THE ROLE OF STABLE LAYERS AND EXTERNAL THERMAL PERTURBATIONS ON PLANETARY DYNAMOS

by

Chi Yan

A dissertation submitted to The Johns Hopkins University in conformity with the requirements for the degree of Doctor of Philosophy

Baltimore, Maryland
May, 2021

Abstract

Planetary magnetic fields are generated in their deep interiors by a self-sustained dynamo process that involves complex motions of electrically conducting fluids in the presence of existing magnetic fields. Numerical simulations have shown that dynamo action is sensitive to variations of the interior structure and boundary conditions such as thickness of the dynamo regions and the presence of stably stratified layers as well as heat flux patterns at the boundary of the dynamo region. Diagnosis of the effect of specific properties and conditions are therefore useful for comparison to the observational data of planetary magnetic fields, providing information on their interior structures. Here I perform three case studies:

(1) Geomagnetic octupole anomaly

Current "Earth-like" numerical dynamo simulations are able to reproduce many characteristics of the observed geomagnetic field. One notable exception is the geomagnetic octupolar component. Here I investigate whether a stably stratified layer at the top of the core, a missing ingredient in standard dynamo simulations, can explain the observed geomagnetic octupole. Through numerical simulations, I find that the existence of a stable layer has a significant influence on the octupole-to-dipole ratio of the magnetic field. In particular, I find that a 60 km stable layer with relatively strong stability or a 130 km layer with relatively weak stability are compatible with the observations, but a 350 km stable layer, as suggested by recent seismological evidence, is not compatible with Earth's octupole field over the past 10,000 years.

(2) Recipe for a Saturn-like dynamo

The Cassini Grand Finale orbits provided detailed observations of Saturn's internal magnetic field. Unique characteristics of the observed field, such as its axisymmetry and power spectrum, provide constraints on dynamo processes deep in Saturn's interior. Here I use numerical dynamo simulations to explore what ingredients are necessary in a dynamo in order to produce the unique "Saturn-like" surface magnetic field. I find that characteristics of Saturn's magnetic field can be sensitive to properties of a stably stratified helium rain-out layer and thermal perturbations at the top of that layer.

(3)Simulations of an ancient martian dynamo

Magnetic field observations from the Mars Global Surveyor, MAVEN, and InSight missions reveal that a dynamo was active in Mars' early history. One unique feature of Mars' crustal field is its hemispheric dichotomy, with the southern hemisphere crustal fields stronger than those in the northern hemisphere. The hemispheric dichotomy has been previously proposed to be due to either crustal reprocessing or a hemispheric dynamo.

Here we use numerical dynamo models to investigate the potential hemispheric nature of Mars' ancient dynamo. Previous studies show that a hemispheric heat flux perturbation at the core-mantle boundary could result in either a stable hemispherical magnetic field or a constantly reversing field, depending on the choices of parameters used in the models. These two scenarios lead to very different implications for the generation of crustal fields. Here we test the dynamo sensitivity to various heat flux perturbations at the core-mantle boundary in a broader parameter regime than previous studies in order to understand whether a hemispheric dynamo is likely for early Mars. We also compare to constraints available on the martian crustal field intensity determined from the InSight mission.

Thesis Committee

Primary Readers

Dr. Sabine Stanley(Primary Advisor)
Professor
Department of Earth and Planetary Sciences
Johns Hopkins Krieger School of Arts & Sciences

Dr.Kevin Lewis
Professor
Department of Earth and Planetary Sciences
Johns Hopkins Krieger School of Arts & Sciences

Alternate Readers

Dr. Sarah Hörst
Professor
Department of Earth and Planetary Sciences
Johns Hopkins Krieger School of Arts & Sciences

Dr. Anand Gnanadesikan
Professor
Department of Earth and Planetary Sciences
Johns Hopkins Krieger School of Arts & Sciences

Acknowledgements

First and foremost, I would like to thank my advisor, Dr. Sabine Stanley for accepting me to do research in the Department of Physics at the University of Toronto and supporting me transferred to the Earth and Planetary Sciences at the Johns Hopkins University. These projects would not have been accomplished if it weren't for your insights, guidance, and support. Furthermore, you've showed me how wonderful and supportive a mentor can be. I am just so fortunate to have you as my advisor, and I hope one day I could pass down and offer the same support that I've been offered during my PhD life.

I would also like to thank my committee members Prof. Kevin Lewis and Prof. Sarah Hörst for enlightening me with their wealth of knowledge and passion of scientific research. I am grateful to have been surrounded with my wonderful group members: Ankit Barik, Viranga Perera, Melissa Sims, Regupathi Angappan, Mayuri Sadhasivan and Miché Aaron. Special thanks to Ankit for enduring me with endless, sometimes naive MagIC questions.

I would also like to thank my friends outside the group: my office mates Hannah Susorney, Xinting Yu, Joseph Serigano, Mariah Baker and Lyle Nelson for sharing laughter in EPS. And thanks to my Chinese friends: Chao He, Yanqing Zhang, Jingyi Huang, Wanshu Nie, Yifan Zhou, Xu Yang and Yinhong Hu, for sharing amazingly delicious food and warmth. And Tangtang who uses her irresistible smiles and cuteness to chase away all my frustration.

Finally, I'd like to thank my parents Xiangdong Yan and Judi Pan and my younger sister Jin Yan, who have been both absolutely supportive and pushing. I would not have completed all the writing if it weren't for my mom when every video chat just started with "When are you graduating". Love you Mom! Last thoughts of thanks goes to my wonderful partner, who I am so blessed to have met during the difficult times, Heyuan Huang, for cooking so many delicious dinners, accompanying during my thesis writing and offering such strong support.

Contents

List of Figures

Chapter 1

Introduction

1.1 Magnetic Fields in our Solar System

Why do we care about studying planetary magnetic fields? First of all, on Earth, the geomagnetic field protects organic life from harmful high energy particles blown from the sun by redirecting these particles to Earth's poles, which forms the aurorae.

Second, planets with large-scale magnetic fields indicate *dynamo action*, which involves complex dynamics of the electrically conducting fluids in their deep interiors. Studying the observed magnetic field provides us with valuable insights of the matter and dynamics of a planet's interior.

Third, the records of the paleomagnetic field can help decoding the history of a planet's magnetic field. For Earth, the remanent magnetic field recorded in the ocean sea floor presents a stripy feature: the magnetic field close to the crest of the mid-ocean ridge obtains the present day dipole polarity, but the field away from the crest shows reversed polarity and this reversing feature continues further away from ridge. We learned from these *magnetic stripes* recorded in the ocean sea floor that the geomagnetic field has gone through several polarity reversals in the past (Vine and Matthews, 1963).

We can also reconstruct the movements and/or collisions of the lithosphere in the past, by studying the features of these remanent magnetic fields. One way to

investigate this is through *apparent polar wander*, a description of the perceived movement of the paleomagnetic pole locations assuming that 1) the continent is fixed in position, and 2) the geomagnetic field can be simplified as an axial dipole. Causes of apparent polar wander could be a combination of true polar wander and continental drift, where the former exerts a minor effect except for during dipole reversal or excursion periods. Take the major plates of China as an example, the paleomagnetic directions restored in the sedimentary rocks at different times in North China Block (NCB) and South China Block (SCB) indicates that the SCB was not adjacent to the NCB in late Permian time and possibly later on collided with the NCB at the easternmost corner and then rotated clockwise relative to the NCB for more than 60° (X. Zhao and Coe, 1987).

1.1.1 Spatial Features of Planetary Magnetic Fields

Planets in our solar system have been investigated by spacecraft missions over the last 60 years, many of which carried magnetometers on board (Stanley, 2014). A majority of the planets and some moons are revealed to have active dynamos, including Mercury (Ness et al., 1975; 1976; Anderson et al., 2008; 2011; 2012), Earth (Langel et al., 1982; Olsen et al., 2000; Langlais et al., 2003; Sabaka et al., 2004), the two gas giants Jupiter (Smith et al., 1974; 1975; Ness et al., 1979; 1979; Moore et al., 2017; Connerney et al., 2018) and Saturn (Acuña & Ness 1980; Ness et al., 1981; Connerney et al., 1982; Cao et al., **cao:etal:2011**; Dougherty et al., 2018), the two ice giants Uranus (Connerney et al., 1987) and Neptune (Ness et al., 1989), and one of Jupiter's natural satellites, Ganymede (Kivelson et al., 1996; Gurnett et al., 1996).

Some other planets, moons or smaller celestial bodies such as asteroids show evidence of past dynamo processes. The planet Mars doesn't possess an active dynamo today, but its global crustal field mapped by Mars Global Surveyor (Acuña et al., 1999), as well as the magnetization found on a martian meteorite ALH84001 (Weiss et

al., 2002), likely results from an ancient martian dynamo in the planet's early history. Similarly, for the Earth's Moon, Lunar Prospector (Halekas et al., 2001; Hood et al., 2001; Purucker & Nicholas, 2010) and other spacecraft missions (e.g. the Kaguya satellite, Tsunakawa et al., 2010) found localized crustal magnetic fields on the surface of the Moon, suggesting the likely presence of an ancient lunar dynamo, corroborated by the collected Apollo samples (Cournède et al., 2012; Garrick-Bethell et al., 2009; 2017). For smaller celestial bodies such as planetesimals or asteroids, it is possible to sustain a dynamo for a short period of time (around a few million years) given sufficient heat from short lived radioactive isotopes such as Al^{26} (Weiss et al., 2010). For example, the remanent magnetization extracted from the eucrite meteorite Allan Hills A81001 supports the presence of an earlier dynamo, at least 3.7 billion years ago, in the asteroid 4 Vesta (Fu et al., 2012).

The only planet in our solar system that has shown no evidence of present or past dynamo action is Venus (Bridge et al., 1967; Ness et al., 1974), despite its similarities to Earth. The high surface temperature of Venus would have removed any remanent magnetization of most ferromagnetic minerals in the Venusian crust (e.g. Luhmann & Russell, 1997, Breuer et al., 2010). However, recent studies argue that the surface temperature of Venus is about $100K$ to $200K$ below the Curie temperature of minerals such as magnetite and hematite (O'Rourke et al., 2018; 2019), so it may be worth searching for crustal magnetic fields with future missions.

Figure 1-1 presents the surface radial magnetic fields of different planets that have active dynamo processes in their interiors. Ganymede, Jupiter's largest moon, is the only natural satellite with an intrinsic magnetic field (approximately antiparallel to Jupiter's magnetic field) at the present day (Kivelson et al., 1996; Gurnett et al., 1996). However, current data can only constrain the dipole moment of Ganymede's magnetic field, therefore it is not shown in Figure 1-1.

As can be seen from Figure 1-1, the most prominent feature of a planet's global-

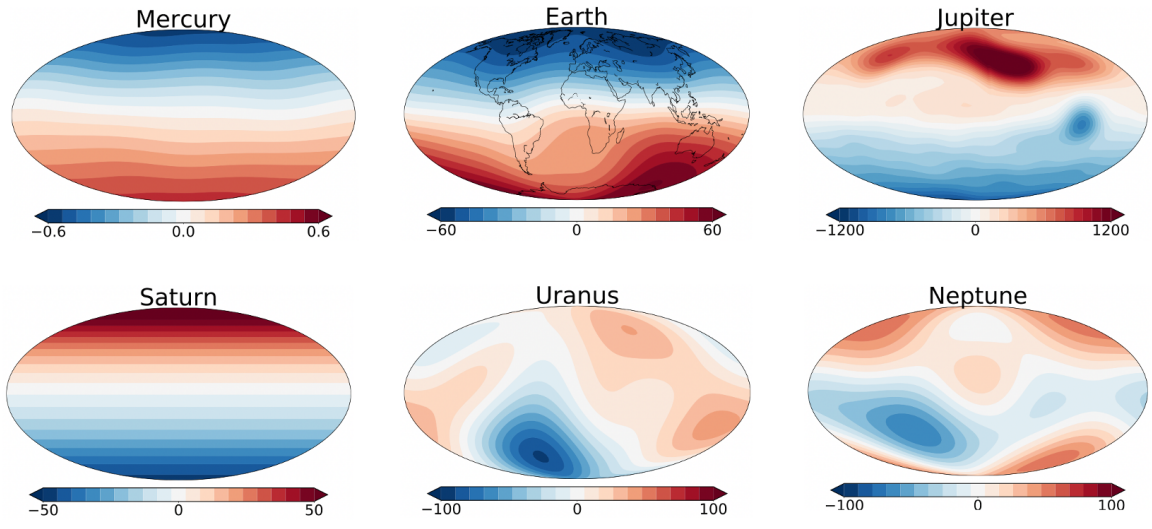

Figure 1-1. Surface radial magnetic fields of different planets, units are in μT. Red/Blue represent magnetic field lines going out/into the planets. Data for computing the magnetic field is listed below. Mercury: Anderson et al. (2011); Thébault et al. (2018). Earth: Thébault et al. (2015). Jupiter: Connerney et al. (2018). Saturn: Dougherty et al. (2018); Cao et al. (2020). Uranus & Neptune: Connerney et al. (1987; 1991); Holme & Bloxham (1996)

scale magnetic field is the *dipolarity*, i.e. whether a planet's surface magnetic field is dominated by the axial dipole component, as is Mercury, Earth, Jupiter, Saturn, and Ganymede. On the contrary, the magnetic fields of Uranus and Neptune are *multipolar*: the axial dipole component takes no dominance of the total field but instead shares a similar magnitude to other small-scale and non-axisymmetric components.

The four dipolar dominated fields can be further differentiated by the amount of the non-axisymmetric magnetic field component seen at the surfaces. Earth and Jupiter's dipolar fields are both tilted around 10° away from their planetary rotational axes, although their non-dipolar fields differ significantly: for Jupiter, the non-dipolar fields at a potential dynamo surface ($0.9R_J$, Tsang & Jones, 2020) are localized in the northern hemisphere, whereas for Earth, the non-dipolar fields at the core-mantle boundary ($0.54R_E$) are more evenly distributed in both hemispheres (Figure 1-2).

In contrast, for Mercury and Saturn, their magnetic fields observed at the surface are both very axisymmetric, i.e. the magnetic axis is almost aligned with the planetary

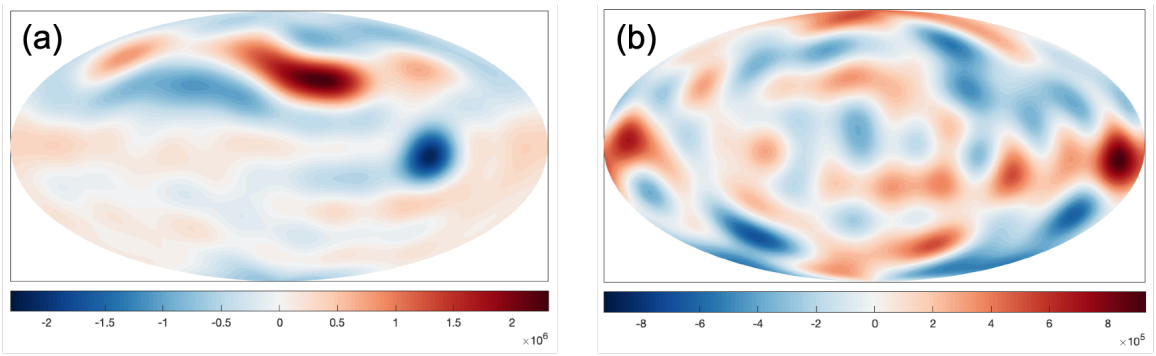

Figure 1-2. The non-dipolar radial magnetic field at (a) $0.9R_J$ of Jupiter and (b) $0.54R_E$ of Earth. Gauss coefficients are both truncated to $l = 10$. Units are in nT. Red/Blue represent magnetic field lines going out/into the planets. Figure adapted from Moore et al., (2018).

rotational axis. The dipole tilt of Mercury is less than 0.8° with a northward offset about 500 km, due to a large contribution of the magnetic quadrupole (Anderson et al., **Anderson:etal:2012**). The dipole tilt of Saturn's magnetic field is constrained to be less than 0.007° (Cao et al., 2020), possibly the most axisymmetric planetary magnetic field in our solar system.

1.1.2 Gauss Coefficients

These spatial features can be quantitatively summarized into the *Gauss coefficients*. Outside the dynamo region where no electrical currents should exist in the insulator, the magnetic field $\mathbf{B}$ can be represented as the gradient of a scalar potential V. The Gauss coefficients are then defined by the expression:

$$V(r,\theta,\phi) = a\sum_{l=1}^{\infty}\sum_{m=0}^{l}[g_l^m cosm\phi + h_l^m sinm\phi]\left(\frac{a}{r}\right)^{l+1} P_l^m(cos\theta) \tag{1.1}$$

where r is radius, θ the co-latitude, ϕ the longitude, and a is the surface radius of a planet. The g_l^m and h_l^m coefficients are named Gauss coefficients where l and m are the spherical harmonic degree and order, respectively, and the $P_l^m(cos\theta)$ are the associated Legendre polynomials.

Summing the mean square magnetic field contributed at each spherical harmonic

degree l, we then have the magnetic power spectrum at a particular radius r:

$$R_l = (l+1)\left(\frac{a}{r}\right)^{2l+4} \sum_{m=0}^{l} \left[(g_l^m)^2 + (h_l^m)^2\right] \tag{1.2}$$

which can be simplified to the Lowes spectrum (Lowes, 1974) equation when r is taken equal to the planetary radius a. The slope in Earth's Lowes spectrum (except the dipole field) reflects the dynamo surface ($0.54R_E$, i.e. Earth's core mantle boundary), where the magnetic power at all degrees (except the dipole field) contributes relatively equally. A noticeable quality of Eq. 1.2 is that as the radius r gets further away to the dynamo-generated region and closer to the planetary surface (a), magnetic power in the higher spherical harmonic degrees gets more diminished, due to the exponential decay in degree l, at a rate of $(a/r)^{2l+4}$. Therefore, without preferential excitation in specific spherical harmonic degrees, the surface magnetic field of a planet with its dynamo region closer to the planetary surface, may contain more power in the non-dipolar, smaller scale features.

For example, the top of the dynamo region of Jupiter ($R_{J_{core}} \sim 0.9R_J$, Tsang & Jones 2020) is very close to its surface, therefore its magnetic field observed at the surface contains more smaller scale features, such as the strong blue spot near the equator. In contrast, Jupiter's magnetic field looks a lot more dipolar if we extrapolate the surface to a hypothetical radius at $R'_J = 1.67R_J$, the same dynamo to surface ratio as Earth (i.e. $R_{J_{core}}/R'_J = 0.54$), shown in Figure 1-3.

1.1.3 Temporal Features of Planetary Magnetic Fields

Planetary magnetic fields are dynamo generated, so they vary in time. To acquire temporal features of the planetary magnetic fields, we need either satellites that can orbit the planet and record the field for some time, or rock samples that preserve the paleomagnetic field with remanent magnetization, where the latter method requires crust on the planetary surface, and is therefore not viable for giant planets.

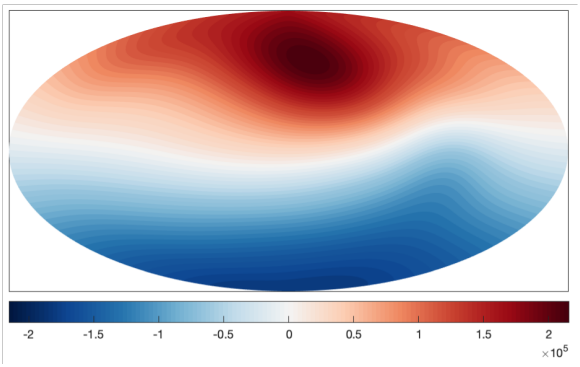

Figure 1-3. The radial magnetic field of Jupiter seen at $1.67R_J$. Units are in nT. Red/Blue represent magnetic field lines going out/into the planets.

Earth: The geomagnetic field is the best known planetary field in temporal resolution, and the field varies on a wide range of time scales. The most prominent temporal feature of the geomagnetic field at the longest wavelength is the polarity reversals. The first definite evidence of the geomagnetic polarity reversal was established by two groups (Cox et al. 1963; McDougal & Tarling 1963) which combined K-Ar dating with the paleomagnetism in lava flows and showed the synchronicity of the geomagnetic polarity reversals over the globe. The study of paleomagnetism further progressed as Vine and Drummond (1963) proposed the magnetic tape recording theory at the mid-ocean ridges. The geomagnetic field reverses aperiodically, with an average frequency around 0.5 Ma. If the direction of the dipole moment changes drastically but doesn't result in a reversal, then it is called a geomagnetic excursion, which happens much more often than polarity reversals. The geomagnetic field can also vary on decadal time scales, i.e. the *secular variation*, such as the westward drift (Vestine et al., 1968; Dumberry et al., 2007) or the geomagnetic jerks (Mandea et al., 2010; Aubert et al., 2019).

Earth's Moon: The lunar magnetic field is the only other field that we have a time series of, though not continuous, paleomagnetic record (Figure 1-4). From the lunar rocks collected during the Apollo missions, the ancient lunar dynamo is found to have generated a strong magnetic field (comparable to the present-day Earth) from

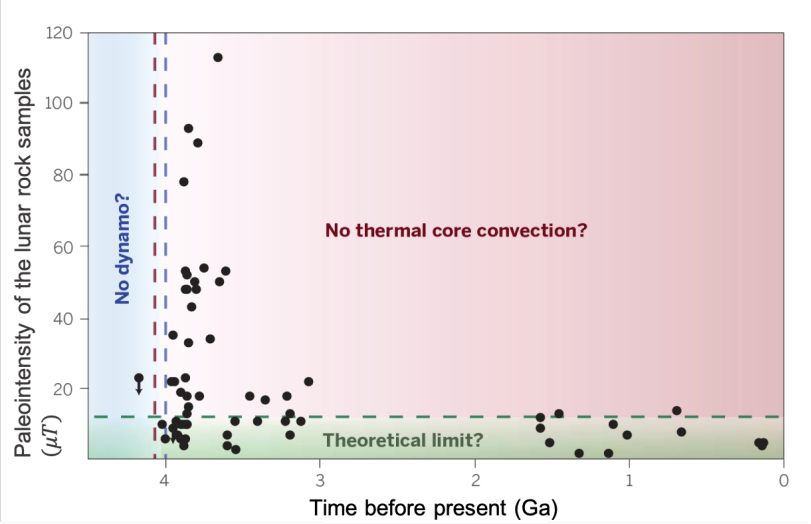

Figure 1-4. The paleointensity measurements of the lunar rocks collected from the Apollo mission. Figure adapted from Weiss & Tikoo (2014).

4.25 − 3.56 Gya, followed by a long lived weaker field after around 3.3 Gya. The persistent ancient dynamo of Earth's Moon is very interesting since a conventional dynamo powered by thermal convection could not last long given the Moon's size. Alternative theories such as mechanical stirring (Dwyer et al., 2011), impact-driving (Le Bars et al., 2011), thermal blanket (Stegman et al., 2003) or water-rich mantle (Evans et al., 2014) have been proposed to support the lunar dynamo budget.

Jupiter & Saturn: Since the first visits by Pioneer 10 and 11, Jupiter's and Saturn's magnetic fields have been observed by spacecraft missions for over 40 years, allowing possible detection of the secular variation.

For Jupiter, Ridley & Holme (2016) investigated magnetic measurements from 1973 to 2003 and found a slight increase ($\sim 0.012\%\ yr^{-1}$) of Jupiter's magnetic dipole moment. Studies by Moore et al. (2019) found variations in Jupiter's magnetic field, possibly caused by its interactions with the zonal winds, and predicted the disruption of the Great Blue Spot in the next few decades.

On the contrary, Saturn's magnetic field has shown no detectable secular variation. Studies led by Cao et al. (**Cao:2011aa**) show that the secular variation of Saturn's

magnetic field is at least an order of magnitude smaller than that of the geomagnetic field, whereas from scaling laws a comparable rate was expected for Saturn. The low rate of secular variation of Saturn's magnetic field provides independent evidence of a stably stratified layer in between Saturn's dynamo region and its surface, as the slow secular variation is a natural consequence of a stable layer (Stanley & Bloxham, 2016).

1.2 Planetary dynamo processes

The nature of the geomagnetic field as well as other planetary magnetic fields resides in the dynamo process, which from an energetic perspective, transfers mechanical energy to magnetic energy through the work done by Lorentz forces. In Earth, the convection in its fluid outer core is driven by both thermal and compositional buoyancy sources that are produced as Earth slowly cools and iron-rich alloys solidify onto the inner core giving off latent heat and releasing lighter elements. These buoyancy forces cause fluids to rise and the Coriolis force, due to the Earth's rotation, causes fluids to differentially rotate, resulting in helical flows that are beneficial for magnetic field generation. These complex fluid motions furthermore twist and shear the existing magnetic field through alpha and beta effects, and generate new magnetic fields to replace those that dissipated away.

Dynamo action is sensitive to a planet's interior structure and thermal evolution. First of all, it is difficult to categorize whether a planet obtains an active dynamo just from bulk properties, which unfortunately are often the only parameters we know for exoplanets. A classic example in our solar system is the contrast of Venus and Earth. Since Venus shares similar size, chemical compositions, and a similar layered structure (i.e. crust-mantle-core) with Earth, it was surprising to learn about the lack of a Venusian dynamo at the present day. We now think that Venus doesn't possess an active dynamo possibly because its mantle layer is not cooling sufficiently enough to drive vigorous convection as Earth does (Nimmo, 2002).

Second, dynamo action and its resulting magnetic morphology may be affected by planetary interior structures such as stably stratified layers, inner core sizes, etc. The density structure inside a stably stratified layer inhibits convection and so differential rotation dominates the dynamics inside such a layer. This could further lead to interesting interactions with planetary magnetic fields such as the electromagnetic skin effect which will is more thoroughly discussed in Section 2.5.

Finally, planetary dynamos are closely connected to their thermal histories, as thermal energy serves as one major buoyancy source of core convection. For example, some small bodies such as planetesimals and asteroids in the solar system may once have possessed dynamos in their early histories (e.g. asteroid 4 Vesta, Fu et al., 2012), given sufficient heat budget. Nevertheless, it is difficult to sustain these dynamos of small bodies because the amount of radiogenic heating inside these bodies can only support core convection for a short period of time. On the other hand, it is also worth noting that other buoyancy sources (e.g. compositional buoyancy) or driving mechanisms (e.g. mechanical stirring, Dwyer et al., 2011) may also power a planetary dynamo.

1.3 Toroidal and Poloidal Decomposition

In the dynamo community, we often use the toroidal and poloidal field to describe the magnetic field and the incompressible fluid flow field. In spherical coordinates, we can describe the magnetic field as $\mathbf{B} = (B_r, B_\theta, B_\phi)$. Gauss' Law for magnetism requires that:

$$\nabla \cdot \mathbf{B} = 0 \tag{1.3}$$

This means the magnetic field $\mathbf{B}$ can be represented as

$$\mathbf{B} = \nabla \times \mathbf{A} \tag{1.4}$$

where $\mathbf{A}$ is known as the magnetic vector potential, which can be represented by two orthogonal components,

$$\mathbf{A} = T\mathbf{r} + \nabla \times (P\mathbf{r}) \tag{1.5}$$

The magnetic field in this fashion can be written as

$$\begin{aligned} \mathbf{B} &= \mathbf{B_T} + \mathbf{B_P} \\ &= \underbrace{\nabla \times (T\mathbf{r})}_{toroidal} + \underbrace{\nabla \times [\nabla \times (P\mathbf{r})]}_{poloidal} \end{aligned} \tag{1.6}$$

where $\mathbf{B_T}$ is the toroidal field which only has θ and ϕ components but no r component. $\mathbf{B_P}$ is the poloidal magnetic field which may have components in all directions.

The choice of toroidal-poloidal (T-P) decomposition is beneficial. First, toroidal and poloidal components form an orthogonal basis, whereby any field can be fully described by these two components. Second, T-P decomposition has an elegant physics interpretation, i.e. poloidal electrical currents can generate toroidal magnetic fields and vice versa, toroidal electrical currents can generate poloidal magnetic fields.

$$\nabla \times \mathbf{B_T} = \nabla \times \nabla \times T\mathbf{r} \tag{1.7}$$

which obtains the form of a poloidal field on the right hand side. Furthermore,

$$\begin{aligned} \nabla \times \mathbf{B_P} &= \nabla \times [\nabla \times \nabla \times P\mathbf{r}] \\ &= \nabla \times \left[\cancelto{0}{\nabla \left(\frac{\partial}{\partial r}(rP) \right)} - \nabla^2 P\mathbf{r} \right] \end{aligned} \tag{1.8}$$

where the first term on the right hand side becomes 0 because $\nabla \times \nabla f = 0$, which then obtains the form of a toroidal field. Figure 1-5 shows the axisymmetric toroidal (left) and poloidal (right) magnetic fields. Contours of the toroidal fields are plotted on the left hand side, where red solid (purple dashed) lines represent toroidal fields coming out (going into) the page. Magnetic poloidal field lines are shown on the right hand side.

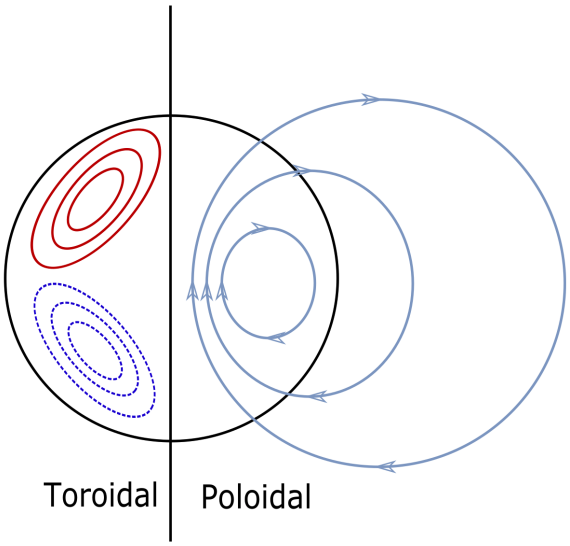

Figure 1-5. Illustration of the toroidal and poloidal magnetic field.

1.4 Governing Equations of MHD

In this section we retrieve the fundamental equations for magnetohydrodynamic (MHD) theory, which govern the evolution of the velocity, magnetic and energy fields in time and space. The information presented in this section can be found in standard dynamo theory and magnetism texts such as Mathematical Aspects of Natural Dynamos (2007) or Dynamos (2011). We start with the magnetic field. Table 1-I lists the set of Maxwell's equations, the Lorentz force equation and Ohm's law, where $\mathbf{E}$, $\mathbf{B}$, $\mathbf{J}$ are the electric, magnetic, and electric current density fields, $\mathbf{u}$ is the velocity field, ρ_e is the charge density, ϵ_0, μ_0 are the permittivity and permeability of free space and σ is the Stefan-Boltzman constant. Because we are essentially dealing with electrical fluid conductors with characteristic speeds (u) that are far less than the speed of light (c), the displacement current term $\frac{1}{c^2}\frac{\partial \mathbf{E}}{\partial t} \ll \nabla \times \mathbf{B}$ in Ampere's Law as well as the term $\rho_e \mathbf{E}$ in the Lorentz force equation can be neglected. This form of the equations is known as the ***MHD approximation***.

To derive an equation showing the evolution of the magnetic field that only involves

Category	Name	Differential Form
Maxwell Equations	Gauss's Law	$\nabla \cdot \mathbf{E} = \frac{\rho_e}{\epsilon_0}$
	Gauss's Law for Magnetism	$\nabla \cdot \mathbf{B} = 0$
	Faraday's Law	$\nabla \times \mathbf{E} = -\frac{\partial \mathbf{B}}{\partial t}$
	Ampere's Law	$\nabla \times \mathbf{B} = \mu_0 \mathbf{J} + \cancel{\frac{1}{c^2}\frac{\partial \mathbf{E}}{\partial t}}^{0}$
	Lorentz Force	$\mathbf{F_L} = \cancel{\rho_e \mathbf{E}}^{0} + \mathbf{J} \times \mathbf{B}$
	Ohm's Law	$\mathbf{J} = \sigma(\mathbf{E} + \mathbf{u} \times \mathbf{B})$

Table 1-I. Equations of Electromagnetism for MIE with the MHD approximation indicated by which terms are neglected.

$\mathbf{B}$ as a variable, we begin by taking the curl of Ohm's Law:

$$\nabla \times \mathbf{J} = \sigma \nabla \times \mathbf{E} + \sigma \nabla \times (\mathbf{u} \times \mathbf{B}) \tag{1.9}$$

Using Ampere's Law, the left hand side of Eq. 1.9 becomes $\frac{1}{\mu_0}(\nabla \times \nabla \times \mathbf{B})$. Using differential operator identities (i.e. $\nabla \times (\nabla \times \mathbf{A}) = \nabla(\nabla \cdot \mathbf{A}) - \nabla^2 \mathbf{A}$), Eq. 1.9 can be written as:

$$\begin{aligned} \nabla \cancel{(\nabla \cdot \mathbf{B})}^{0} - \nabla^2 \mathbf{B} &= \mu_0 \sigma \left[\nabla \times \mathbf{E} + \nabla \times (\mathbf{u} \times \mathbf{B})\right] \\ &= \mu_0 \sigma \left[\left(-\frac{\partial \mathbf{B}}{\partial t}\right) + \nabla \times (\mathbf{u} \times \mathbf{B})\right] \end{aligned} \tag{1.10}$$

where $\nabla \cdot \mathbf{B}$ is 0 because there is no magnetic monopoles, and we used Faraday's law to replace $\nabla \times \mathbf{E}$ with $-\frac{\partial \mathbf{B}}{\partial t}$. Rearranging both sides to get the time derivative to the left hand side, we now have the ***Magnetic Induction Equation (MIE)***:

$$\frac{\partial \mathbf{B}}{\partial t} = \nabla \times (\mathbf{u} \times \mathbf{B}) + \lambda \nabla^2 \mathbf{B} \tag{1.11}$$

where λ is the magnetic diffusivity, defined as $\lambda = 1/\mu_0 \sigma$, with unit of m^2/s.

The MIE says how magnetic fields evolve with time depends on two things: 1) the generation term $\nabla \times (\mathbf{u} \times \mathbf{B})$, and 2) the dissipation term $\lambda \nabla^2 \mathbf{B}$. The ratio of these two terms is known as the magnetic Reynolds number (Re_M), which evaluates the relative effect of the magnetic induction to the diffusion:

$$\begin{aligned} Re_M &= \frac{|\nabla \times (\mathbf{u} \times \mathbf{B})|}{|\lambda \nabla^2 \mathbf{B}|} \\ &\sim \frac{UL}{\lambda} \end{aligned} \tag{1.12}$$

so Re_M is proportional to the length L, velocity U and electrical conductivity $\sim 1/\lambda$. When estimating the Re_M, the radius of the dynamo source region is often taken as the length scale, e.g. 3486 km for the geodynamo; the electrical conductivity of different materials such as iron, metallic hydrogen and ionic water, can be estimated using high pressure experiments; however, the characteristic velocity in planets is not very well constrained. Assuming an Earth-like velocity $U = 5 \times 10^{-4} m/s$, the magnetic Reynolds number of the geodynamo is $Re_M = O(10^3)$.

Further expanding the induction term:

$$\nabla \times (\mathbf{u} \times \mathbf{B}) = \mathbf{u}(\cancelto{0}{\nabla \cdot \mathbf{B}}) - \mathbf{B}(\nabla \cdot \mathbf{u}) + (\mathbf{B} \cdot \nabla)\mathbf{u} - (\mathbf{u} \cdot \nabla)\mathbf{B} \tag{1.13}$$

then we have MIE as:

$$\frac{\partial \mathbf{B}}{\partial t} + \underbrace{(\mathbf{u} \cdot \nabla)\mathbf{B}}_{a} = \underbrace{(\mathbf{B} \cdot \nabla)\mathbf{u}}_{b} - \underbrace{\mathbf{B}(\nabla \cdot \mathbf{u})}_{c} + \underbrace{\lambda \nabla^2 \mathbf{B}}_{d} \tag{1.14}$$

so the magnetic field can be changed by four terms: a) advection of the fluid flow, which combined with $\partial \mathbf{B}/\partial t$, is noted as the material (or Lagrangian) derivative $D\mathbf{B}/Dt$; b) stretching of the magnetic field lines due to velocity gradients; c) compression/dilation of the fluid flow; and d) magnetic diffusion.

1.4.1 Bullard-Gellman Formalism

The Bullard-Gellman formalism (Bullard & Gellman, 1954) offers a simplified system to investigate the interactions between fluids and magnetic fields. It is helpful in determining whether specific fluid modes can be excited due to certain layout of the interior geometry or external thermal perturbations, and could further influence the excitation or suppression of specific magnetic modes. Details on the applications of the Bullard-Gellman formalism for Chapter 2 and Chapter 3 can be found in the Appendix I. *The vector fields are represented with arrows for concision.*

The problem set-up:

Here we consider work in the geometry of a conducting fluid sphere of non-dimensional

radius $r = 1$, surrounded by an infinite insulator. The fluid is assumed to be incompressible, i.e $\nabla \cdot \mathbf{u} = 0$. Therefore in the dynamo region ($r < 1$) the nondimensional MIE becomes:

$$\frac{\partial \mathbf{B}}{\partial t} = Re_M \nabla \times (\mathbf{u} \times \mathbf{B}) + \nabla^2 \mathbf{B} \tag{1.15}$$

In the insulating outer layer ($r \geq 1$), we have

$$\nabla \times \mathbf{B} = 0 \tag{1.16}$$

Finally because magnetic monopoles do not exist (Gauss's law of magnetism), $\nabla \cdot \mathbf{B} = 0$. Here we seek solutions of an exponential form

$$\mathbf{B} = \mathbf{B}(\mathbf{r}) e^{pt} \tag{1.17}$$

so that the time derivative of $\mathbf{B}$ is $p\mathbf{B}$, the Magnetic Induction Equation (Eq. 1.15) then becomes

$$(p - \nabla^2)\mathbf{B} = Re_M \nabla \times (\mathbf{u} \times \mathbf{B}) \tag{1.18}$$

We perform a Toroidal-Poloidal decomposition of the velocity ($\mathbf{u}$) and magnetic ($\mathbf{B}$) fields:

$$\begin{aligned} \mathbf{u} &= \mathbf{u}_T + \mathbf{u}_P = \sum_{l,m} (\mathbf{t}_l^m + \mathbf{p}_l^m) \\ \mathbf{B} &= \mathbf{B}_T + \mathbf{B}_P = \sum_{l,m} (\mathbf{T}_l^m + \mathbf{P}_l^m) \end{aligned} \tag{1.19}$$

in which

$$\begin{cases} \mathbf{t}_l^m = \nabla \times [t_l^m(r) Y_l^m(\theta, \phi) \hat{r}] \\ \mathbf{p}_l^m = \nabla \times \nabla \times [p_l^m(r) Y_l^m(\theta, \phi) \hat{r}] \\ \mathbf{T}_l^m = \nabla \times [T_l^m(r) Y_l^m(\theta, \phi) \hat{r}] \\ \mathbf{P}_l^m = \nabla \times \nabla \times [P_l^m(r) Y_l^m(\theta, \phi) \hat{r}] \end{cases} \tag{1.20}$$

where $\hat{r}$ is the unit vector in the radial direction. Since there are no electric currents outside the dynamo region ($T = 0$, and $\nabla^2 P = 0$) so the boundary conditions of the magnetic field at $r = 1$ can be written as:

$$
\begin{aligned}
T_l^m(r) &= 0 \\
\frac{dP_l^m(r)}{dr} + l(l+1)P_l^m(r) &= 0
\end{aligned}
\tag{1.21}
$$

We can further substitute the Poloidal-Toroidal decomposition of the $\mathbf{u}$ and $\mathbf{B}$ into Eq. 1.18 and get:

$$
\left(p - \nabla^2\right)\left[\sum_1(\mathbf{T}_{l1}^{m1} + \mathbf{P}_{l1}^{m1})\right] = Re_M \nabla \times \left\{\left[\sum_2(\mathbf{t}_{l2}^{m2} + \mathbf{p}_{l2}^{m2})\right] \times \left[\sum_3(\mathbf{T}_{l3}^{m3} + \mathbf{P}_{l3}^{m3})\right]\right\} \tag{1.22}
$$

where the numeric subscripts under the summation symbol denote the summation over the l and m of that index. We can interpret Eq. 1.22 as the sum of all modes of the ($\sum_1$) magnetic field is a product of all velocity modes ($\sum_2$) acting on all the magnetic modes ($\sum_3$). For a specific toroidal or poloidal mode, we can calculate the inner product of the Eq. 1.22 with a specific toroidal mode $\nabla \times [Y_{l1}^{m1}(\theta,\phi)\hat{r}]^*$, or a specific poloidal mode $\nabla \times \nabla \times [Y_{l1}^{m1}(\theta,\phi)\hat{r}]^*$ where $*$ denotes the complex conjugate, and integrate over the $r = 1$ surface:

$$
\begin{aligned}
&\oint_S \left[\nabla \times \left(Y_{l1}^{m1}(\theta,\phi)\hat{r}\right)\right]^* \cdot \left(p - \nabla^2\right)\left[\sum_1(\mathbf{T}_{l1}^{m1} + \mathbf{P}_{l1}^{m1})\right] = \\
Re_M &\oint_S \left[\nabla \times \left(Y_{l1}^{m1}(\theta,\phi)\hat{r}\right)\right]^* \cdot \nabla \times \left\{\left[\sum_2(\mathbf{t}_{l2}^{m2} + \mathbf{p}_{l2}^{m2})\right] \times \left[\sum_3(\mathbf{T}_{l3}^{m3} + \mathbf{P}_{l3}^{m3})\right]\right\}
\end{aligned}
\tag{1.23}
$$

for toroidal fields, or for poloidal fields:

$$
\begin{aligned}
&\oint_S \left[\nabla \times \nabla \times \left(Y_{l1}^{m1}(\theta,\phi)\hat{r}\right)\right]^* \cdot \left(p - \nabla^2\right)\left[\sum_1(\mathbf{T}_{l1}^{m1} + \mathbf{P}_{l1}^{m1})\right] = \\
Re_M &\oint_S \left[\nabla \times \nabla \times \left(Y_{l1}^{m1}(\theta,\phi)\hat{r}\right)\right]^* \cdot \nabla \times \left\{\left[\sum_2(\mathbf{t}_{l2}^{m2} + \mathbf{p}_{l2}^{m2})\right] \times \left[\sum_3(\mathbf{T}_{l3}^{m3} + \mathbf{P}_{l3}^{m3})\right]\right\}
\end{aligned}
\tag{1.24}
$$

Now we can use orthogonality of the spherical harmonics,

$$
\begin{aligned}
\oint_S \mathbf{T}_l^{m*} \cdot \mathbf{P}_l^m dS &= 0 \\
\oint_S \mathbf{T}_l^{m*} \cdot \mathbf{T}_p^q dS &= T_l^m(r) T_p^q(r) \delta_{lp}\delta_{mq} \\
\oint_S \mathbf{P}_l^{m*} \cdot \mathbf{P}_p^q dS &= P_l^m(r) P_p^q(r) \delta_{lp}\delta_{mq}
\end{aligned}
\tag{1.25}
$$

and also ∇^2 is a derivative only related to r, so it can be pulled in front of the surface integral.

$$\nabla^2 = \frac{1}{r^2}\frac{\partial}{\partial r}\left(r^2\frac{\partial}{\partial r}\right) - \frac{l(l+1)}{r^2} \tag{1.26}$$

Substitute the (t_l^m, p_l^m) and (T_l^m, P_l^m) using the Eq. 1.20, the Eq. 1.23 then becomes:

$$\begin{aligned}(p-\nabla^2)\mathbf{T}_{l1}^{m1}(r) = Re_M \oint_S \left[\nabla\times\left(Y_{l1}^{m1}(\theta,\phi)\hat{r}\right)\right]^* \\ \cdot\nabla\times\left[\sum_2\left(\nabla\times\left[t_{l2}^{m2}(r)Y_{l2}^{m2}(\theta,\phi)\hat{r}\right]+\nabla\times\nabla\times\left[p_{l2}^{m2}(r)Y_{l2}^{m2}(\theta,\phi)\hat{r}\right]\right)\right] \\ \times\left[\sum_3(\nabla\times\left[T_{l3}^{m3}(r)Y_{l3}^{m3}(\theta,\phi)\hat{r}\right]+\nabla\times\nabla\times\left[P_{l3}^{m3}(r)Y_l^m(\theta,\phi)\hat{r}\right])\right]dS\end{aligned} \tag{1.27}$$

Because (t_l^m, p_l^m) and (T_l^m, P_l^m) only depend on r and Eq. 1.27 is a surface integral over a fixed r, we can pull out these coefficients and Eq. 1.27 becomes:

$$\begin{aligned}&(p-\nabla^2)\mathbf{T}_{l1}^{m1}(r) = Re_M\sum_2\sum_3 \\ &t_{l2}^{m2}(r)T_{l3}^{m3}(r)\oint_S\left[\nabla\times\left(Y_{l1}^{m1}(\theta,\phi)\hat{r}\right)\right]^*\cdot\left[\nabla\times\left(\nabla\times Y_{l2}^{m2}(\theta,\phi)\hat{r}\right)\times\left(\nabla\times Y_{l3}^{m3}(\theta,\phi)\hat{r}\right)\right]dS \\ &+t_{l2}^{m2}(r)P_{l3}^{m3}(r)\oint_S\left[\nabla\times\left(Y_{l1}^{m1}(\theta,\phi)\hat{r}\right)\right]^*\cdot\left[\nabla\times\left(\nabla\times Y_{l2}^{m2}(\theta,\phi)\hat{r}\right)\times\left(\nabla\times\nabla\times Y_{l3}^{m3}(\theta,\phi)\hat{r}\right)\right]dS \\ &+p_{l2}^{m2}(r)T_{l3}^{m3}(r)\oint_S\left[\nabla\times\left(Y_{l1}^{m1}(\theta,\phi)\hat{r}\right)\right]^*\cdot\left[\nabla\times\left(\nabla\times\nabla\times Y_{l2}^{m2}(\theta,\phi)\hat{r}\right)\times\left(\nabla\times Y_{l3}^{m3}(\theta,\phi)\hat{r}\right)\right]dS+ \\ &p_{l2}^{m2}(r)P_{l3}^{m3}(r)\oint_S\left[\nabla\times\left(Y_{l1}^{m1}(\theta,\phi)\hat{r}\right)\right]^*\cdot\left[\nabla\times\left(\nabla\times\nabla\times Y_{l2}^{m2}(\theta,\phi)\hat{r}\right)\times\left(\nabla\times\nabla\times Y_{l3}^{m3}(\theta,\phi)\hat{r}\right)\right]dS\end{aligned} \tag{1.28}$$

Similarly, one can expand Eq. 1.24. The integrals in Eq. 1.28 can be categorized into two families, an *Adams-Gaunt integral*:

$$AG = \oint_S Y_{l1}^{m1*}Y_{l2}^{m2}Y_{l3}^{m3}dS \tag{1.29}$$

or an *Elsasser integral*:

$$El = \oint_S Y_{l1}^{m1*}\left(\frac{\partial Y_{l2}^{m2}}{\partial\theta}\frac{\partial Y_{l3}^{m3}}{\partial\phi} - \frac{\partial Y_{l2}^{m2}}{\partial\phi}\frac{\partial Y_{l3}^{m3}}{\partial\theta}\right)dS \tag{1.30}$$

A practical way to distinguish the integrals is to count the number of ∇s: an odd number of ∇s is an *Adams-Gaunt integral* and an even number of ∇s is an *Elsasser integral*.

Notation:

Next we simplify Eq. 1.28 by notating and categorizing these two types of integrals. First, we use (α, β, γ) to represent spherical harmonic degrees of the different fields, and $(m_\alpha, m_\beta, m_\gamma)$ to represent the spherical harmonic orders. We note the magnetic field that is being produced γ (i.e. $(l1, m1) \rightarrow \gamma$), the velocity field that acts on the existing magnetic field α (i.e. $(l2, m2) \rightarrow \alpha$), and the existing magnetic field that has velocity fields acting on β (i.e. $(l3, m3) \rightarrow \beta$). Then we note T as a toroidal field (i.e. $\nabla \times Y_l^m \hat{r}$) and P as a poloidal field (i.e. $\nabla \times \nabla \times Y_l^m \hat{r}$). Now Eq. 1.28 can be shortened as:

$$(p - \nabla^2) T_\gamma(r) = Re_M \sum_\alpha \sum_\beta (T_\alpha T_\beta T_\gamma + T_\alpha P_\beta T_\gamma + P_\alpha T_\beta T_\gamma + P_\alpha P_\beta T_\gamma) \tag{1.31}$$

and Eq. 1.24 can be shortened as:

$$(p - \nabla^2) P_\gamma(r) = Re_M \sum_\alpha \sum_\beta (T_\alpha T_\beta P_\gamma + T_\alpha P_\beta P_\gamma + P_\alpha T_\beta P_\gamma + P_\alpha P_\beta P_\gamma) \tag{1.32}$$

From anti-dynamo theorems, we know poloidal magnetic fields cannot be created by having toroidal flows acting on toroidal magnetic fields, therefore the term $T_\alpha T_\beta P_\gamma$ is always zero. The other terms then belong to the *Adams-Gaunt Integrals* which have odd number of Ps and even number of Ts:

$$\begin{gathered} T_\alpha P_\beta T_\gamma \\ P_\alpha T_\beta T_\gamma \\ P_\alpha P_\beta P_\gamma \end{gathered} \tag{1.33}$$

or the *Elsasser Integrals* which have even number of Ps and odd number of Ts:

$$\begin{gathered} T_\alpha T_\beta T_\gamma \\ P_\alpha P_\beta T_\gamma \\ P_\alpha T_\beta P_\gamma \\ T_\alpha P_\beta P_\gamma \end{gathered} \tag{1.34}$$

The Selection Rules

For a self-sustaining dynamo, the right hand side of Eq. 1.31 and Eq. 1.32 should be

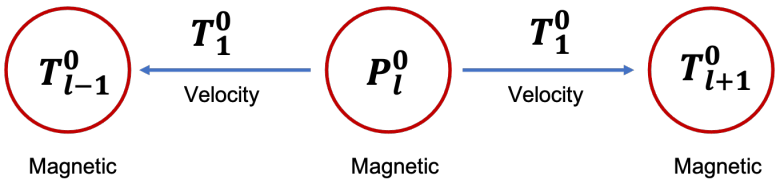

Figure 1-6. Interaction diagram of the Bullard-Gellman formalism. Red circles represent the magnetic field, arrows represent the velocity field (here T_1^0 specifically).

non-zero. Both the *Adams-Gaunt* and *Elsasser* integrals turn out to be zeros, except for a few cases, as defined by their selection rules. The *Adams-Gaunt* integral is zero unless:

1. $\alpha + \beta + \gamma$ is even;
2. α, β, γ can form the sides of a triangle;
3. one or more of the $m_\alpha \pm m_\beta \pm m_\gamma$ vanishes;
4. one or three of the harmonics has the $cos(m\phi)$ term ($m = 0$ counts as $cos(m\phi)$).

For the *Elsasser* integral, it is zero unless:

1. $\alpha + \beta + \gamma$ is odd;
2. α, β, γ can form the sides of a triangle;
3. one or more of the $m_\alpha \pm m_\beta \pm m_\gamma$ vanishes;
4. none or two of the harmonics has the $cos(m\phi)$ term ($m = 0$ counts as $cos(m\phi)$)

and,

5. no two harmonics are identical.

Examples

Figure 1-6 shows an interaction diagram involving only a degree one zonal flow pattern (T_1^0) pattern acting on the axisymmetric poloidal magnetic field (P_l^0), which can generate zonal toroidal magnetic fields (T_{l-1}^0 and T_{l+1}^0). This is an example of field creation through *Adams-Gaunt* integrals (i.e., $T_\alpha P_\beta T_\gamma$).

Furthermore, if we keep the flow field (i.e. T_1^0) and consider non-axisymmetric magnetic fields (i.e. $m_\beta \neq 0$, then one could have the following diagram 1-7 which shows magnetic field creation through *Adams-Gaunt* integrals ($T_\alpha P_\beta T_\gamma$) and *Elsasser*

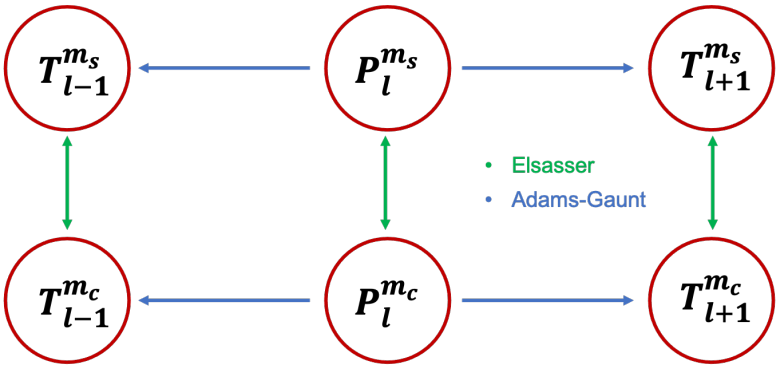

Figure 1-7. Interaction diagram of the Bullard-Gellman formalism. Red circles represent the magnetic field, arrows represent the T_1^0 velocity field where green indicates an Elsasser integral while blue an Adams-Gaunt integral.

integrals ($T_\alpha T_\beta T_\gamma$ and $P_\alpha P_\beta P_\gamma$).

1.4.2 Core Dynamics

Next we review the Navier-Stokes equation which governs the dynamics of the electrically conducting fluids in the dynamo region. In planetary dynamo studies, fluids are examined in a rotating sphere, where fictitious forces are introduced to account for the non-inertial reference frame. The acceleration of the fluid parcel in an inertial reference frame with rotational angular velocity $\mathbf{\Omega}$ is

$$\frac{d\mathbf{u}'}{dt} = \frac{d\mathbf{u}}{dt} + \underbrace{2\mathbf{\Omega}\times\mathbf{u}'}_{Coriolis} + \underbrace{\frac{d\mathbf{\Omega}}{dt}\times\mathbf{r}}_{Poincaré} + \underbrace{\mathbf{\Omega}\times(\mathbf{\Omega}\times\mathbf{r})}_{centrifugal} \tag{1.35}$$

where $d\mathbf{u}/dt$ is the acceleration in the rotating frame. In most cases, the Poincare term is comparatively small so it is often ignored in the Navier-Stokes equation. In the rotating frame of reference, the comprehensive ***Navier-Stokes Equation*** is:

$$\rho\underbrace{\left[\frac{\partial\mathbf{u}}{\partial t}+\mathbf{u}\cdot\nabla\mathbf{u}\right]}_{inertia} + \underbrace{2\rho\mathbf{\Omega}\times\mathbf{u}}_{Coriolis} = -\underbrace{\nabla p}_{*} + \underbrace{\mathbf{J}\times\mathbf{B}}_{Lorentz} + \underbrace{\rho\mathbf{g}}_{buoyancy} + \underbrace{\mu\nabla^2\mathbf{u}+\frac{1}{3}\mu\nabla(\nabla\cdot\mathbf{u})}_{deviatoric\ stress} \tag{1.36}$$

Where ρ is the density of the fluid material, μ the dynamic viscosity and $\mathbf{g}$ is the gravitational acceleration. As can be seen from Eq. 1.36, the fluid motion is governed

under balances between the Coriolis, pressure gradient, buoyancy, Lorentz, inertia and diffusive forces. Notice here instead of pressure, the term $*$ in Eq. 1.36 is the modified pressure gradient which includes the centrifugal acceleration,

$$p = p' - \frac{1}{2}|\mathbf{\Omega} \times \mathbf{r}|^2 \tag{1.37}$$

The density of the fluid parcel ρ is another variable which can be solved through ***conservation of mass***:

$$\frac{\partial \rho}{\partial t} + \nabla \cdot (\rho \mathbf{u}) = 0 \tag{1.38}$$

In practice we choose either (1) the ***anelastic approximation*** where fast motions such as seismic or acoustic waves are filtered out:

$$\nabla \cdot (\rho \mathbf{u}) = 0 \tag{1.39}$$

so this makes logical choice for core convection, or (2) the ***Boussinesq approximation*** where we assume the change of the density is relatively small (e.g. less than one density scale height), and hence that the fluid is incompressible:

$$\nabla \cdot \mathbf{u} = 0 \tag{1.40}$$

By Boussinesq approximation, the viscous force due to deviatoric stress in Eq. 1.36 can be simplified to only one term $\mu \nabla^2 \mathbf{u}$, and we assume density variations are only important in the buoyancy term, resulting in the Boussinesq Navier-Stokes equation:

$$\frac{D\mathbf{u}}{Dt} + 2\mathbf{\Omega} \times \mathbf{u} = -\nabla p + \frac{1}{\tilde{\rho}} \mathbf{J} \times \mathbf{B} + \frac{\rho'}{\tilde{\rho}} \mathbf{g} + \nu \nabla^2 \mathbf{u} \tag{1.41}$$

where the hydrostatic state $\tilde{\rho}\mathbf{g} = \Delta \tilde{p}$ has been subtracted out, and $\nu = \mu/\tilde{\rho}$ is the kinematic viscosity. We define the Ekman number to be the ratio of the viscous force to the Coriolis force to evaluate the relative strength of the viscous force,

$$E = \frac{viscous}{Coriolis} = \frac{|\nu \nabla^2 \mathbf{u}|}{|2\mathbf{\Omega} \times \mathbf{u}|} \tag{1.42}$$

At Eath's core conditions, the viscous force is 16 orders of magnitude smaller than the Coriolis force. However, in order to maintain the mathematical nature of the Navier-Stokes equation that it is a 2nd order partial differential equation, we cannot simply ignore the viscous term. Similarly, the Rossby number

$$R_O = \frac{inertia}{Coriolis} = \frac{|\mathbf{u} \cdot \nabla \mathbf{u}|}{|2\boldsymbol{\Omega} \times \mathbf{u}|} \tag{1.43}$$

gives an estimation of how strong the nonlinear inertia force is compared to the Coriolis force (e.g. $O(10^{-6})$ for Earth's core).

1.4.3 Force Balance

Fluid motion in Earth's outer core is controlled by a balance between the Coriolis, pressure gradient, buoyancy, and Lorentz forces, with smaller contributions from the inertia and viscous forces. For a review of force balances in planetary cores, see Sreenivasan (2010), Jones (2011) and Aurnou et al. (2015). To zeroth order of magnitude, the force balance presents a quasi-geostrophic (QG) balance, i.e. balance between the Coriolis and pressure gradient force. Fluid flows under the influence of only the Coriolis and the pressure gradient force naturally form Taylor columns, where the flows are independent of the direction of rotation axis. This indicates that the flow is essentially two dimensional, in the absence of other forces such as viscous, inertia or Lorentz forces, forming *geostrophic flows* in the spherical geometry.

To first order of magnitude, the force balance is found to be dependent on the dynamo types. Dynamos are categorized into *strong dynamos* if the Lorentz force is comparable to the Coriolis force, or *weak dynamos* if the Lorentz force is considerably smaller than the Coriolis force.

Figure 1-8 shows how different categories of dynamos result in different force balances in their core dynamics. For dynamos with dipole-dominated magnetic fields, the first order of force balance is the Magneto-Archimedean-Coriolis (MAC) balance,

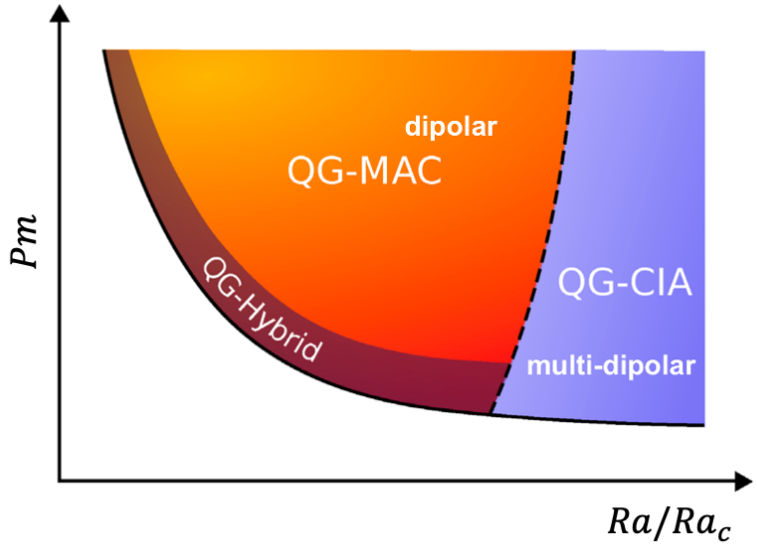

Figure 1-8. Force balance regimes in different types of dynamos. Red-orange region represents dynamos that produce dipolar dominated magnetic field, purple region represents dynamos that produce the multipolar fields. The dark brown region represents the dynamos that are close to onset. Figure adapted from Schwaiger et al. 2019.

i.e. a balance between the Lorentz, buoyancy and the ageostrophic Coriolis forces. To second order of magnitude, viscous and inertia forces make contributions to the force balance. Whereas for dynamos that present multipolar magnetic fields, the Lorentz force becomes a secondary force while the inertia force becomes stronger to balance the ageostrophic Coriolis force, forming a first order Coriolis-Inertia-Archimedean (CIA) balance. For dynamos that are close to onset, the first order force balance is called *hybrid* because part of the fluids lose the MAC balance.

The governing equations can be closed with the inclusion of the energy equation for temperature T,

$$\frac{DT}{Dt} = \frac{H}{\rho C_P} + \frac{k}{\rho C_P}\nabla^2 T \tag{1.44}$$

for Boussinesq approximations, where H represents the internal heating sources or sinks, C_P the specific heat, and κ is the thermal conductivity. In the Boussinesq approximation, the heating due to viscous and joule dissipation are comparatively small and therefore ignored (Malkus, 1973).

Dynamos under the anelastic approximation more often adopt entropy s as the variable of the energy equation.

$$\rho T\left(\frac{\partial s}{\partial t}+\mathbf{u}\cdot\nabla s\right)=\nabla\cdot(\kappa\nabla T)+\underbrace{\Phi_\nu}_{viscous}+\underbrace{\frac{\lambda}{\mu_0}\left(\nabla\times\mathbf{B}\right)^2}_{joule}+\epsilon \tag{1.45}$$

where Φ_ν represents the viscous dissipation and ϵ represents the internal heating sources/sinks.

1.5 Numerical Dynamo Modeling

The set of Navier-Stokes, Magnetic Induction, and the energy equations are non-dimensionalized in numerical dynamo modeling, where different dynamo models could yield different non-dimensional parameters depending on how $\mathbf{u}$, $\mathbf{B}$, T or s are scaled. For incompressible fluids ($\nabla\cdot\mathbf{u}=0$), the equation set under Boussinesq approximation is:

$$\begin{aligned}\left(\frac{\partial}{\partial t}+\mathbf{u}\cdot\nabla\right)\mathbf{u}+2\Omega\times\mathbf{u}&=-\nabla p+\frac{1}{\tilde{\rho}}\mathbf{J}\times\mathbf{B}+\frac{\rho'}{\tilde{\rho}}\mathbf{g}+\nu\nabla^2\mathbf{u}\\ \left(\frac{\partial}{\partial t}-\lambda\nabla^2\right)\mathbf{B}&=\nabla\times\mathbf{u}\times\mathbf{B}\\ \left(\frac{\partial}{\partial t}-\kappa\nabla^2\right)T&=-\mathbf{u}\cdot\nabla T+Q\end{aligned} \tag{1.46}$$

where Q represents internal heat sources or sinks. Taking the dynamo code mMoSST (W. Kuang, 1999; Jiang and Weijia Kuang, 2008) as an example, the fundamental units used in the non-dimensionalization of the model are: the radius of the outer core boundary (i.e. the top of the dynamo region) r_0 as the length scale, the magnetic diffusion time $\tau=r_0^2/\lambda$ as the time scale, $h_T r_0$ as the temperature scale, where $h_T=-\partial T/\partial r$ is the temperature gradient at the inner core boundary, and $(2\tilde{\rho}\Omega\mu_0\lambda)^{1/2}$ as the magnetic field scale. This results in the non-dimensional equations:

$$R_0(\partial_t+\mathbf{u}\cdot\nabla)\mathbf{u}+\mathbf{e}_z\times\mathbf{u}=-\nabla p+\mathbf{J}\times\mathbf{B}+E\nabla^2\mathbf{u}+R_{th}\Theta\mathbf{r} \tag{1.47}$$

$$(\partial_t-\nabla^2)\mathbf{B}=\nabla\times(\mathbf{v}\times\mathbf{B}) \tag{1.48}$$

$$(\partial_t - q_\kappa \nabla^2)\Theta = -\mathbf{v} \cdot \nabla[T_0(r) + \Theta] \tag{1.49}$$

where $\mathbf{e_z}$ is the axial unit vector and Θ is the temperature perturbation field from its mean static field $T_0(r)$. The four non-dimensional parameters are the Ekman number E, the magnetic Rossby number R_o, which measure the strength of the viscous and Lorentz forces relative to the Coriolis force, respectively, the modified Rayleigh number R_{th}, which measures the ratio of the driving buoyancy force to the Coriolis force, and the Prandtl number q_κ which compares the thermal diffusivity against the magnetic diffusivity.

$$\begin{aligned} E &\equiv \frac{\nu}{2\Omega r_0^2} \\ R_o &\equiv \frac{\lambda}{2\Omega r_0^2} \\ q_\kappa &\equiv \frac{\kappa}{\lambda} \\ R_{th} &\equiv \frac{\alpha_T g_0 h_T r_0^2}{2\Omega\lambda} \end{aligned} \tag{1.50}$$

where α_T is the thermal expansion coefficient.

Dynamo models could invoke different scaling schemes. Some common variations of scaling schemes include: the length scale may be taken as the shell thickness of the dynamo region, i.e. $d = r_0 - r_i$, where r_i is the radius of the inner core boundary; the time scale may be taken as the viscous diffusion time $\tau = d^2/\nu$; and temperature scale may be taken as the temperature at the outer core boundary where $h_T = -dT/dr$ is defined as the temperature gradient at the outer core boundary; or the temperature scale may also be taken in terms of the temperature variation $\Delta T = T_o - T_i$ across the dynamo region. The non-dimensional parameters and equations will be varied accordingly, however the physics behind these equations doesn't change. For example, the non-dimensional equations in the *MagIC* (Wicht, 2002; Schaeffer, 2013) code are different than those in *mMoSST*:

$$(\partial_t + \mathbf{u} \cdot \nabla)\mathbf{u} = -\nabla p - \frac{2}{E}\mathbf{e}_z \times \mathbf{u} + \frac{1}{EP_m}(\nabla \times \mathbf{B}) \times \mathbf{B} + \nabla^2 \mathbf{u} + \frac{R_a}{P_r} T \frac{\mathbf{r}}{r_o} \tag{1.51}$$

$$(\partial_t - \frac{1}{P_m}\nabla^2)\mathbf{B} = \nabla \times (\mathbf{u} \times \mathbf{B}) \tag{1.52}$$

$$(\partial_t - \frac{1}{P_r}\nabla^2)T = -\mathbf{u} \cdot \nabla T \tag{1.53}$$

where the four non-dimensional parameters are the Ekman number E, the Prandtl number P_r, the magnetic Prandtl number P_m and the Rayleigh number Ra defined as,

$$\begin{aligned} E &\equiv \frac{\nu}{\Omega d^2} \\ P_r &\equiv \frac{\nu}{\kappa} \\ P_m &\equiv \frac{\nu}{\lambda} \\ Ra &\equiv \frac{\alpha g_0 h_T d^4}{\nu\kappa} \end{aligned} \tag{1.54}$$

where $d = r_o - r_i$ is the dynamo shell thickness, and $h_T = -dT/dr$ is the temperature gradient at the outer core boundary.

1.5.1 Conversion of Non-dimensional Parameters between Codes

It is sometimes necessary to convert the non-dimensional parameters in one numerical code to another with different scaling schemes, to reproduce specific dynamo models in the literature, for example. Here we make the conversion of the non-dimensional parameters from *mMoSST* to *MagIC* as an example. Noting the non-dimensional parameters (Eq. 1.54) in *MagIC* with subscript 1 and those (Eq. 1.50) in *mMoSST* with subscript 2, the first three non-dimensional parameters can be converted straightforwardly:

$$\begin{aligned} E_{\mathbf{1}} &= 2\left(\frac{1}{1-\eta}\right)^2 E_{\mathbf{2}} \\ P_{m\mathbf{1}} &= \frac{E_{\mathbf{2}}}{R_{o\mathbf{2}}} \\ P_{r\mathbf{1}} &= \frac{E_{\mathbf{2}}}{R_{o\mathbf{2}} q_{\kappa\mathbf{2}}} \end{aligned} \tag{1.55}$$

where $\eta = r_i/r_o$ is defined as the ratio of the inner core boundary to the outer core boundary. The conversion of the two Rayleigh numbers is slightly more complex. Under the thermal boundary condition of fixed heat flux, MagIC uses the entropy s to solve the energy equation,

$$\tilde{\rho}\tilde{T}\left(\frac{\partial s'}{\partial t} + \mathbf{u}\cdot\nabla s'\right) = \frac{1}{Pr}\nabla\cdot\left(\kappa(r)\tilde{\rho}\tilde{T}\nabla s'\right) + \frac{PrDi}{Ra}\Phi_\nu + \frac{PrDi}{Pm^2ERa}\lambda(r)\left(\nabla\times\mathbf{B}\right)^2 \tag{1.56}$$

where $\tilde{\rho}$, $\tilde{T}$ is the background state density and temperature, s' the entropy perturbation from its background state, and $Di = \alpha_0 g_0 d/C_p$ is the dissipation number. The Rayleigh number is by default set with entropy flux,

$$Ra = \frac{g_0 d^3}{\nu\kappa} S_{scale} \tag{1.57}$$

where S_{scale} is defined as

$$S_{scale} = \frac{q_0 d}{\rho_0 C_p \kappa} \tag{1.58}$$

where q_0 is the entropy flux at the outer core boundary. Notice that the energy flux (or "heat flux") means energy per unit area, per unit time. Hence, by definition, the entropy flux q_0 is entropy per unit area, per unit time, i.e. the unit should be $J\cdot K^{-1}/m^2\cdot s$.

Denoting entropy S as a function of temperature T and pressure P, then we have

$$\frac{dS}{dr} = \left(\frac{dS}{dT}\right)_P\left(\frac{dT}{dr}\right) + \cancel{\left(\frac{dS}{dP}\right)_T\left(\frac{dP}{dr}\right)} \tag{1.59}$$

where the second term can be ignored under the Boussinesq approximation, so

$$\frac{dS}{dr} = \frac{C_p}{T}\frac{dT}{dr} = \frac{C_p}{\tilde{T}}\frac{dT}{dr} \tag{1.60}$$

That is to say, the entropy gradient is proportional to the temperature gradient. Notice in Eq. 1.60 we replaced the T with $\tilde{T}$, because the temperature can be considered as a constant when we evaluate dS/dr at an instant. Therefore the entropy S variable

in the energy equation can be replaced by the temperature T variable, as they are equivalent. As a result, we can rewrite the Rayleigh number as:

$$\begin{aligned} Ra &= \frac{g_0 d^3}{\nu\kappa} T_{scale} \\ &= \frac{g_0 d^3}{\nu\kappa}\left(-\alpha \frac{dT}{dr}|_{r_0} d\right) \end{aligned} \tag{1.61}$$

Now we can convert between the different Rayleigh numbers:

$$\begin{aligned} \frac{Ra_{\mathbf{1}}}{R_{th\mathbf{2}}} &= \frac{\frac{g_0 d^3}{\nu\kappa}\left(-\alpha \frac{dT}{dr}|_{r_0} d\right)}{\frac{\alpha_T g_0 h_T r_0^2}{2\Omega\lambda}} \\ &= \frac{2\Omega\lambda}{\nu\kappa}\left(\frac{-dT/dr|_{r_0}}{h_T}\right)\frac{d^4}{r_0^2} \end{aligned} \tag{1.62}$$

If there is no internal heating in the dynamo region (i.e. $Q = 0$), then

$$\frac{dT}{dr}|_{r_0} = \frac{-h_T r_i^2}{r_o^2} \tag{1.63}$$

and we have

$$Ra_{\mathbf{1}} = \frac{\eta^2(1-\eta)^4 R_{th\mathbf{2}}}{E_{\mathbf{2}} q_{\kappa\mathbf{2}}} \tag{1.64}$$

Notice that the above conversion of the Rayleigh number is correct only under the conditions of: 1) Boussinesq approximation, and 2) no internal heating. The conversion will be different if there is also internal heating in the dynamo region.

1.5.2 Boundary Conditions

There are generally three kinds of boundary conditions for the three variables, Dirichlet or Neuman boundary conditions or the combined Robin boundary condition. They should be chosen based on the relevant physics of the situation.

Boundary Conditions		
Variables	Physic Property	Boundary Condition
Temperature Difference Θ	Fixed heat flux Fixed temperature	$\frac{\partial\Theta}{\partial r} = 0$ $\Theta = 0$
Velocity field $\mathbf{u}$	Non-slip boundary Stress free or Free slip	$[\mathbf{u}] = 0$ $\mathbf{e}_n \cdot \mathbf{u} = 0$
Magnetic field $\mathbf{B}$	Perfect conducting Perfect insulating Finite conducting	$\mathbf{l}_n \cdot \mathbf{B} = 0$ $[\mathbf{B}] = \mathbf{l}_n \cdot \mathbf{J} = 0$ $[\mathbf{B}] = [\mathbf{l}_n \cdot \mathbf{J}] = \mathbf{l}_n \times \mathbf{J} = 0$

Table 1-II. Different boundary conditions for the energy, velocity, and magnetic fields. $\mathbf{e}_n$ is the norm of the boundaries and [ ] denotes the difference across the boundaries.

It should be noticed that, because we use a much larger Ekman number in numerical modeling, the viscous boundary layer would be overestimated by orders of magnitude than that in the real fluid cores, under the non-slip boundary condition. Hence, the free slip boundary condition may be favored to better match the boundary layers in planetary cores.

1.5.3 Geodynamos

Many aspects of the dynamo process are still unknown due to the following reasons: (1) The governing equations are nonlinear; (2) Planetary dynamos operate in the deep interior with extremely high pressure and temperature conditions; (3) The magnetic diffusive time scale is large (e.g. 10^5 yrs for Earth); and (4) There are a limited number of magnetic field measurements of other planets. For Earth, there is a current model, the *International Geomagnetic Reference Field* (Thébault et al., 2015) as well as paleomagnetic and archeomagnetic models available for a relatively short time (Jackson et al., 2000; Constable et al., 2016), comparing to geomagnetic time scales.

One important tool to understand the dynamo process is numerical simulations. Extreme physical properties of fluids in the electrically conducting shell make numerical simulations with realistic planetary parameters unattainable. However, scaling laws can be used to determine combinations of computationally attainable parameters that can produce a modeled magnetic field with planetary characteristics. Geodynamo models, for example, have been successfully reproduced salient features of the geomagnetic field including its dipolar dominance, spatial power spectrum and temporal characteristics of the variability, despite working in a parameter regime far from the real conditions in Earth's core due to computational limitation. Christensen et al. (2010) looked at the parameter space and quantified the χ^2 criteria to determine the degree of resemblance

of a modeled magnetic field to the geomagnetic field, based on the field morphology at the core–mantle boundary. The χ^2 criteria compare properties of a modeled field to the geomagnetic field, including the concentration of the axial dipole power, the ratio between the equatorial symmetric and antisymmetric field, the ratio between the zonal and non-zonal non-dipole moments, and the magnetic flux at the top of the dynamo region. Davies & Constable (2014) furthermore expanded on Christensen's study and introduced one more criterion by looking at the temporal behavior of the geomagnetic field. Model outputs are useful for comparing the current observational data of the geomagnetic field, or the historical data recovered from ship logs as well as paleomagnetic and archeomagnetic studies of crustal magnetism. This helps us to investigate dynamo process and interior structures in Earth's core.

1.6 Stably Stratified Layers (SSL)

A stably stratified layer (SSL) consists of fluid parcels of various densities that, under gravity, will tend to arrange themselves so the direction of increasing density is parallel to the gravitational acceleration (Cushman-Roisin & Beckers, 2011).

Figure 1-9 presents a simple illustration of the SSL. The radius r increases from the bottom (r_1) to the top ($r_2 = r_1 + h$), in the opposite direction of the gravity ($\mathbf{g}$) and the fluid density (ρ) increment. Suppose we move a fluid parcel from the location r_1 with the ambient density $\rho_0(r_1)$ to the location r_2 where the ambient fluid density is $\rho_0(r_2)$, then we have a fluid parcel that is heavier than its environment ($\rho(r_2) > \rho_2(r_2)$). The net force exerted on this fluid parcel is pointing to the bottom of the fluid, i.e. its own gravity force minus the buoyancy force by its surrounding fluids,

$$g\left[\rho(r_2) - \rho_0(r_2)\right] V > 0 \tag{1.65}$$

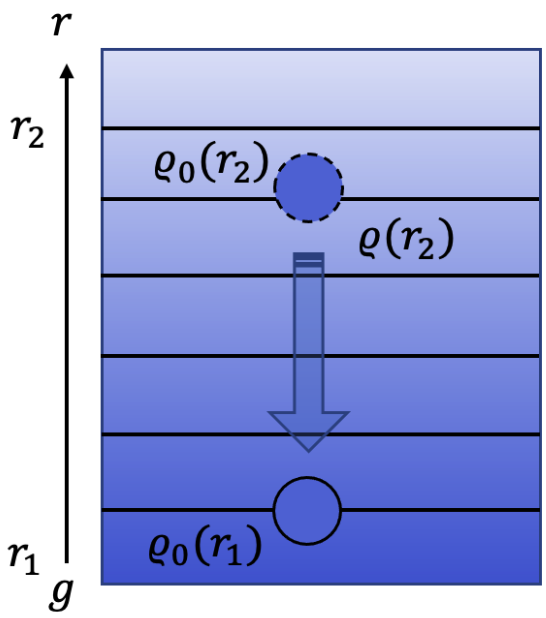

Figure 1-9. Illustration of a stably stratified layer.

Applying Newton's second law, the acceleration of the investigated fluid parcels is

$$\rho_0(r_1)V\frac{d^2h}{dt^2} = g\left[\rho(r_2) - \rho_0(r_2)\right]V \tag{1.66}$$

Given that the density variations across the layer are relatively small compared with the averaged background density, i.e. applying the Boussinesq approximation, we can replace $\rho_0(r_1)$ with ρ_0 (averaged background density) on the left hand side of Eq. 1.66 while keep the density variation in the buoyancy term on the right hand side but replace it with $(d\rho/dr)h$,

$$\frac{d^2h}{dt^2} - \frac{g}{\rho_0}\frac{d\rho}{dr}h = 0 \tag{1.67}$$

If the factor $-\frac{g}{\rho_0}\frac{d\rho}{dr} > 0$, i.e. $d\rho/dr < 0$, then the fluid is stably stratified, and the solution to the Eq. 1.67 instructs fluid oscillations with a characteristic frequency known as the *Brunt-Väisälä frequency*,

$$N^2 = -\frac{g}{\rho_0}\frac{d\rho}{dr} \tag{1.68}$$

On the other hand, if $-\frac{g}{\rho_0}\frac{d\rho}{dr} < 0$, i.e. the fluid is heavier at the top and lighter at the bottom $(d\rho/dr > 0)$, then the solution to the Eq. 1.67 leads to exponential growth.

The fluid parcel placed at r_2 is more buoyant than its surroundings and therefore keeps moving further away from the original location.

1.6.1 Dynamic & Electromagnetic Effect of the SSL

Inside the stable layer, convection of fluid flows is inhibited while lateral flows or differential rotations are possible. When considering electrically conducting fluids inside the SSL of the dynamo region, there is a well known effect called the electromagnetic skin effect (Dynamos 2011) on the magnetic field. Smaller scale magnetic fields often tend to be rapidly varying in time (i.e. high frequencies) so they are filtered by the SSL; whereas larger scale fields are moving more slowly in time (i.e. low frequencies) so they can pass through the SSL. As a result, the magnetic field outside the SSL lacks high resolution features and appears more axisymmetric.

1.6.2 Origins of the SSL

A stably stratified layer can result from two sources: (a) thermal stratification, i.e. a subadiabatic temperature gradient due to high thermal conductivity; or (b) compositional stratification, i.e. enrichment of light elements relative to the bulk materials in the convective dynamo region. A thermally stratified outer core has been proposed to exist on Earth (Lister & Buffett, 1998; Gubbins et al., 2015), and on Mercury to explain Mercury's weak surface magnetic field (Christensen, 2006; Christensen & Wicht, 2008).

For compositional stratification, there are a few mechanisms that have been proposed to explain the origin of a SSL atop the dynamo region.

1. During the inner core crystallization, incompatible light elements are expulsed from the inner core boundary and could rise to the top of the convective core and accumulate over time. Proposed for: Earth (Helffrich & Kaneshima, 2013).

2. Barodiffusion: A diffusion process of the light elements tending to migrate down

the pressure gradient. Proposed for: Earth (Gubbins & Davies, 2013).

3. Core-mantle interaction: Light elements such as Si and O may dissolve from the Fe-bearing lower mantle into Fe metal, and travel towards the outer core through diffusion. Proposed for: Earth (Buffett & Seagle, 2010).

4. Relic of the Moon-forming impact: During the Moon-forming impact, the core materials of the Mars-sized impactor may be lighter than those of the proto-Earth, thus accumulate at the top of the Earth's outer core. Proposed for: Earth (Landeau et al., 2016).

5. Change of solubility of helium: In gas giants, as molecular hydrogen transitions to metallic phase, helium becomes immiscible in hydrogen and precipitates into the deeper interior until it is soluble again. This results in a helium rain layer at the top of the metallic hydrogen-rich shell with a stable compositional gradient. Proposed for: Saturn (Stevenson, 1980; 1982; Christensen & Wicht, 2008; Stanley, 2010), Jupiter (Militzer et al., 2016).

1.6.3 Observational Evidence of SSL

Seismological Evidence

The presence of stably stratified layers can be verified by their influence on the propagation of seismic waves, core flows and the magnetic field. On terrestrial planets, there are a few ways to identify an SSL in the planetary interior. First, the SSL is essentially a type of *density anomaly*, and could be detected through its influence on the propagation of seismic waves. For example, an SSL at the bottom and the top of the Earth's outer core is supported by seismic evidence (Zou et al., 2008; Tanaka & Hamaguchi, 1993). Although for the SSL at the top of the Earth's core, the signal may be polluted with signals from the lowermost mantle such as large low-shear-velocity provinces (Garnero & Helmberger, 1995). Seismic measurements on planets other than Earth are more difficult, although some Marsquakes have been detected by the

InSight lander (Lognonné et al., 2020).

Evidence from Waves and Magnetic Fields

The geomagnetic field could also provide evidence of the stable stratification of the upper outer core, since the core flows in the stable layer are constrained to be lateral, which may favor wave propagations and in turn influence the magnetic field morphology and its secular variation.

For example, studies suggest that the existence of the stable layer may help stabilize high-latitude flux features in the geomagnetic field (Sreenivasan & Gubbins, 2008). The fluctuations of the geomagnetic field with a dominant period of ~ 60 years suggest Magnetic-Archimedean-Coriolis (MAC) waves in a 140 km stably stratified layer at the top of Earth's outer core (B. Buffett, 2014). In Chapter 2, I show the effect of the SSL at the top of Earth's outer core on a large scale feature of the magnetic field, which in turn helps determine the thickness of Earth's SSL.

In addition, Saturn ring seismology (Fuller, 2014) has been utilized to reveal the resonances of ring waves with Saturn's normal mode oscillations, providing evidence of stable stratification in Saturn's fluid interior (Mankovich, 2020). A previous study by Stanley & Bloxham (2016) demonstrated that an SSL at the top of the dynamo region results in slower time variation of the magnetic field, consistent with Saturn's slow secular variation (Cao et al., 2012). In Chapter 3, I show that the presence of a helium rainout SSL may be necessary inside Saturn to explain critical features of its magnetic field.

1.6.4 Numerical Implementation of Stable Stratification

To incorporate both thermal and compositional stratification effects, we use the buoyancy variable C, termed the "co-density", to replace the variable T in the energy equation. The co-density variable combines the buoyancy effects from the perturbations from the core's mean state of the light-element concentration $\Delta\chi_c$ and the temperature

ΔT. The non-dimensional co-density is given by

$$C = \alpha \Delta T + \alpha_c \Delta \chi_c \tag{1.69}$$

where α and α_c are thermal and compositional expansion coefficients, respectively. The gradient of the co-density ∇C thus measures the buoyancy flux. In the convecting region, the reference state co-density gradient can be written

$$\frac{dC_0(r)}{dr} = \frac{\beta^{(b)}}{r^2} + \beta^{(i)} r + \beta^{(s)} r^3 \tag{1.70}$$

where the constants $\beta^{(b)}, \beta^{(i)}$ and $\beta^{(s)}$ define the amount of the bottom, internal and non-uniform specific buoyancy sources separately. The thickness of the SSL is prescribed by the radius R_{bot_SSL} for the onset of stable stratification. The stability of the background static co-density gradient is prescribed by a positive constant A,

$$\frac{dC_0(r)}{dr} = A \tag{1.71}$$

that we vary to adjust the strength of the stratification. The parameter A can be related to the *Brunt-Väisälä frequency* N (Gill, 2016), which is given by

$$N^2 = -g[\frac{\rho g}{\kappa_s} + \frac{1}{\rho}\frac{d\rho}{dr}] \approx -\frac{g}{\rho}\frac{d\rho}{dr} \tag{1.72}$$

where κ_s is the bulk modulus. Keeping the dominant term we can relate the strength of the stratification $N/2\Omega$ to the parameter A:

$$(\frac{N}{2\Omega})^2 \approx R_o R_{th} A \tag{1.73}$$

Figure 1-10 shows an example of the radial profile of the background static codensity gradient, the case implemented in Saturn's helium rainout SSL. The radial profile is plotted as the potential dynamo region and the proposed SSL region, where R_S is the radius of Saturn.

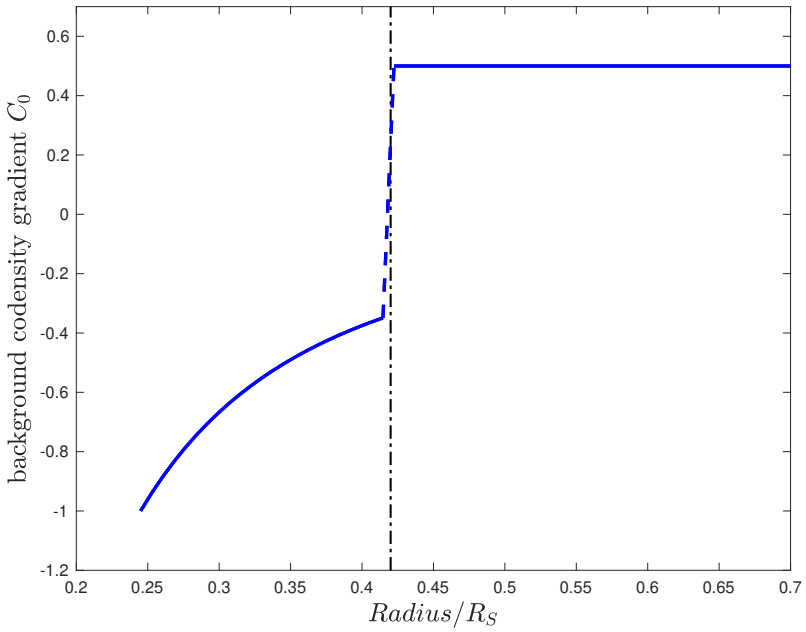

Figure 1-10. Example of the radial profile of the background static co-density gradient where $R_{bot\_SSL} = 0.42$ and $A = 0.5$. In the convective region (0.25 to 0.42), the gradient of the background co-density is the conductive solution without internal heating, while in the stable stratification region (0.42 to 0.7), the gradient is a positive constant to ensure stable stratification.

Chapter 2

Sensitivity of the Geomagnetic Octupole to a Stably Stratified Layer in the Earth's Core

2.1 Introduction

The geomagnetic field is generated through dynamo action operating in Earth's liquid outer core, where convection is driven by thermal and compositional buoyancy forces as Earth slowly cools and the inner core solidifies. Archeomagnetic and paleomagnetic data demonstrate that Earth's field is axially-dipolar dominated on long timescales and exhibits variability on various timescales including westward drift, excursions and aperiodic reversals. Numerical simulations of dynamo action are used to investigate the mechanism responsible for generating Earth's magnetic field. Comparing the results of these simulations to observations of the present and past geomagnetic field provides vital information on processes occurring in Earth's deep interior. Geodynamo models aim to reproduce the salient features of the geomagnetic field including the dipole dominance, spatial power spectrum and temporal characteristics of the variability. Researchers have proposed quantitative criteria for determining whether a simulated field is "*Earth-like*" and determined regions of parameter space where such fields occur (Christen et al., 2010; Davies & Constable, 2014). Models in this parameter space are believed to provide the best insights into Earth's dynamo

processes.

However, one large-scale field characteristic that many Earth-like models cannot reproduce is the octupolar component of the magnetic field (Figure 2-1). Here we use Gauss coefficients to represent the different modes of the magnetic field morphology. Outside the fluid core, where the magnetic field **B** can be represented as the gradient of a scalar potential V, the Gauss coefficients are defined by the expression

$$V(r,\theta,\phi) = r_e \sum_{l=1}^{\infty} \sum_{m=0}^{l} [g_l^m cosm\phi + h_l^m sinm\phi](\frac{r_e}{r})^{l+1} P_l^m(cos\theta) \tag{2.1}$$

where r is radius, θ is co-latitude, ϕ is longitude, r_e is the radius of Earth's surface, g_l^m and h_l^m are Gauss coefficients, l and m are spherical harmonic degree and order, respectively, and $P_l^m(cos\theta)$ are associated Legendre polynomials. The three largest zonal signals are the dipole (g_1^0), quadrupole (g_2^0) and octupole (g_3^0). Following previous studies, we scale the octupole and quadrupole components to the dipole component (g_3^0/g_1^0 and g_2^0/g_1^0) for comparison. A standard Earth-like model tends to produce an octupolar-to-dipolar ratio (g_3^0/g_1^0) that is always positive and larger than observational values over the past 10,000 years. This discrepancy between a standard model and the paleomagnetic model suggests that another ingredient may be necessary in the models to properly simulate Earth's dynamo processes.

Here we investigate whether a stably stratified layer at the top of Earth's core could be that ingredient. The presence of such a layer has long been proposed based on evidence from seismology (Tanaka and Hamaguchi, 1993) and geomagnetic secular variation (Braginsky, 1993; 1999). However, there is disagreement on the thickness and stability of this layer; properties which depend on the stable layer's origins. Recent seismological evidence suggests the layer may be over 300 km thick (Tang et al., 2015; Kaneshima, 2018) whereas secular variation studies suggest a thickness between 60 to 140 km (David Gubbins, 2007; B. Buffett, 2014)). Proposed origins for such a layer include a sub-adiabatic temperature gradient in the upper core due to its high thermal

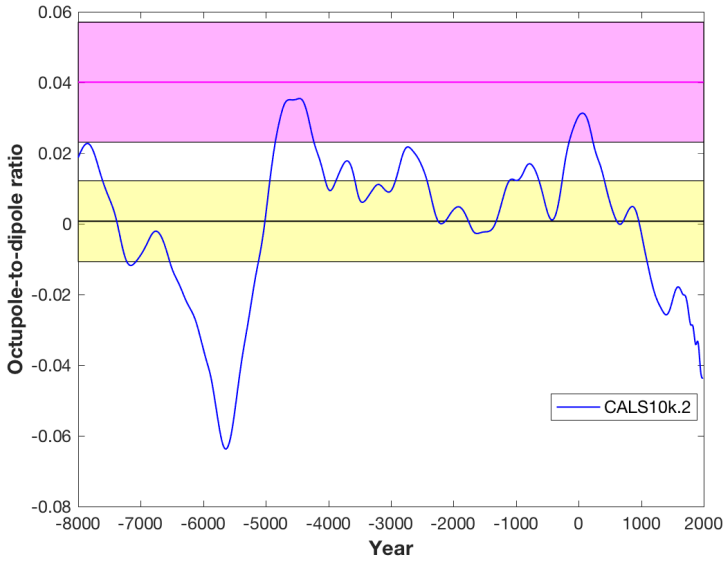

Figure 2-1. The magnetic octupole-to-dipole ratio for paleomagnetic observations from the past 10,000 years from *CALS10k.2* (Constable et al., 2016) and for an Earth-like dynamo model that does not include a stable layer (Model 0 of Table 2-I). The simulation time is redimensionalized through the magnetic diffusion time scale d^2/η to have the same time span as in the *CALS10k.2* model. The magenta line gives the time-averaged value from the model and the shaded magenta region represents the standard deviation about the average. The observational values are shown in the solid blue line with the black line representing the average and the shaded yellow region representing the standard deviation about the average.

conductivity, producing a stable layer with thickness that may range from ~ 100 km (Lister & Buffett, 1998) to ~ 740 km (Gubbins et al., 2015); compositional layering due to light element expulsion from inner core crystallization, resulting in a ~ 250 km thick layer (Helffrich & Kaneshima, 2013); barodiffusion in the core, with a ~ 100 km thick layer (Gubbins & Davies, 2013); or a relic of merging cores from giant impacts early in Earth's history, with a ~ 300 km thick layer (Landeau et al., 2016).

In this study we use numerical dynamo simulations to evaluate the effects of a stably stratified layer at the top of Earth's outer core on the resulting geomagnetic octupole. Details of the numerical methods can be found in Section 2, results in Section 3, discussions in Section 4, and conclusions in Section 5.

2.2 Numerical Methods

We use the MPI-based numerical dynamo model mMoSST (Jiang & Kuang, 2008) to solve the coupled equations governing dynamo action in a fluid, electrically conducting, rotating outer core surrounding a solid, electrically conducting inner core. This model has been shown to reproduce benchmark results (Christensen et al., 2001). Further details on the relevant dynamo equations, non-dimensional parameters and the numerical method can be found in Kuang & Bloxham (1999) and Jiang & Kuang (2008). We additionally implement a stably stratified layer at the top of the core, where the layer stability is maintained through the background co-density gradient, in a similar manner as previous dynamo studies (e.g. Stanley & Bloxham, 2004; Stanley & Mohammadi, **Stanley2008**; Christensen & Wicht, 2008). Further details on the non-dimensional parameters, model equations and implementation of stratification can be found in Chapter 1 Numeric Model Section 1.5, **??**, and 1.6.4.

Due to numerical constraints, dynamo simulations cannot operate with realistic Earth-like parameters. However, scaling laws can be used to determine combinations of computationally attainable parameters that can produce dynamo generation with Earth-like characteristics. Christensen et al. (2010) proposed conditions for an Earth-like dynamo model by defining quantitative criteria evaluating the level of agreement of the output from a numerical simulation with observed properties of the geomagnetic field morphology. We adopt their χ^2 criterion, which is composed of four separate quantities, to evaluate the performance of our models. These four quantities are: (1) the ratio of the power in the axial dipole component to the power in the rest of the magnetic field, (2) the ratio of the power in the equatorially antisymmetric and symmetric magnetic field, (3) the ratio of the power in zonal and non-zonal non-dipole magnetic field, and (4) the concentration factor of magnetic flux at the core surface.

For this study, we consider model C1-4* from Davies & Gubbins (2014), which

Model	Δr (km)	$(\frac{N}{2\Omega})^2$
0	0	0
1	60	$[0 \rightarrow 1.36]$
2	130	$[0 \rightarrow 1.36]$
3	350	$[0 \rightarrow 1.36]$

Table 2-I. Model parameters: Δr is the thickness of the stable layer. $(N/2\Omega)^2$ measures the strength of the stable layer stratification where N is the Brunt-Väisälä frequency and Ω is the angular velocity. Other non-dimensional parameters relevant to the models are held fixed at Ekman number of $E = 1.2 \times 10^{-4}$, Prandtl number $Pr = 1$, the magnetic Prandtl number $Pm = 2$ and the modified Rayleigh number $R_a = 8.33 \times 10^5$ (note that the definition of these nondimensional numbers is given in Chapter 1).

satisfies the χ^2 criterion but does not reproduce the observed g_3^0/g_1^0 ratio (Figure 2-1). We add stable layers of different thicknesses, i.e. 60 km, 130 km and 350 km, and strength of stratification to this model to determine whether it is possible to match both the χ^2 criterion and the g_3^0/g_1^0 ratio. We also examine a case with no stable layer for comparison. Numerical simulation details are listed in Table 2-I. We use the Boussinesq approximation and apply co-density boundary conditions of fixed buoyancy at the inner core boundary (ICB) and fixed buoyancy flux at the core mantle boundary (CMB); no-slip boundary conditions on the velocity field; and magnetic field boundary conditions at the ICB for a finite electrically conducting inner core with equal conductivity to the outer core and at the CMB for an insulating mantle. We use finite differencing in the radial direction with 58 Chebyshev collocation points. Each spherical shell is resolved in latitude and longitude using spherical harmonics with maximum degree and order $l_{max} = 31, m_{max} = 23$. Our models are resolved. For example, simulations with $l_{max} = 50$, $m_{max} = 41$ and 78 radial points produce similar power spectra from degree 1 to 31 and the power in the highest degree $l_{max} = 50$ is 12 orders of magnitude smaller than the power in the lower degree $l_{max} = 31$.

2.3 Results

Figure 2-2 shows the g_3^0/g_1^0 ratio averaged over $10,000$ years for our models. Although we ran our simulations for longer than 10,000 years, we chosen a random 10,000 year window in our simulations to present results here and confirmed that other randomly-chosen 10,000-yr windows produced similar results. The historical g_3^0/g_1^0 ratio from paleomagnetic model *CALS10k.2* is also shown in the yellow shaded region. For the control model with no stable layer, g_3^0/g_1^0 is constantly larger than the values in *CALS10k.2* model and never produces the negative values seen in *CALS10k.2* model. However, for models with a stable layer, the average g_3^0/g_1^0 ratio decreases as the layer stability increases for all values of stable layer thickness we investigated. The ratios tend towards an equilibrium value as $(N/2\Omega)^2$ increases. This suggests that once a layer has become stable enough to fully inhibit convective flows (see Figure 2-7), there is no further effect on the g_3^0/g_1^0 ratio. Examining the cases with different stable layer thicknesses demonstrates that the thicker the layer, the more g_3^0/g_1^0 is impacted, both in terms of average values and variations.

To determine which of our models can reproduce the most Earth-like characteristics, we first exclude models that don't produce the historical g_3^0/g_1^0 ratio, namely, we exclude models that don't produce time averages that are consistent with the observations as well as models that don't produce standard deviations that include both positive and negative values (e.g. the lack of positive g_3^0/g_1^0 values is why models with $\Delta r = 130$ km and $(N/2\Omega)^2 = 0.54$ and 0.68 are excluded even though their mean values are consistent with the observations). This leaves 8 cases out of 33 simulations which are marked by asterisks in Figure 2-2. Next we exclude models that do not meet the quantitative criterion χ^2 from Christensen et al. (2010), leaving 5 cases marked by pentagrams in Figure 2-2 that comply with standards for "good" agreement ($\chi^2 < 4$) between the simulated field and the paleomagnetic model *CALS10k.2* (Table 2-II) as

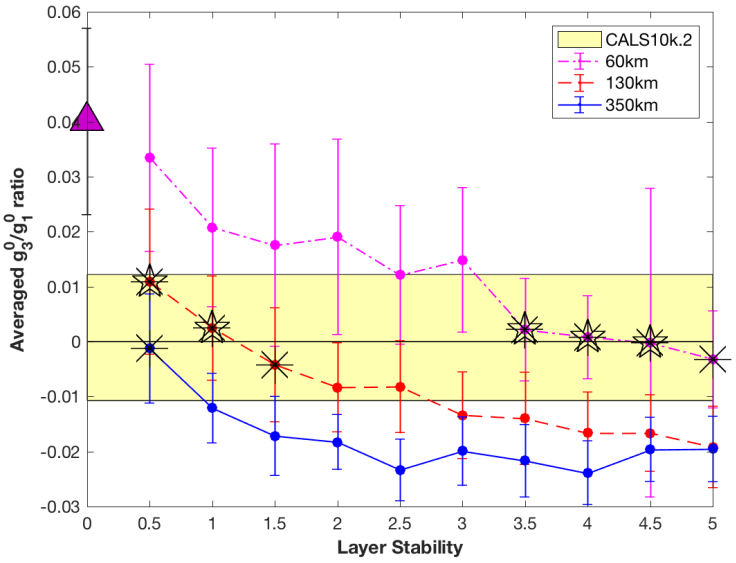

Figure 2-2. The g_3^0/g_1^0 ratio as a function of stable layer properties. The error bars show the standard deviation in time of the g_3^0/g_1^0 ratios about the average values given by the circles. The model represented by a triangle is the control model 0 from Table 2-I with no stable layer. Asterisks mark cases producing compatible g_3^0/g_1^0 ratios compared to *CALS10k.2* and pentagrams mark cases that also meet the criterion χ^2.

well as meeting the g_3^0/g_1^0 ratio constraint. For visualizations of the radial magnetic field, see Figure 2-8(a).

We also investigated the zonal quadrupole to dipole (g_2^0/g_1^0) ratio in our simulations (Figure 2-5, 2-6). A standard Earth-like model without a stable layer is able to reproduce the historic values for this ratio and the addition of a stable layer in our models did not affect the ratio. Our results are therefore also consistent with observations for the quadrupolar field, although this wasn't an issue for the standard model to begin with. The lack of dependence of the zonal quadrupole on the presence of a stable layer may be due to the fact that the zonal quadrupole belongs to a different dynamo symmetry family than the zonal octupole and dipole and is therefore generated by different convective modes.

Previous work has also demonstrated that a spatially variable CMB heat flux pattern can affect the zonal octupole component. For example, a surface spherical

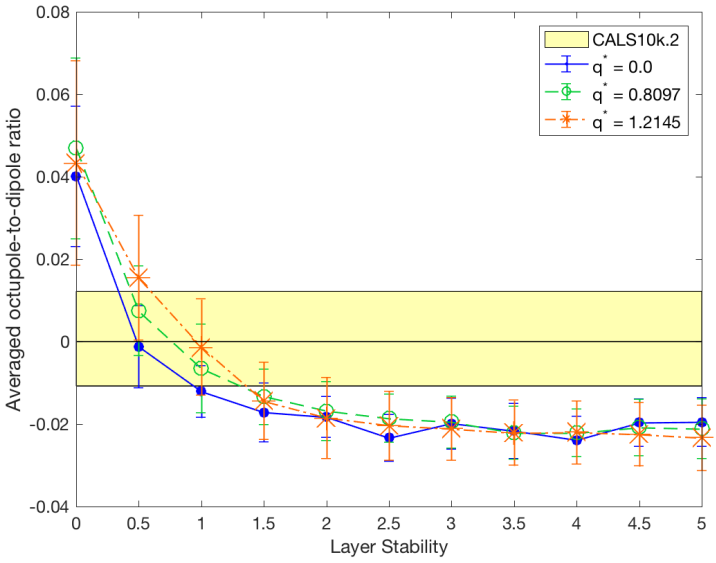

Figure 2-3. The sensitivity of the ratio g_3^0/g_1^0 to the modern day heat flux variation pattern at the CMB, for a model with a 350 km stable layer. The blue line is the same as that in Figure 2-2. q^* is the ratio of the heat flux anomaly divided by twice the average heat flux at the CMB.

harmonic degree-2, order-0 (Y_2^0) pattern of heat flux perturbation at the CMB has been shown to result in a positive g_3^0/g_1^0 ratio that can better match paleomagnetic data from 250 Myr ago (Bloxham, 2000). It is thus necessary for us to examine the possible effects of the CMB heat flux variation over the past 10,000 years to disentangle the possible influences of CMB heat flux variation and the stable layer on the g_3^0/g_1^0 ratio. We have therefore imposed the current era's dominant heat flux signature (Y_2^2 pattern) discerned from mantle tomography on the CMB in our models to investigate the effects on the g_3^0/g_1^0 ratio.

Figure 2-3 shows that: 1) when there is no stable layer, adding a Y_2^2 pattern of heat flux variation doesn't change the average ratio although it causes a larger variation, as suggested previously by Bloxham (2000), and 2) a Y_2^2 pattern of heat flux variation did not significantly affect the g_3^0/g_1^0 ratio in our models. As a result, we conclude that the g_3^0/g_1^0 ratio is insensitive to the largest component of the modern era CMB heat flux pattern.

2.4 Discussion

Our study demonstrates that a stably stratified layer at the top of Earth's core may be necessary to explain the zonal octupolar component of the geomagnetic field over the past 10,000 years. It should be noted that other magnetic models such as CHAOS-4 (Olsen et al., 2014) and gufm1 (Gubbins et al., 2000) have higher spatial and temporal resolutions compared to *CALS10k.2* used in this study. However, those models only cover short time periods (recent decades) and therefore represent more of a snapshot of core processes making it unclear how representative they are of longer-term behavior. We wanted to compare average behavior on longer timescales and the *CALS10k.2* model allowed for that. That being said, if we were instead to assume that the CHAOS-4 and gufm1 models from data over the past couple of decades was a better proxy of the average behavior of the large-scale components of the Earth's magnetic field over the past 10,000 years, then the prediction would be for an octupole-to-dipole ratio of -0.0453 ± 0.0002 which is even further removed from the standard dynamo models without a stable layer than the data from the *CALS10k.2* model. This would suggest that an even larger correction to the models would be needed (e.g. a thicker, more stable layer, or other new features in the model). We therefore feel we are making the conservative choice in this study by using the *CALS10k.2* data as representative of average behavior over the past 10,000 years.

Almost all models with a 350 km thick stable layer fail to match the geomagnetic octupolar constraint. The exception is our model with weak layer stability $(N/2\Omega)^2 = 0.14$ but this model fails to match the Earth-like χ^2 criterion. This suggests discrepancy with recent seismic claims (Tang et al., 2015, Kaneshima, 2018) unless the seismic observations are capturing a physical process that is not being considered in our modeling approach of the stably stratified layer, (in particular, since the models operate in a parameter regime far from that of Earth's core.)

The reason for the stable layer's influence on the octupolar component of the magnetic field resides in the dynamo mechanism itself. Figure 2-4(a) shows that there is amplified power in velocity modes $(l, m) = (3, 0)$ and $(5, 0)$ due to the presence of a stable layer where models with larger layer stabilities lead to stronger amplification in these zonal flows. Dynamically as the stable layer is implemented, it forces thermal wind in the outer core (e.g. see Figure 2-8(b)) to be concentrated into the deeper region of the outer core, which results in a strengthened signature in the zonal octupolar toroidal kinetic energy. However, future studies are needed to scale the modeled zonal flows to these flows in real Earth conditions.

Figure 2-4(b) shows that models with a stable layer only see amplification in the g_3^0/g_1^0 ratio and not other magnetic modes. The amplified octupolar zonal flow can lead to creation of the magnetic octupole field through a two-step dynamo mechanism described with the Bullard & Gellman formalism (1954) as (Details are provided in the Appendix I):

Step 1: $(T_3^0 S_2^{1c} T_1^{1c})$

Step 2: $(S_3^{1s} T_1^{1c} S_3^0)$

Step 1 is described by an Adams-Gaunt integral which involves the octupolar zonal flow (T_3^0) acting on the poloidal magnetic field (S_2^{1c}) to generate a toroidal magnetic field (T_1^{1c}). Step 2 is described by an Elsasser integral where a poloidal flow (S_2^{1s}) acts on the toroidal magnetic field (T_1^{1c}) which was generated in Step 1 to generate the new magnetic zonal poloidal octupole field (S_3^0) that is observed. Similar to the above two-step dynamo mechanism, there are other paths leading to the creation of the magnetic octupole field through the amplified zonal flow in degree 5.

A recent geodynamo study investigating partially stratified regions, where convection can occur locally in a stable layer due to strong thermal influences from the CMB, also found that the octupolar field is affected by the presence of a stable layer. However, they found the g_3^0/g_1^0 ratio increased with layer stability and always produced

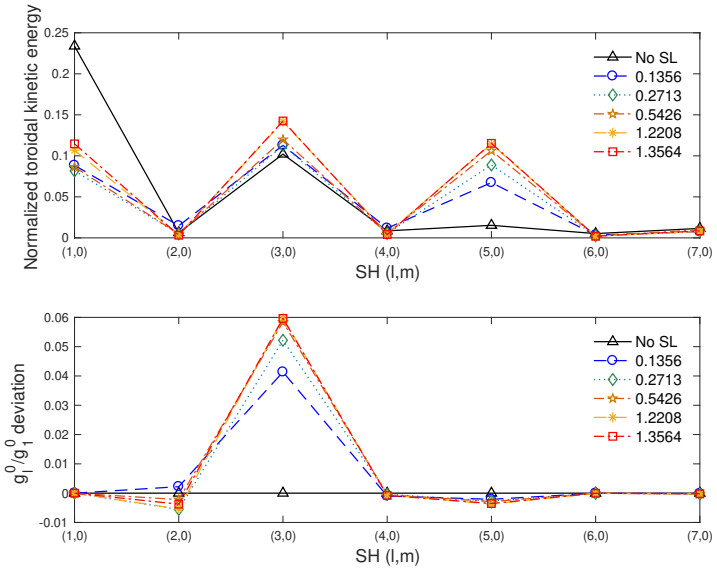

Figure 2-4. (a) Normalized toroidal kinetic energy as a function of zonal spherical harmonic mode and (b) Deviation of the g_l^0/g_1^0 ratio in the 350 km case with different stratification $(N/2\Omega)^2$ values, averaged over 1 magnetic diffusion time. Both x axes list the sequential zonal spherical harmonic (SH) degree, the y axis in (a) shows the fraction of the toroidal kinetic energy of a single mode whereas the y axis in (b) shows the deviation of the g_l^0/g_1^0 in that model compared to the g_l^0/g_1^0 value without a stable layer (SL).

a positive ratio (Olson et al., 2017). Their results would therefore not be consistent with observations, although it was not the purpose of that study to match observations. The reason for the differences between our studies is likely related to the fact that they were performed in different parameter regimes. This demonstrates that the effects we observe may be limited to the specific scenario appropriate to an Earth-like dynamo regime.

The model with 130 km stable layer and $(N/2\Omega)^2 = 0.27$ in this study is similar to the result in Buffett (2014) with a 140 km layer and $(N/2\Omega)^2 \approx 0.26$. However, the level of stratification investigated here is smaller than some previous predictions for what is expected in Earth's stable layer. For example, the Gubbins & Davies' (2013) barodiffusion model has $(N/2\Omega)^2$ ranging from $100 \sim 400$. However, the flattening of the g_3^0/g_1^0 ratios in our results (e.g. in Figure 2-2) suggests that further increasing the stratification in our models would not significantly affect the results. By this point,

the layer is fully stratified with extremely small radial motions (see Figure 2-7). This suggests that there is no entrainment by the underlying convection into the stable region.

It is worth noting that a stably stratified layer might not be the only mechanism affecting the magnetic octupole. For example, Bloxham (2000) found that the Y_2^0 CMB heat flux variation pattern from 250 Ma increases the g_3^0/g_1^0 ratio compared to a model with no CMB heat flux variations. Modern day values of Y_2^0 may be quite small (e.g. Zhang & Zhong, 2011) and hence they may not significantly affect the g_3^0/g_1^0 ratio. However, if they are somewhat comparable to the Y_2^2 amplitude (as suggested in some seismic studies) then the Bloxham (2000) study suggests they would actually work to increase the g_3^0/g_1^0 ratio compared to a scenario with no Y_2^0 heat flux pattern. This could exacerbate the issue of matching the g_3^0/g_1^0 observations with dynamo models and would suggest that an even stronger or thicker stable layer may be needed. In addition, there are previously published dynamo models that do match the χ^2 criterion and the g_3^0/g_1^0 ratio for particular parameter choices. For example, a previous study by Davies et al. (2008) captures the modern-day average g_3^0/g_1^0 ratio in a model with no stable layer, but in a low Rayleigh number regime with relatively large lateral CMB heat flux perturbations that may not be Earth-like. Furthermore, Landeau et al. (2017) finds that the g_3^0/g_1^0 ratio may also depend on inner core size. That study implemented different buoyancy conditions relevant to various potential thermal histories for the inner core and showed that the g_3^0/g_1^0 ratio decreases as the inner core grows through time reaching values similar to present day observations for present day inner core sizes. These studies demonstrate that a stable layer may not be the only potential explanation for the present day g_3^0/g_1^0 ratio, but that other ingredients involving core thermal histories may contribute as well.

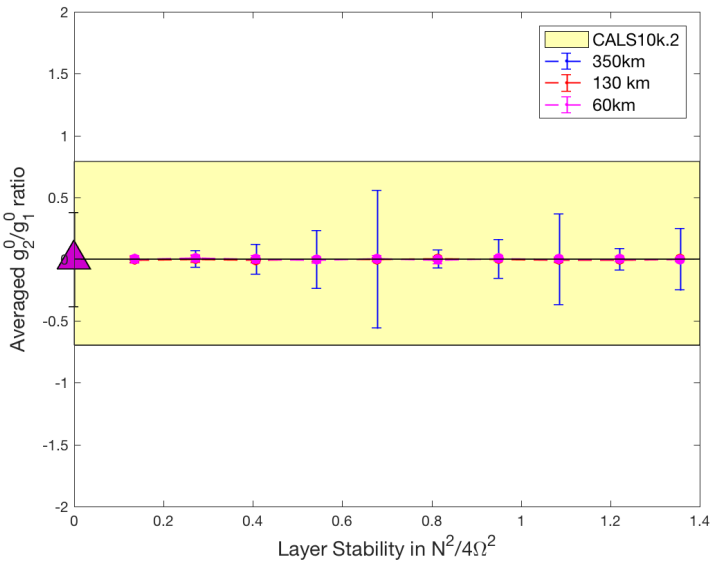

Figure 2-5. The g_2^0/g_1^0 ratio as a function of stable layer properties.

2.5 Conclusion

Our study demonstrates that a stably stratified layer at the top of Earth's core may be necessary to explain the zonal octupolar component of the geomagnetic field over the past 10,000 years. We found that a fairly thin stable layer (60 km) needs to be relatively strongly stratified ($(N/2\Omega)^2 \in [0.95, 1.22]$) whereas a moderately thick layer (130 km) needs to be more weakly stratified ($(N/2\Omega)^2 \in [0.14, 0.27]$). Our model with a 350 km thick stable layer could not match the geomagnetic zonal octupolar constraint and the Earth-like χ^2 criterion.

	layer stratification $(N/2\Omega)^2$										
$\Delta r(km)$, q^*	0	0.1356	0.2713	0.4069	0.5426	0.6782	0.8138	0.9495	1.0851	1.2208	1.3564
60 km	1.0851	0.6499	0.6270	1.4019	1.2453	1.9710	2.2532	**2.8439**	**3.5152**	**3.7153**	4.0938
130 km	0.3676	**1.8701**	**3.6273**	4.8262	5.7901	6.6318	7.0833	7.5562	7.5545	8.0796	8.2228
350 km	0.5934	7.1184	10.347	12.565	14.421	15.848	16.975	17.395	16.783	18.379	18.495
350 km, $q^* = 0.8097$	1.3112	5.9553	7.6981	9.3450	10.679	12.328	12.265	10.143	12.853	14.276	15.110
350 km, $q^* = 1.2145$	1.6347	6.7317	7.5691	8.3400	9.5470	10.512	10.586	11.875	12.092	12.462	12.672

Table 2-II. χ^2 evaluation for our models in Table 2-I as well as the models with core-mantle boundary heat flux variations. The underlined cases are in good agreement with the geomagnetic observations based on the χ^2 criterion. The bold cases match both the χ^2 criterion as well as the g_3^0/g_1^0 ratio constraint. The definition of q^* is in the Figure 2-3 caption.

	layer stratification $(N/2\Omega)^2$										
$\Delta r(km)$, q^*	0	0.1356	0.2713	0.4069	0.5426	0.6782	0.8138	0.9495	1.0851	1.2208	1.3564
60 km	0.0409	0.0335	0.0208	0.0176	0.0191	0.0122	0.0148	0.0022	0.0008	-0.0002	-0.0032
	$\pm$0.0193	$\pm$0.0170	$\pm$0.0145	$\pm$0.0184	$\pm$0.0178	$\pm$0.0126	$\pm$0.0132	$\pm$0.0094	$\pm$0.0076	$\mp$0.0281	$\mp$0.0088
130 km	0.0394	0.0109	0.0025	-0.0042	-0.0084	-0.0082	-0.0134	-0.0140	-0.0166	-0.0167	-0.0192
	$\pm$0.0171	$\pm$0.0132	$\pm$0.0095	$\mp$0.0103	$\mp - 0.0081$	$\mp$0.0084	$\mp$0.0079	$\mp$0.0084	$\mp$0.0075	$\mp$0.0070	$\mp$0.0074
350 km	0.0401	-0.0013	-0.0121	-0.0172	-0.0183	-0.0234	-0.0199	-0.0216	-0.0239	-0.0196	-0.0195
	$\pm$0.0170	$\mp$0.0099	$\mp$0.0064	$\mp$0.0072	$\mp$0.0050	$\mp$0.0056	$\mp$0.0063	$\mp$0.0066	$\mp$0.0058	$\mp$0.0058	$\mp$0.0060
350 km,	0.0470	0.0074	-0.0065	-0.0133	-0.0169	-0.0186	-0.0195	-0.0221	-0.0222	-0.0208	-0.0211
$q^* = 0.8097$	$\pm$0.0220	$\pm$0.0109	$\mp$0.0107	$\mp$0.0067	$\mp$0.0072	$\mp$0.0059	$\mp$0.0063	$\mp$0.0064	$\mp$0.0057	$\mp$0.0068	$\mp$0.0073
350 km,	0.0433	0.0155	-0.0014	-0.0144	-0.0185	-0.0204	-0.0212	-0.0221	-0.0220	-0.0225	-0.0233
$q^* = 1.2145$	$\pm$0.0248	$\pm$0.0151	$\mp$0.0117	$\mp$0.0094	$\mp$0.0098	$\mp$0.0084	$\mp$0.0077	$\mp$0.0079	$\mp$0.0077	$\mp$0.0077	$\mp$0.0080

Table 2-III. Averaged values of the g_3^0/g_1^0 ratio with the standard deviation for our models in Table 2-I as well as the models with core-mantle boundary heat flux variations.

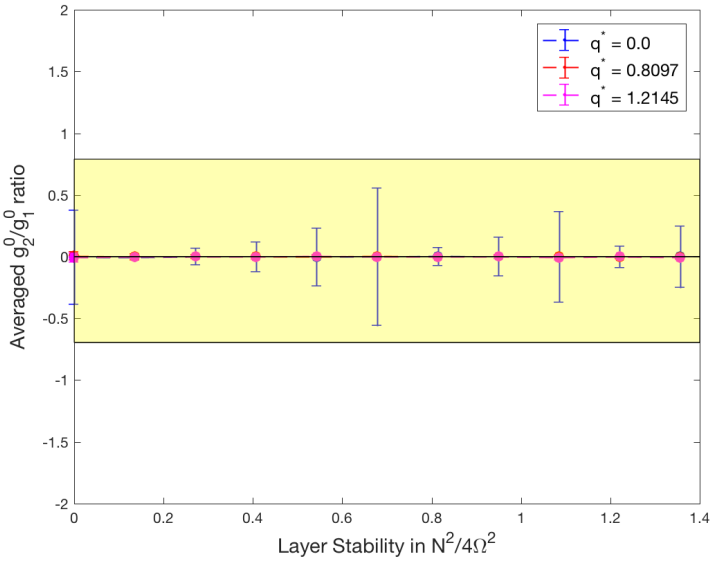

Figure 2-6. The sensitivity of the ratio g_2^0/g_1^0 to the modern day heat flux variation pattern at the CMB, for a model with a 350 km stable layer. q^* is the ratio of the heat flux anomaly divided by twice the average heat flux at the CMB.

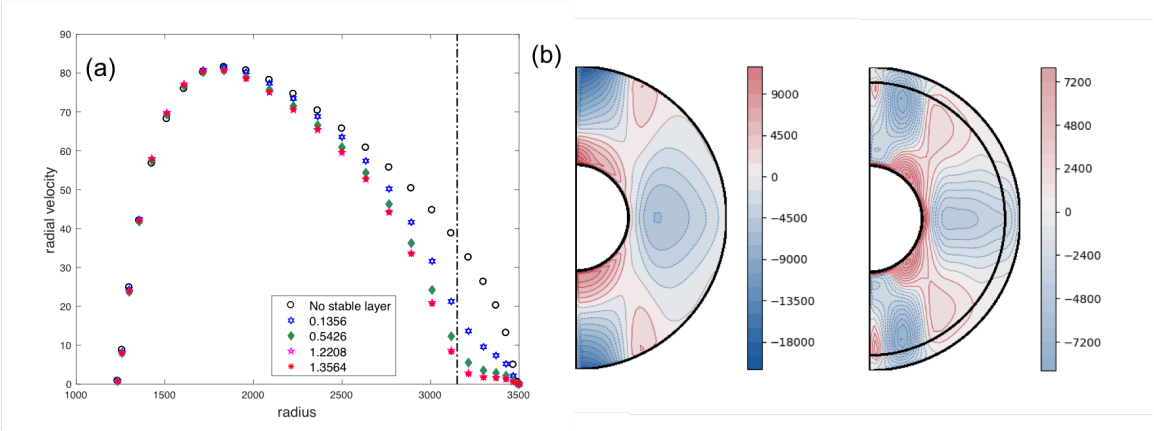

Figure 2-7. (a) The non-dimensional radial velocity $\mathbf{v}'$ profiles in models with a 350 km stable layer and various layer stratification $(N/2\Omega)^2$, where $\mathbf{v}' = \mathbf{v}d/\eta$ for a dimensional velocity $\mathbf{v}$. Note the magnetic Reynolds number in our simulations range from 110 to 150. The x axis shows the outer core region from ICB (1225 km) to CMB (3500 km) whereas the y axis shows the magnitude of the radial velocity averaged over 1 magnetic diffusion time and the spherical surface at each radius. The black dash-dot line marks the boundary of the implemented stable layer (i.e. $r_{CMB} - \Delta r$). (b) The time averaged zonal flows in a model without a stable layer (left column) and with a 350 km stable layer and $(\frac{N}{2\Omega})^2 = 1.3564$ (right column).

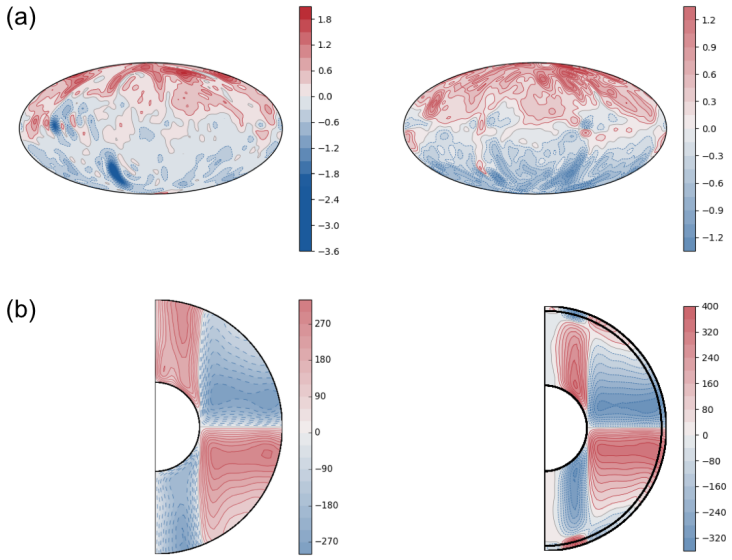

Figure 2-8. (a) Snapshots of the radial magnetic field at the CMB and (b) time-averaged axisymmetric buoyancy wind profiles in a model without a stable layer (left column) and a 130 km stable layer model with $(N/2\Omega)^2 = 0.2713$ (right column).

Chapter 3

Recipe for a Saturn-like Dynamo

3.1 Introduction

Saturn's magnetic field is unique among the planets in our Solar System. First, the field is extremely axisymmetric (Acuña et al., 1980; Ness et al., 1982), with the most recent and detailed observations from the Cassini Grand Finale orbits demonstrating that the surface magnetic field can be well-represented with a purely axisymmetric field up to spherical harmonic (SH) degree 14 (Figure 1) with an upper bound on the non-axisymmetric field contribution of 0.1% (Dougherty et al., 2018; Cao et al., 2020). This level of axisymmetry is problematic in dynamo theory because of Cowling's Theorem (Cowling, 1934), and not typically seen in numerical simulations of dynamo action. In addition, no other planets with active dynamos show this level of axisymmetry, with the possible exception of Mercury (Ness, 1979; Anderson et al., 2012).

Second, the power spectrum of Saturn's surface magnetic field ("Cassini spectrum" in Figure 3-1) shows excessive power in the octupole (SH degree $l = 3$) component compared to the quadrupole ($l = 2$) component, as well as in higher odd degrees (i.e., equatorially anti-symmetric components) relative to adjacent even degrees, except for degree 5. This is unusual because it implies that the power spectrum at the top of the dynamo source region is not flat, i.e., that there is preferential power in specific

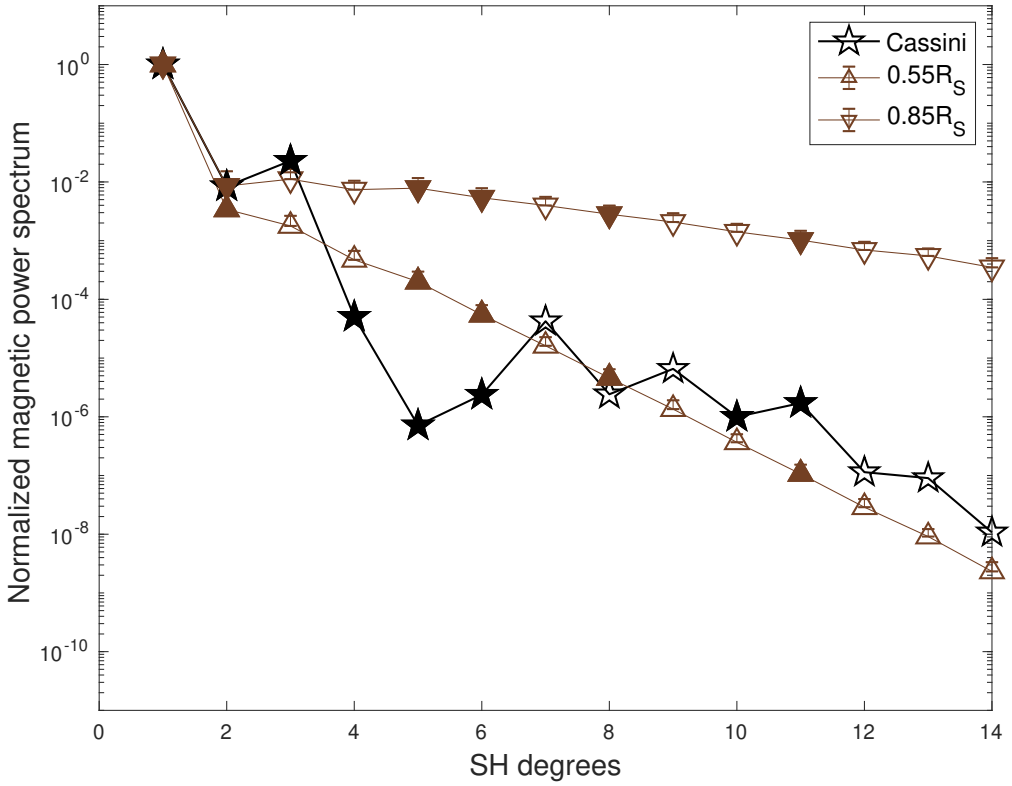

Figure 3-1. Magnetic power spectra for Saturn and control models (i.e. model 0 in Table 1). Pentagrams in black represent Saturn's magnetic power spectrum modeled from Cassini Grand Finale data, namely the "Cassini spectrum" (Dougherty et al., 2018), plotted at $1.0R_S$, where R_S is the 1-bar equatorial radius of Saturn. The upper and lower triangles in brown represent the power spectrum at $1.0R_S$ of a homogeneously convective dynamo model extrapolated from a dynamo surface at 0.55 and $0.85R_S$, respectively. Solid/Open symbols represent positive/negative signs of the zonal Gauss coefficients that make up the spectrum.

modes generated in the dynamo. As demonstrated in our control model (i.e., model 0 represented with triangles in Figure 3-1), power decreases exponentially with spherical harmonic degree at the surface of a planet if there is no preferential power in specific modes.

Third, the slope of Saturn's magnetic power spectrum flattens from degrees 6 to 14 compared to degrees 1 to 5. The trend in Saturn's magnetic power spectrum from degrees 6 to 14 might imply a shallower dynamo surface (Figure 3-1) than that

inferred from degrees 2 to 5 (Cao & Stevenson, 2017), although using spectral slope to determine the depth to the dynamo surface may be inaccurate for gas giants (Tsang & Jones, 2020). A standard convection-driven dynamo model (Figure 3-1) can match the trend in the Cassini spectrum either at low degrees (e.g. 1 to 3), for a shallowly embedded dynamo, or at high degrees (e.g. 7 to 14) for a deeply embedded dynamo. However, it cannot do both simultaneously. This suggests that additional complexity in the dynamo source region is needed to explain Saturn's observed magnetic field.

An additional unique feature of Saturn's magnetic field, not represented in Figure 3-1, is that it appears to change very slowly in time (Cao et al., 2011). Using observations for the past 40 years, the secular variation of Saturn's magnetic field is at least one order of magnitude slower than that of the Earth's magnetic field. This points to unusual dynamics in Saturn's interior, but also emphasizes the importance of explaining the observed spectrum: the features of Saturn's magnetic field revealed by Cassini Grand Finale may be steady in time, representing more than just a snapshot of a more variable field.

These unusual features of Saturn's magnetic field suggest that Saturn's interior dynamics may be different from other planets. Saturn's interior structure and composition are constrained by measurements of the planet's bulk properties, gravity field (Iess et al., 2019; Galanti and Kaspi, 2020), ring seismology (Fuller, 2014), heat flow, and magnetic field. Probable interior profiles (Militzer et al., 2019) can be produced by combining these constraints with equations of state (e.g. Nettelmann et al., 2013) for Saturn's composition developed from experimental and *ab initio* studies. Interior structure models based on available constraints are non-unique and are hampered by our lack of knowledge of material properties at high pressures and temperatures.

As illustrated in Figure 3-2 and 3-7(a), models of Saturn's interior based on available constraints typically include a solid or stably stratified (Mankovich, 2020) icy/rocky inner core, above which a convective, electrically conducting metallic hydrogen-rich

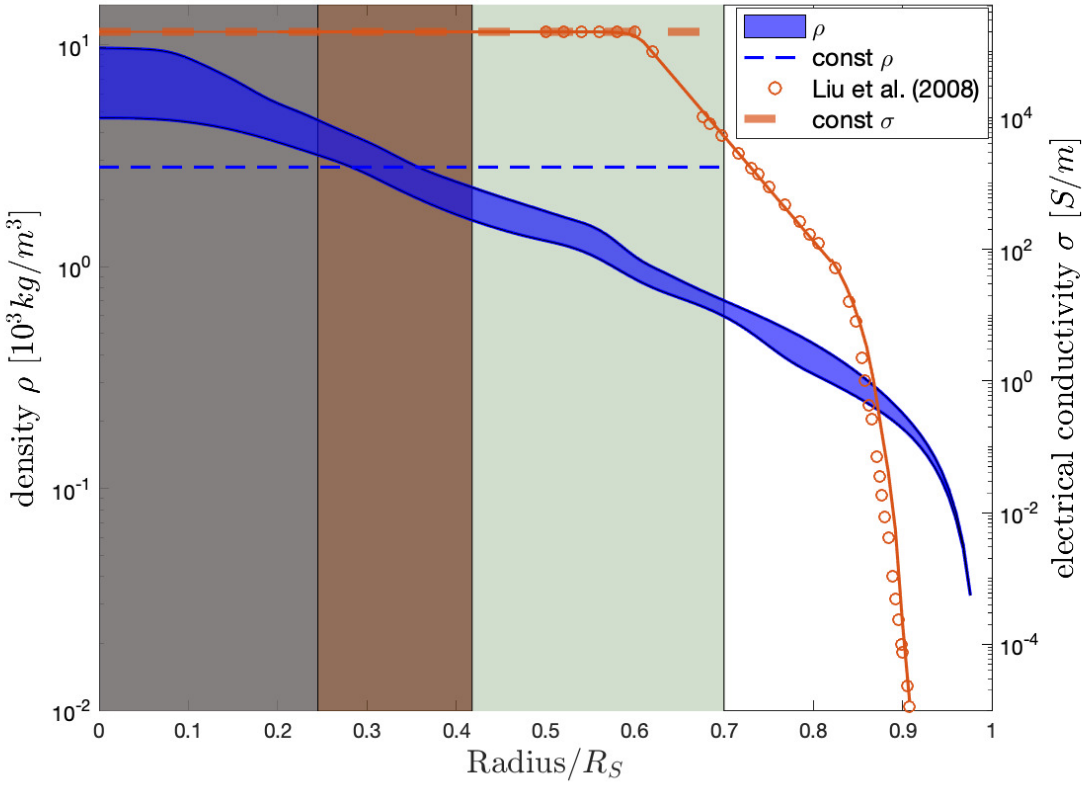

Figure 3-2. Interior properties of Saturn. The filled blue region shows a range of possible density profiles of Saturn based on available constraints (Movshovitz et al., 2020). Circles represent the electrical conductivity data from (Liu, Goldreich, and David J. Stevenson, 2008). Dashed blue (orange) lines represent the constant density (electrical conductivity) used in this study. The shaded regions correspond to the layered structures of model 3 from Table 3-I. From left to right the regions represent the inner core (grey), the convective dynamo region (brown), and the stable layer (light green).

layer generates the dynamo. This region transitions to a surrounding insulating atmospheric layer containing mostly molecular hydrogen.

Ab initio calculations and high-pressure experiments (Vorberger et al., 2007; Morales et al., 2013) show that helium becomes immiscible in hydrogen at approximately $1Mbar$ ($\sim 0.62R_S$) in Saturn. This results in helium raining out of hydrogen forming a layer at the top of the metallic hydrogen-rich shell with a stable compositional gradient tending to inhibit convection. At higher pressures, helium once again becomes miscible in metallic hydrogen, allowing convection and dynamo action in

this deeper region. However, the depth of the dynamo and the thickness of the stably stratified helium rain layer are not well constrained.

The stably stratified layer (SSL) has been proposed as an explanation for the axisymmetrization of Saturn's magnetic field as well as its steadiness, due to the skin effect (Stevenson, 1982; Stanley & Bloxham, 2016). Dynamo models incorporating a stably stratified layer confirm that non-axisymmetric magnetic fields are attenuated in the layer and result in a more axisymmetric magnetic field at Saturn's surface (Christensen & Wicht, 2008; Stanley & Mohammadi, 2008). However, a dynamo model with a stable layer as the only non-standard ingredient does not produce a surface magnetic field as axisymmetric as that of Saturn, nor can it capture the unique morphology of the magnetic power spectrum.

Additionally, strong thermal winds might be expected inside the stably stratified layer as a result of variable heat flux (VHF) perturbations at the top of stable layer. For example, a pole-to-equator heat flux pattern (VHF1,3-7(c)) was first proposed by Stevenson (1982) to be due to solar insolation. While it may be unrealistic for the pattern of thermal perturbations due to solar insolation to penetrate to the top of the dynamo region because of atmospheric convection, it's possible that there is still a remnant of this signal at depth. Alternatively, the same VHF pattern may naturally form at the bottom of the molecular hydrogen envelope, as a result of atmospheric convection (e.g. Aurnou et al., 2008 Soderlund,). A previous study (Stanley, 2010) demonstrated that the surface magnetic field becomes more axisymmetric when there is strong differential rotation occurring in the stable layer as a result of a pole-to-equator temperature gradient at the top of the layer. However, other features in Saturn's magnetic field power spectra are still unexplained.

Here we use numerical dynamo modeling to explore various mechanisms related to the helium rain-out layer that may be acting in Saturn's interior to produce the observed magnetic field. We focus on constraining two 'ingredients' that have been

previously proposed to be important in Saturn's interior: (1) the stability and thickness of a stably stratified helium rain-out layer above the dynamo, and (2) thermal winds in the helium rain-out layer.

3.2 Numerical Methods

Here we use the 3-D numerical dynamo code mMoSST (Jiang & Kuang, 2008) to explore the above two ingredients in an effort to produce a dynamo model that reproduces Saturn's surface magnetic field. We implement a stably stratified layer above the convective metallic hydrogen region and impose various heat flux patterns at the top of the stable layer. The layer stability is maintained by a constant background codensity gradient (see Chapter 1, Section 1.6.4). We then extrapolate the magnetic power spectrum to the surface of the planet and compare it to the Cassini spectrum.

We begin our models with a search through a wide range of values for thickness and stratification of the stable layer to coarsely constrain the stable layer parameters that produce magnetic fields closely matching the dipole tilt and dominant components (i.e., the octupole-to-dipole ratio) of the magnetic power spectrum of Saturn's observed field. The dipole tilt decreases by 40% when a stably stratified layer is implemented but it is not a strong function of stable layer thickness or stratification in the model cases we considered (Figure 3-3). In order to better-match the observed axisymmetry of Saturn's field, we then examine if the dipole tilt can be further decreased by adding a Y_2^0 heat flux perturbation to the top of the stably stratified layer in order to drive thermal winds in the layer. This is motivated by previous work that suggests the dipole tilt is a function of zonal flow strength (Stanley, 2010). We found models with thicker stable layers tend to produce smaller dipole tilts when the heat flux perturbation is present (Figure 3-4). For models with stable layer thickness $\Delta r = 0.62$, there is an optimal range of the VHF1 magnitude $(0.7 - 1.5)$ that produces the smallest dipole tilt. In addition, for models with the same heat flux perturbation amplitude,

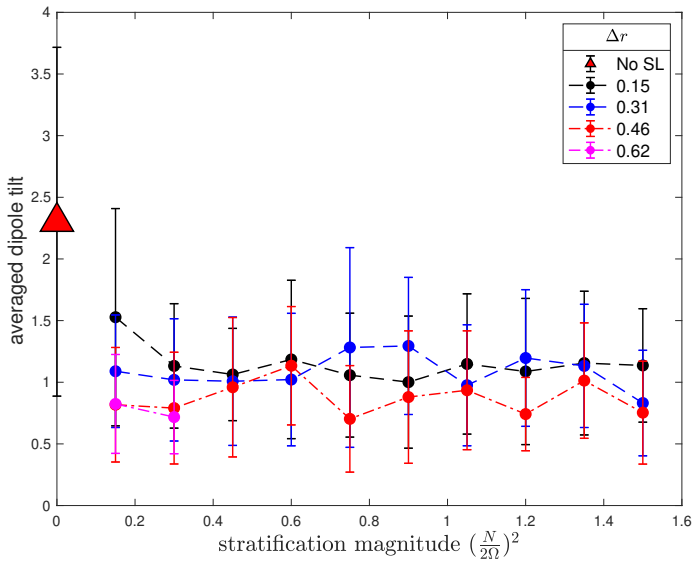

Figure 3-3. The dipole tilt as a function of stable layer properties. The error bars show the standard deviation over half a magnetic dipole diffusion time of the dipole tilt about the averaged values given by circles. The model represented by a triangle is the control model with no stable layer (SL) implemented. Models represented by black (blue/red/magenta) color are models with a $\Delta r = 0.15$ $(0.31/0.46/0.62)$ thick stable layer implemented at the top of the dynamo.

the octupole-to-dipole ratio is typically larger in models with stable layers that are thinner or have weaker stratification (Figure 3-5). A full list of models and detailed procedures are available in Section B, Supporting Information. We then further tune the VHF perturbation by adding smaller scale features in selected models in an effort to match more of the magnetic features. Table 3-I lists the parameter values for models discussed in the text. Further details on the non-dimensional parameters, boundary conditions, implementation of the stably stratified layer and numerical methods can be found in Chapter 1, Section **??**, 1.5, and 1.6.4.

We apply boundary conditions of fixed codensity at the inner boundary and fixed codensity flux at the top of the stable layer; stress-free boundary conditions on the velocity field at both boundaries; and magnetic field boundary conditions for a finite, equal conductivity inner core, and an insulating upper boundary. We use finite differencing in the radial direction with 78 Chebyshev collocation points. Each

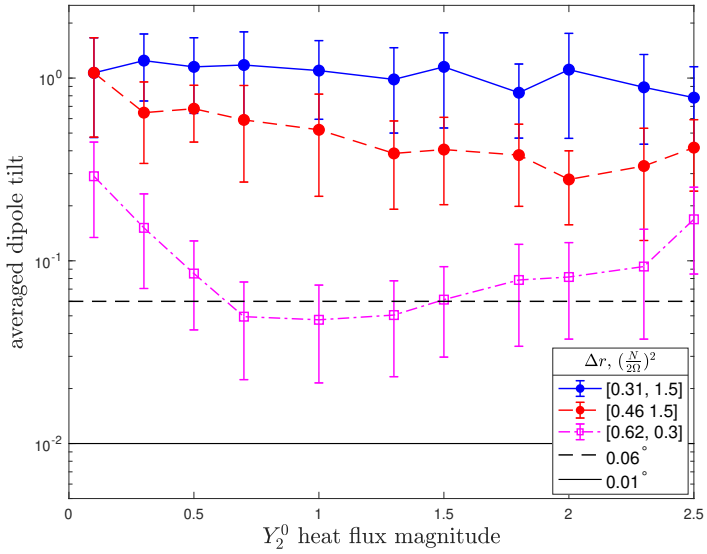

Figure 3-4. The dipole tilt as a function of the VHF1 properties. The error bars show the standard deviation over half a magnetic dipole diffusion time of the dipole tilt about the averaged values given by circles (squares). Models share the same color code with models in Figure 3-3. Circles (Squares) represent models with strong (weak) level of stable stratification $(N/2\Omega)^2 = 1.5(0.3)$.

spherical shell is resolved in latitude and longitude using spherical harmonics with maximum degree and order $l_{max} = 50$, $m_{max} = 41$, respectively. Our models are resolved; the power in degree $l = 50$ is 20 orders of magnitude smaller than the power in the lower degree $l = 15$.

Our models use the Boussinesq approximation, which ignores the density stratification and electrical conductivity variation in the background state. As can be seen from Figure 3-2, the dynamo region ($0.25R_S$ to $0.42R_S$ for the specific model shown) is smaller than one density scale height, demonstrating that the Boussinesq approximation may be reasonable in representing the dynamics occurring in the dynamo region. The stable layer region ($0.42R_S$ to $0.7R_S$ for the specific model shown) is slightly larger than one density scale height, but the dynamics in the stable layer are expected to be dominated by zonal flows whereas density stratification typically affects radial flows. As for the electrical conductivity, our model approximation of

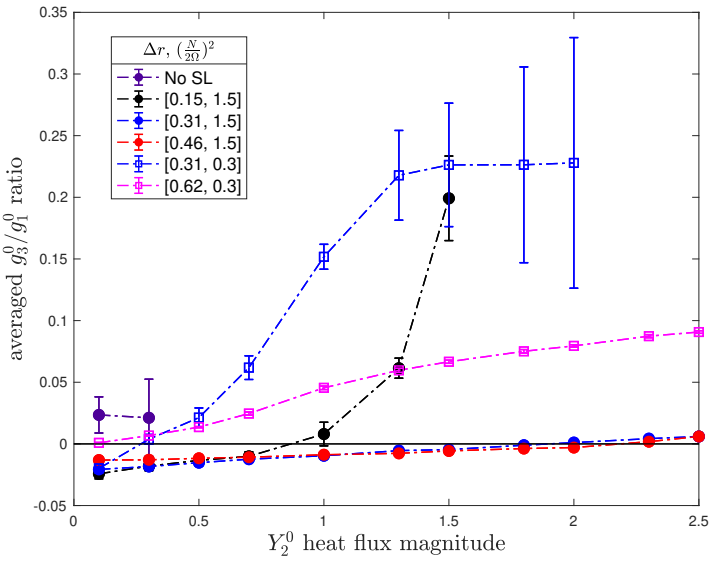

Figure 3-5. The octupole-to-dipole ratio (g_3^0/g_1^0) as a function of the VHF1 properties. The error bars show the standard deviation over half a magnetic dipole diffusion time of the dipole tilt about the averaged values given by circles (squares). Models share the same color/shape code with models in Figure 3-3,3-4, and purple circles represent models without a stable layer. The dynamo core surface is fixed at $0.55R_S$ to ensure models are compared at the same depth so that no bias is brought by different dynamo depth. To extrapolate to different dynamo depth aR_S, the (g_3^0/g_1^0)) values should be multiplied by $(a/0.55)^2$.

constant conductivity is valid below a depth of $0.62R_S$. Although we don't model the exponential decrease of conductivity from $0.62R_S$ to $0.7R_S$. (the outermost region of our stable layer), we don't expect this to have a major effect on our results since most of the axisymmetrization in our models occurs at the base of the stable layer (Figure 3-6).

3.3 Results

Figure 3-8 demonstrates how different ingredients are incorporated into our recipe for reproducing a Saturn-like surface magnetic power spectrum. First, we add a stable layer (model 1 in Table 3-I, $\Delta r = 0.62, (\frac{N}{2\Omega})^2 = 0.3$) at the top of the convective dynamo region and calculate the resulting magnetic field. As shown in Figure 3-

Model	Δr	$(N/2\Omega)^2$	Heat flux patterns	Heat flux magnitude	Dynamo core surface (R_S)	R_{m_rad}	R_{m_zon}
0	0	0	0	0	0.55 (▲) or 0.85 (▼)	6.72	17.96
1	0.62	0.3	0	0	0.85	0.62	6.63
2	0.62	0.3	Y_2^0	1.0	0.7	1.19	106.28
3	0.62	0.3	$[Y_2^0, Y_4^0]$	$[1.3, -0.6]$	0.7	1.08	104.87

Table 3-I. Model parameters: $\Delta r = \frac{R_{top\_SSL} - R_{bot\_SSL}}{R_{top\_SSL} - R_{ICB}}$ is the ratio of the thickness of the stable layer to the dynamo shell. $(\frac{N}{2\Omega})^2$ measures the strength of stratification in the stable layer where N is the Brunt-Väisälä frequency and Ω is the rotation rate of the model.$\sum_{l,m} Y_l^m$ defines the imposed laterally variable heat flux perturbations on the outer boundary of the model where l is the spherical harmonic degree and m is the spherical harmonic order. The dynamo core surface is the inferred depth of R_{top_SSL} for the power spectrum plots in Figure 3-7. R_{m_rad} (R_{m_zon}) is the radial (zonal) magnetic Reynolds number averaged throughout the volume of the stable layer. Other non-dimensional parameters relevant to the models are held fixed at Ekman number $E = 2 \times 10^{-5}$, Roberts number $q_\kappa = 1$, magnetic Rossby number $R_O = 2 \times 10^{-5}$ and modified Rayleigh number $R_{th} = 15000$.

8(a), the power spectrum for the stable layer model demonstrates preferred peaks in the odd degrees (e.g. $l = 1, 3, 5, 7, \ldots$) which do a reasonable job of matching the pattern seen in the Cassini spectrum at higher degrees (e.g. 6 to 14). The amplified equatorially antisymmetric zonal flows in the stable layer favor equatorially anti-symmetric magnetic components producing the odd- harmonic peaks (e.g. Yan and S. Stanley, 2018) in the power spectrum. However, the magnetic energy in the quadrupole and octupole in this model are comparatively small due to field attenuation in the stable layer, with the relative quadrupole being two orders of magnitude smaller than the Cassini observations.

Next, we further impose a Y_2^0 heat flux perturbation (VHF1) in addition to the mean super-adiabatic heat flux at the top of the stable layer (model 2 in Table 3-I). This pattern implies there is lower heat flux coming out of the equator than at the poles (see Figure 3-8(c)). Figure 3-8(b) shows that the addition of the VHF1 at the top of the stable layer generates dynamo action that favors magnetic field in the quadrupolar and octupolar components thereby better-matching the observations. Unfortunately, it also diminishes the peaks in the higher odd SH degrees ($l = 7, 9$). Comparing the total and zonal power spectra, this dynamo model is also more axisymmetric than the

dynamo model with only the stable layer in Figure 3-8(a).

The Y_2^0 heat flux perturbation may not directly affect the magnetic quadrupole component but it may induce various flow patterns that ultimately amplify the quadrupole component 3-9. For example, there is an increase of the axisymmetric degree one poloidal (P_1^0) flow, comparing models 2 and 3 to model 1, which could act on the poloidal magnetic dipole (P_1^0) field, generating poloidal magnetic quadrupole (P_2^0) field. Alternatively, there is another two-step process that could lead to the amplified magnetic quadrupolar field, through the increased degree one toroidal zonal flow in the dynamo region. First, the degree one zonal flow (T_1^0) acts on the degree 1, order 1 poloidal magnetic (P_1^1) field, creating a degree 2 toroidal magnetic field (T_2^1). In the second step, the poloidal (P_1^1) flow acts on the toroidal magnetic field (T_2^1) that was generated in the first step and creates a new poloidal (P_2^0) magnetic field. See I for more details on the Bullard-Gellman formalism.

We further modify the heat flux pattern to include smaller scale features that might be present. We find that a dynamo model with $VHF2 = 1.3Y_2^0 - 0.6Y_4^0$ (model 3 in Table 3-I) produces a power spectrum (Figure 3-8(c)) that best matches the Cassini spectrum in our study. It restores the peaks in magnetic power in higher odd degrees ($l = 7, 9$), while sustaining the power in the lower degrees. We refer to this model as our "preferred" model for Saturn.

The preferred model also produces a magnetic field with very slow secular variation (i.e. it is very steady in time). The secular variations of the preferred model and model 2 are slightly higher than that in model 1 (Figure 3-10), due to the slightly increased radial flows in the stable layer region in these models (Table 3-I), but still much smaller than model 0. The strong zonal flows inside the stable layer act to decrease the secular variation through the electromagnetic skin effect.

Another critical feature of a Saturn-like magnetic field is the signs of the zonal Gauss coefficients. Note that for example, the fact that the octupole (degree 3) has

the same sign as the dipole implies stronger field at the poles compared to a pure dipole field (Cao et al., 2011). For dynamo models with the stable layer and VHF1 pattern, the signs of the largest three zonal degrees (1 to 3) match those of the Cassini spectrum. The addition of the Y_4^0 heat flux pattern reduces the heat flux in the polar regions (colatitude 0-20; 160-180) while increasing the heat flux at the higher latitudes (colatitude 20-40; 140-160), resulting in the smaller scale magnetic field that is more concentrated at higher latitudes due to the same signs of degree 7 and 9, consistent with those of the Cassini spectrum. We find that our preferred model can better match the signs of the zonal Gauss coefficients than the control model (Figure 3-1) and is therefore more representative of Saturn's magnetic morphology.

To evaluate the level of axisymmetry, we compare the magnetic field at the planetary surface of our preferred model (dynamo model 3) to the control model 0. As can be seen in panels (b) and (d) of Figure 3-11, the level of non-axisymmetry is reduced by 2 orders of magnitude in the preferred model, and most of the non-axisymmetry is found in polar regions where the Cassini data is least constrained. The ratio of the non-axisymmetric to the total radial magnetic field is approximately 0.4%, with a major contribution of the non-axisymmetry from low SH degrees 2 to 6; the same order of magnitude as Cassini data (i.e., 0.1% from Dougherty et al. (2018).

Comparing our preferred dynamo model 3 to model 1 with only the stable layer (Figure 3-12), we see stronger thermal winds in model 3. Specifically, the magnetic Reynolds number associated with zonal flows in the stable layer region (R_{m_zon}) of model 3 is almost 15 times larger than that of model 1 (Table 3-I). Such strong thermal winds help significantly axisymmetrize the magnetic field inside the stable layer (Figure 3-6). On the other hand, the radial flows inside the stable layer of model 2 and 3 are slightly increased (R_{m_rad}) in Table 3-I) compared to model 1 due to the addition of the heat flux perturbations, but they are much smaller than the thermal winds and do not affect the axisymmetrization inside the stable layer.

3.4 Discussion

Our study corroborates that a stably stratified helium rain-out layer with heat flux variations at the top of the dynamo region may be necessary to explain Saturn's magnetic observations (e.g., Stevenson, 1982; Christensen, 2006; Stanley & Mohammadi, 2008; Stanley, 2010). In order to axisymmetrize the magnetic field as well as to match the Cassini spectrum, our models suggest that a relatively thick ($\Delta r = 0.62$) stable layer is required with a moderate level of stratification ($(\frac{N}{2\Omega})^2$). Previous work examining the thickness of the stable layer has considered the phase diagram of H-He and its intersection with Saturn's adiabat. This method would give $\Delta r = 0.75$ (Morales et al., 2013; Schoettler & Redmer, 2018; Dietrich & Wicht, 2018). This value is similar although a bit larger than our result. However, assuming an adiabatic profile in the stable layer may overestimate the thickness of the layer, and so our value may be reasonable. In addition, the depth to the top of the stable layer (R_{top_SSL}) that our preferred model requires ($0.7R_S$) is consistent with the depth at which the magnetic Reynolds number is high enough such that flows can affect the magnetic field (Dougherty et al., 2018).

Our preferred model involves a modulated heat flux perturbation ($1.3Y_2^0 - 0.6Y_4^0$) at the top of the stable layer, indicating the possibility of a thermal state more complex than implied from solar insolation alone that exists $17,000$ km deep embedded in Saturn's interior. This modulated heat flux perturbation pattern shifts the maxima of heat transfer from the polar regions (as it would be in the Y_2^0 heat flux perturbation pattern) to the high latitudinal regions at around 57°. Because we find a complex heat flux pattern in the deep atmosphere is necessary to match magnetic field observations, our results suggest a new method to probe the thermal state and winds of Saturn's deep atmosphere.

In the models we present here, we are least able to reproduce the observed power

in the 4^{th} and 5^{th} degrees, although Cao et al. (2020) demonstrates that Cassini data inversions could yield larger magnetic components in the 4^{th} and 5^{th} degrees. Other models we have investigated show that introducing a small amount of north-south asymmetry (e.g. $0.05Y_1^0$) to the total heat flux variation pattern could help to decrease the magnetic energy in degree 5 (see Figure 3-13), although there are trade-offs for matching other features of the field, such as the power in the quadrupole and higher degrees. The remaining discrepancies between our models and the Cassini spectrum suggest that there might be other physical processes (i.e. other ingredients) that are not captured in our recipe for a Saturn-like dynamo, such as a shallower dynamo above the stable layer (Cao & Stevenson, 2017; Cao et al., 2020) or radially varying electrical conductivity (Dietrich & Jones, 2018; Wicht et al., 2019).

Another physical process that needs further investigation is double diffusive convection (Leconte & Chabrier, 2012; Debras & Chabrier, 2019) in the helium rain-out layer, where the convective thermal gradient in the stable layer may be comparable to the stable compositional gradient. The allowance of small-scale convection inside the stable layer may help increase the magnetic energy content in the higher degrees while keeping the sharp spectral slope in the lower degrees of the magnetic spectrum.

It is also worth noting that the recipe for a Saturn-like dynamo is likely non-unique. First, choices of non-dimensional parameters determine the dynamics inside the dynamo region and further affect the magnetic morphology such as dipolarity and field strength, etc, (Christensen & Aubert, 2006; Olson & Christensen, 2006). Second, anelastic models of gas giant planets show dependencies of the magnetic field morphology of the dynamo region on interior properties such as background density stratification and varying electrical conductivity (Wicht et al., 2019). For example, the dipolar magnetic field dominance in the anelastic dynamo models may depend on the magnitude of the background density stratification and profiles of the electrical conductivity profile (Dietrich & Jones, 2018).

Despite these caveats, our study demonstrates that a relatively thick stably stratified layer with moderate level of stratification and strong thermal winds inside the layer can explain features of Saturn's curious magnetic field.

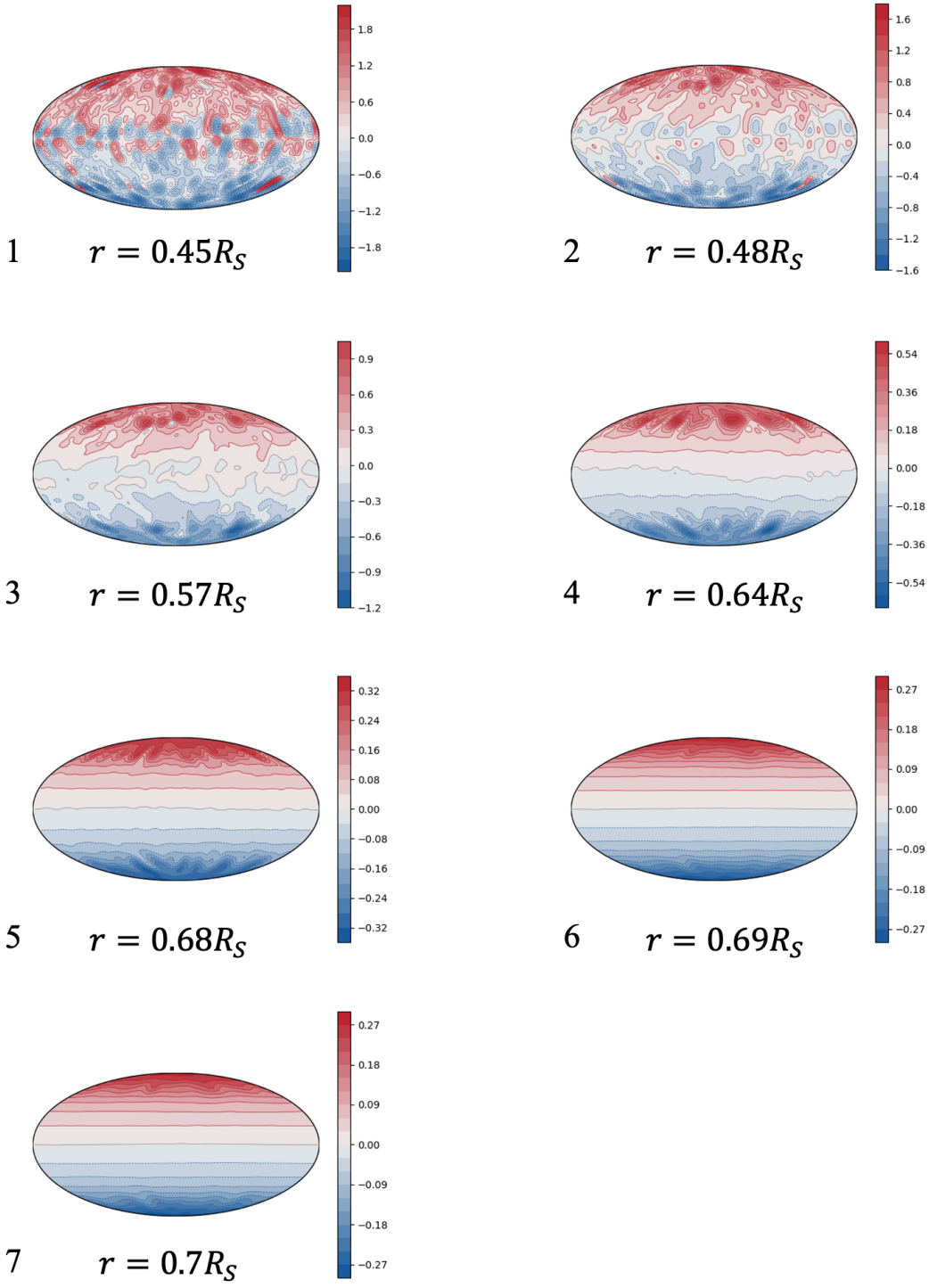

Figure 3-6. The axisymmetrization of the magnetic field through the interior. The radial magnetic fields from the bottom to the top of the stable layer, with the increasing numbering.

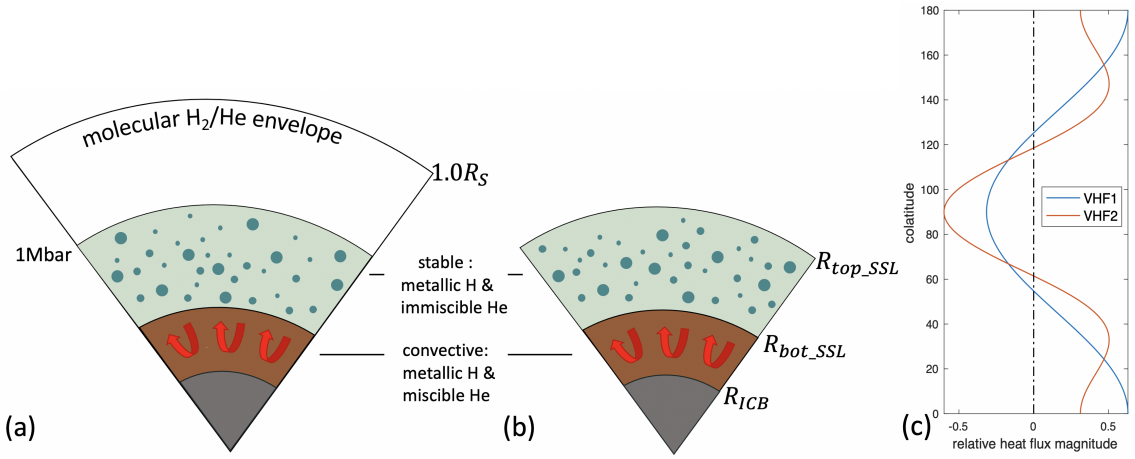

Figure 3-7. (a) Schematic of Saturn's interior structure. From top to bottom, the molecular atmospheric layer is in white, the helium rain layer in light green, the convective and electrically conducting layer in dark brown and the inner core region (which is possibly stably stratified or solid) in grey. (b) The interior geometry used in our numerical dynamo models. Our simulations do not model the molecular H2 He envelope and assume that the inner rocky/icy layer is solid. (c) The heat flux perturbation profiles at the top of the stably stratified helium rain-out layer, as a function of colatitude. Units are non-dimensional.

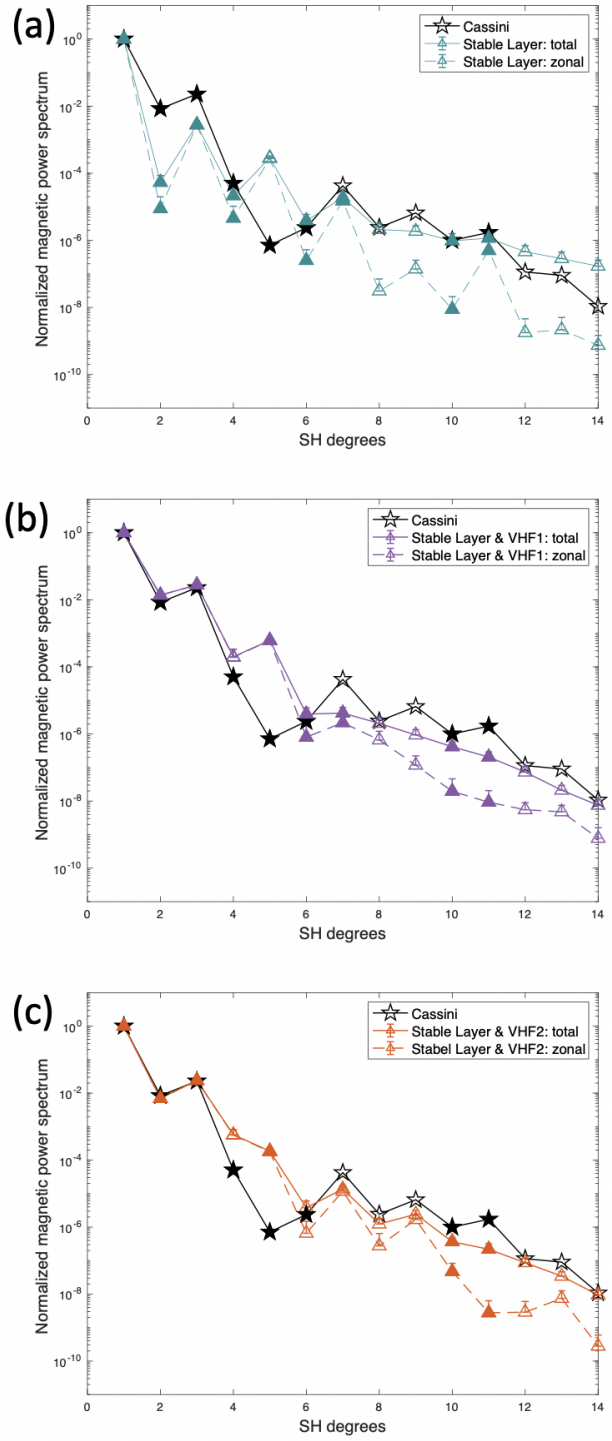

Figure 3-8. Magnetic power spectra at the surface for model 1 (a), model 2 (b), and model 3 (c). Solid lines represent the total magnetic field and dashed lines represent the axisymmetric part of the magnetic field. Solid/Open symbols represent positive/negative values of the zonal Gauss coefficients. The upper error bars represent the standard deviation over half of a magnetic dipole diffusion time of the magnetic power in SH degrees about the average values given by the symbols.

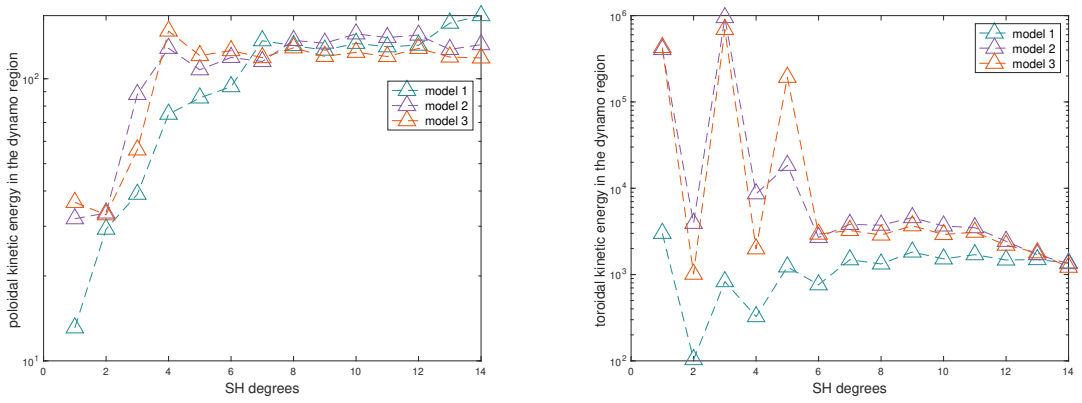

(a) **(b)**

Figure 3-9. (a/b) Poloidal/Toroidal kinetic energy in the dynamo region of model 1 - 3 in Table 3-I.

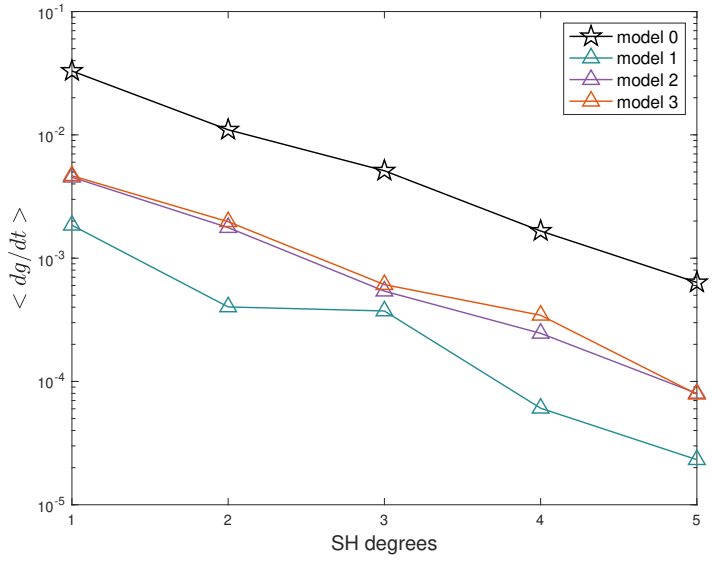

Figure 3-10. The secular variation rates of the individual zonal Gauss coefficients for SH degrees 1 to 5 in our models. The secular variation rates are nondimensionalized by the ratio of the magnetic field scale $((2\rho\Omega\mu\eta)^{1/2})$ to the magnetic diffusion time (r_o^2/η).

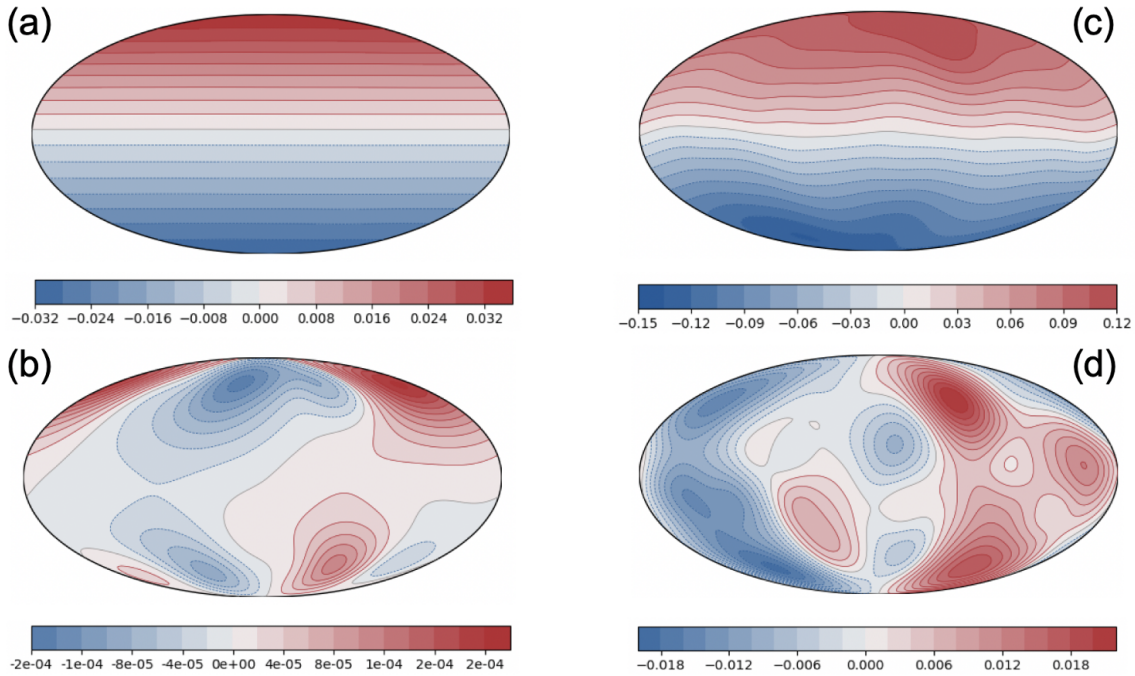

Figure 3-11. Magnetic field at the surface, units are non-dimensional. (a-b) represent the total and non-axisymmetric radial magnetic field components for our preferred model 3. (c-d) represent the same field components for control model 0.

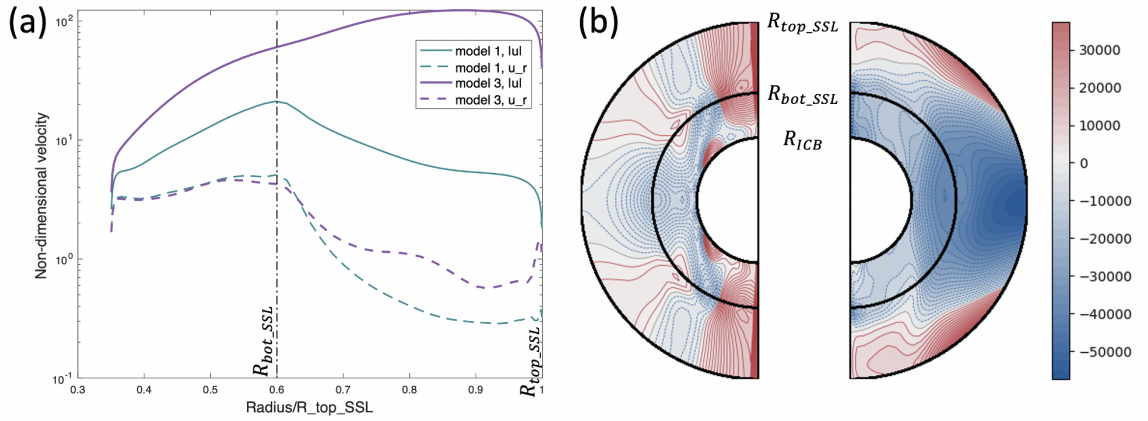

Figure 3-12. Effects of thermal perturbations on zonal and radial flows, units are non-dimensional. (a) Non-dimensional velocity at different radii comparing models 1 and 3; and (b) averaged differential rotation $u_\phi/rsin(\theta)$ or models 1 (left) and 3 (right). The bottom and top of the stable layer are marked by the central and the outer black line.

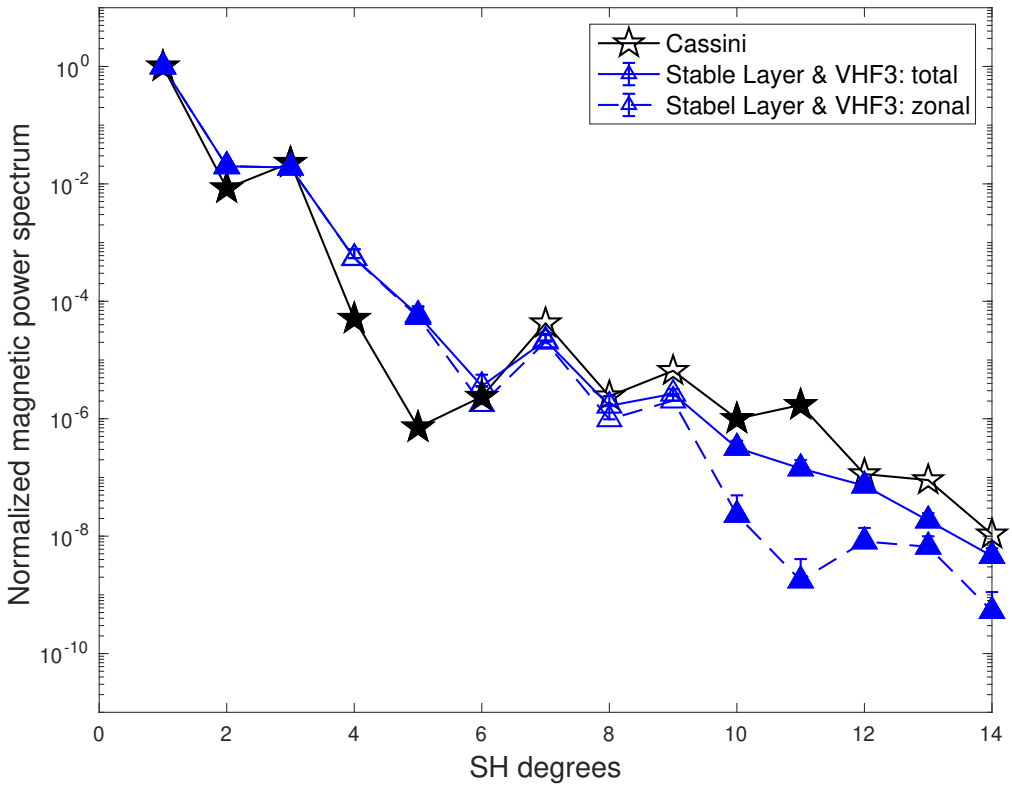

Figure 3-13. Magnetic power spectra at $1.0R_S$ for a dynamo model with a stable layer ($\Delta r = 0.62, (N/2\Omega)^2 = 0.3$) and the heat flux pattern $[0.05Y_1^0 + 1.0Y_2^0 - 0.6Y_4^0 - 0.6Y_6^0]$ at the top of the stable layer for a dynamo core surface at $0.7R_S$.

Chapter 4

The Ancient Martian Dynamo

4.1 Introduction

The magnetic field of Mars was first mapped by the Mars Global Surveyor mission in 1997 (Acuña et al., 1999). Although no present-day dynamo-generated field was seen, global crustal magnetic field anomalies were identified, which likely result from an ancient dynamo in early martian history.

As can be seen in Figure 4-1, strong crustal magnetic anomalies are localized in the southern hemisphere (Terra Cimmeria and Sirenum), while weaker crustal anomalies are distributed in both northern and southern hemispheres. In addition, large impact basins such as Utopia, Hellas and Isidis are demagnetized (Figure 4-1), suggesting the martian dynamo had likely ceased before the remaining impact-heated crust in the youngest of these basins had cooled below its Curie point to be re-magnetized.

The timing of the martian dynamo can be constrained to initiating sometime prior to the end of the late heavy bombardment ($\sim$ 3.9 Ga) from age determinations of magnetized crustal units and 3.9 $\sim$ 4.1 Ga from the age when the oldest martian meteorite Allan Hills ALH84001 when acquired magnetization (Weiss et al., 2002). Recent observations from Mars Atmosphere and Volatile Evolution (MAVEN) detected a magnetic signature coming from 3.7 Ga lava flows in Lucus Planum (Mittelholz et al., 2018). Therefore, the ancient martian dynamo was probably active from

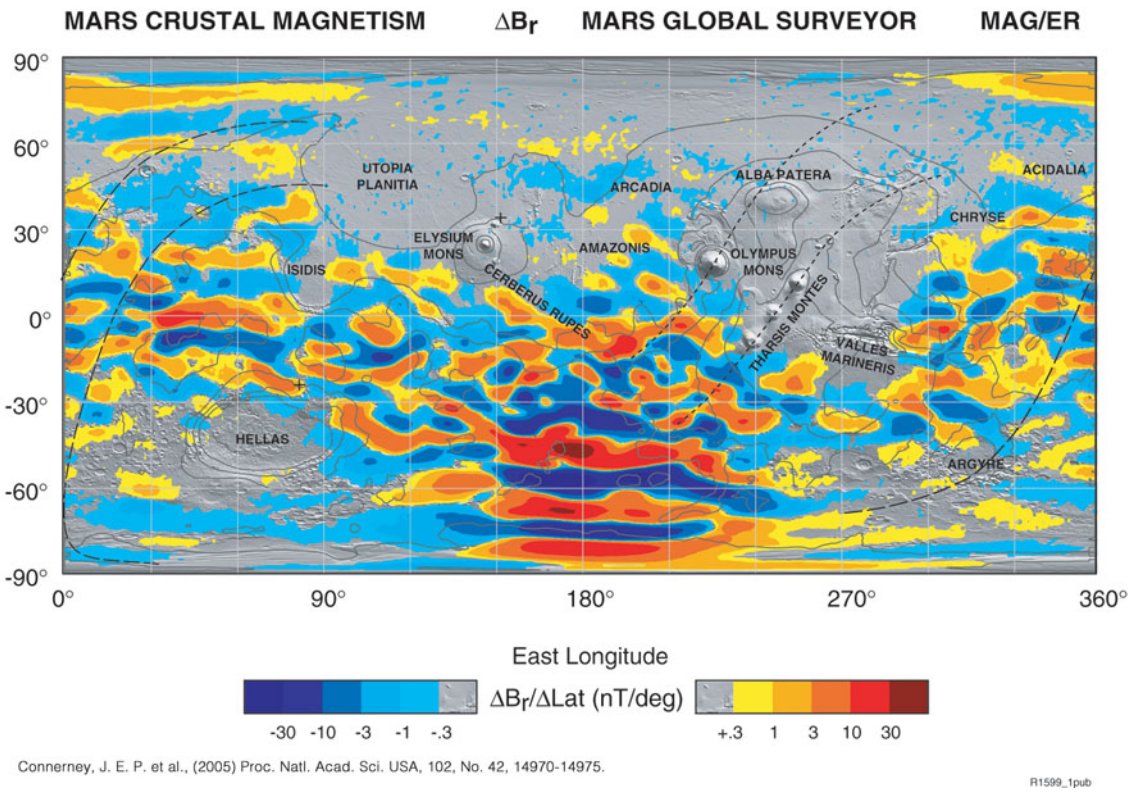

Figure 4-1. Map of the magnetic field anomalies of Mars observed by the Mars Global Surveyor satellite at a nominal 400 km altitude. Where the field falls below the minimum contour a shaded MOLA topography relief map provides context. Figure from Connerney et al. (2005)

sometime since core formation to sometime before the late heavy bombardment, with the possibility of resurrection around 3.7 Ga.

The martian crustal magnetic field is anomalous in several ways. First there is the distinct difference in the crustal magnetic field distribution between the northern and southern hemispheres. There are only weak magnetic field anomalies in the northern hemisphere, while both weak and strong magnetic field anomalies are found in the southern hemisphere. Second, the intensity of the crustal magnetic field in certain continents such as Terra Cimmeria are 10 times stronger than what is observed for Earth's crust (Figure 4-2).

Furthermore, the complex crustal magnetic field contains apparent linear features in the southern hemisphere, especially when viewed in cylindrical projection (Figure

4-1): strong positive field is aligned with strong negative field side by side, continuing for hundreds of kilometers (Connerney et al., 2005). These lineations bear similarities to the magnetic stripes in Earth's mid-ocean ridges which have recorded the polarity reversals of the geomagnetic field as crust has been continuously created along these divergent margins. However, the truth about these stripy features in Mars' southern hemisphere might be less exciting. First, there is no strong evidence of Martian plate tectonics that would lead to such stripes. Second, the surface area in polar regions is amplified in a cylindrical map (e.g. Figure 4-1, therefore the linear features of the Martian crustal magnetic field are exaggerated. When the field is observed in polar projection, the linear features are still there but much less pronounced. In fact, studies such as Nimmo (2000) suggest that such linearized magnetic stripes could be formed through successive dike intrusions.

Here we try to understand one of the most intriguing features of the martian crustal magnetic field: its hemispheric dichotomy, i.e. the crustal field in the southern hemisphere is much stronger than that in the northern hemisphere. There are varying theories attempting to explain the curious north-south dichotomy of the magnetic field, such as impact demagnetization leading to the northern hemisphere being preferentially demagnetized (Nimmo & Gilmore, 2001; Mohit & Arkani-Hamed, 2004), or hydrothermal circulation to connect high magnetization with the water carved valley networks (Solomon et al., 2005). Here we investigate the possibility of the generation of a hemispheric dynamo, i.e. that the dynamo itself produced a stronger magnetizing field in the southern hemisphere. A previous study led by Stanley et al (2008) demonstrated that the crustal dichotomy, i.e. that the northern hemisphere crust is low, thin, and covered with volcanic flows and sediments, while the southern hemisphere crust is high, thick, and lacking large volcanic provinces, could lead to a hemispheric dynamo. Both endogenic (circulation of the mantle, e.g. Zhong et al., 2001; Roberts et al., 2006; Elkins-Tanton et al., 2003; 2005; Ke et al., 2006) or

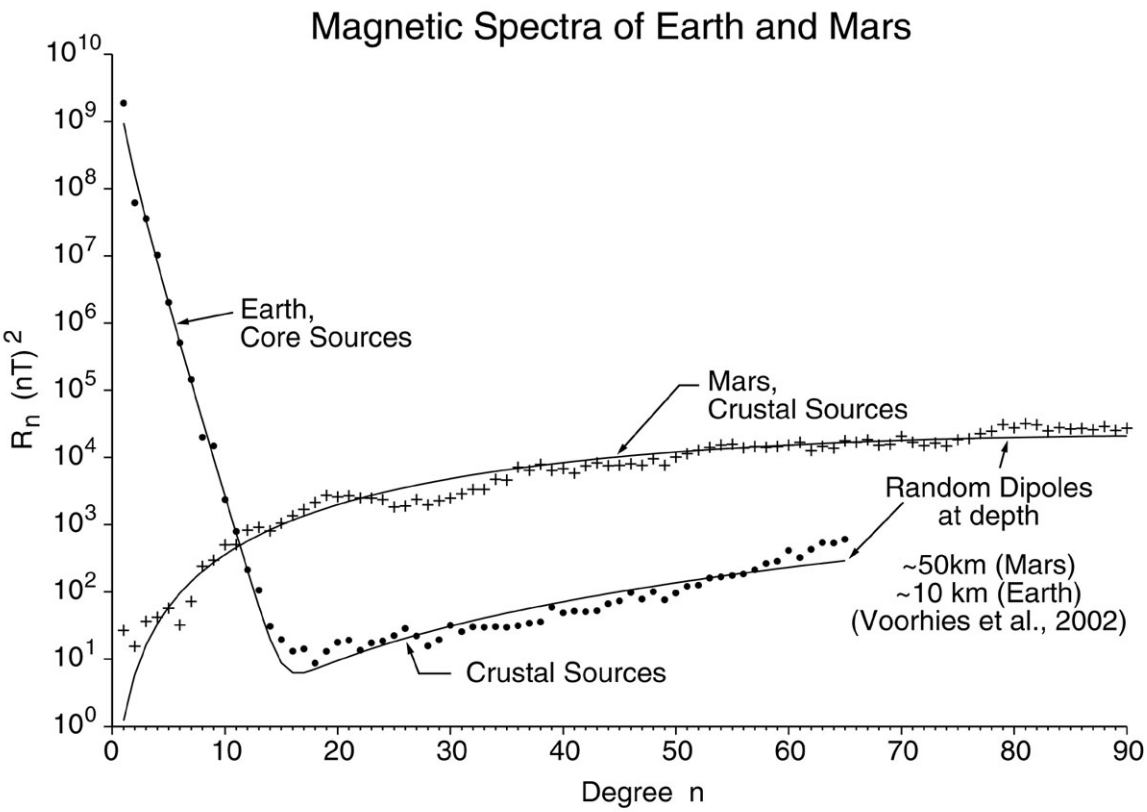

Figure 4-2. Mean square amplitude of the magnetic field on the surface of a sphere of radius a from spherical harmonics of degree n for Earth ($a = 6371$ km) and Mars ($a = 3394$ km). Figure from Voorhies et al. (2002).

exogenic (due to impacts, e.g. Wilhelms & Squyres, 1984; Frey & Shultz, 1988; Nimmo et al., 2008) formation processes could result in more heat flux out of the southern hemisphere than that of the northern hemisphere, resulting the present-day crustal dichotomy.

Previous work (Stanley et al., 2008) has shown that a hemispheric thermal perturbation on Mars' core mantle boundary, where the heat flux is higher out of the southern hemisphere and lower in the northern hemisphere, can result in a hemispheric dynamo which produces a stronger dynamo-generated field in the southern hemisphere. This might be able to explain the observed crustal magnetic field. On the contrary, there have also been competing studies (Dietrich & Wicht, 2013) showing that a

hemispheric dynamo may reverse frequently which would make it harder to explain the observed crustal field, since the stable hemispheric dynamo would produce a crustal field that is strengthened in one hemisphere, but a constantly reversing dynamo would produce a field that observes similar field intensity in both hemispheres.

4.2 Numerical Model

Here we try to use numerical dynamo simulations to first reproduce a magnetic field strengthened in the southern hemisphere, and second, understand the differences between the hemispheric dynamo and the reversing dynamo. We carry out sets of dynamo simulations in a broader parameter space and search for differences between these models. We use the MagIC numerical dynamo model (Wicht, 2002; Schaeffer, 2013) to evaluate how variable heat flux (VHF) perturbation on Mars' core-mantle boundary (CMB) can affect the resulting magnetic field morphology. An example azimuthal slice of the temperature field is shown in Figure 4-3. The relevant equations and non-dimensional parameters for the MagIC code are found in Chapter 1, equations 1.51.

We apply boundary conditions of fixed heat flux at the inner core and core-mantle boundaries; stress-free boundary conditions on the velocity field at both boundaries; and insulating magnetic field at both boundaries. We use spectral methods with 65 Chebychev polynomials in the radial direction. Each spherical shell is resolved in latitude and longitude using spherical harmonics with maximum degree and order $N_\theta = 256$, $N_\phi = 512$, respectively. Table 4-I lists the simulations performed in this study, values of the non-dimensional parameters, heating schemes and boundary conditions.

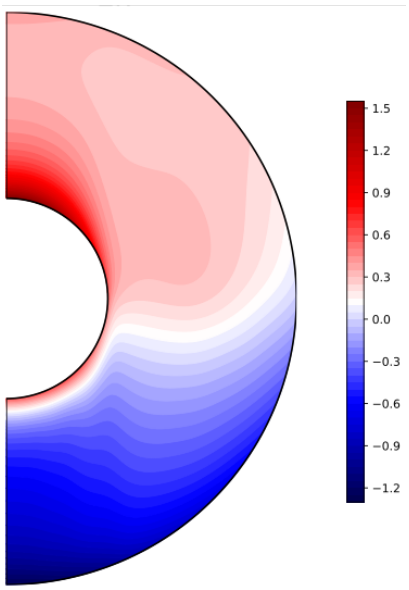

Figure 4-3. An example of the azimuthal slice of temperature due to Y_1^0 VHF subtracting the mean super-adiabatic state.

4.3 Results

4.3.1 Stable hemispheric dynamos

Figure 4-4(a) demonstrates that when the heat flux at the CMB is concentrated in the southern hemisphere, a hemispheric dynamo can result where the magnetic field is stronger in the southern hemisphere. Furthermore, the dichotomy of the magnetic field intensities between north and south hemispheres is not just a result of superposition of different magnetic components so that the field looks stronger or weaker at the surface, but that the magnetic field is preferentially generated in the southern hemisphere than in the northern hemisphere.

It can be seen from Figure 4-4(b) that, with more heat flux coming out of the southern hemisphere, the convection in the southern hemisphere is about 3 to 5 times stronger than in the northern hemisphere. Due to rotational constraints, flows often sustain the columnar shapes, which stretch up to the northern hemisphere. However, there are almost always no flows in the northern polar area.

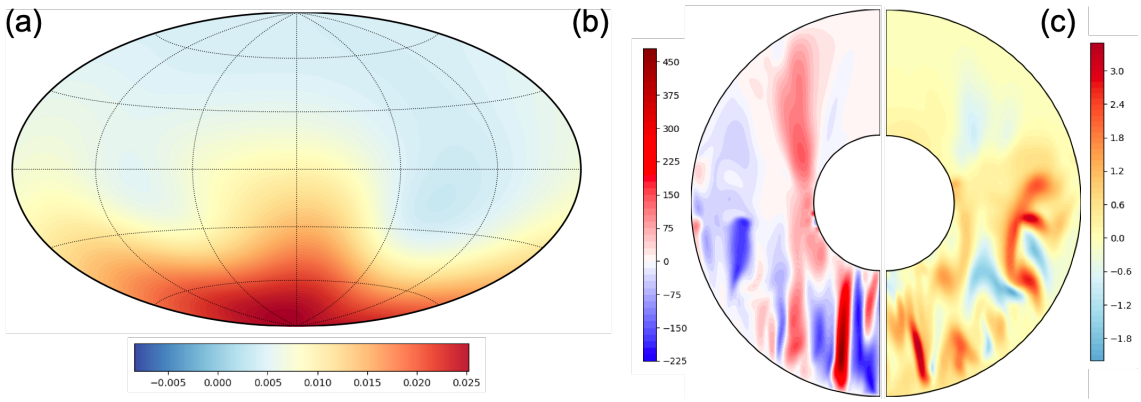

Figure 4-4. Snapshots of the (a) radial magnetic field at the surface, (b) radial velocity field in the outer core, and (c) radial magnetic field in the outer core. Units are non-dimensional.

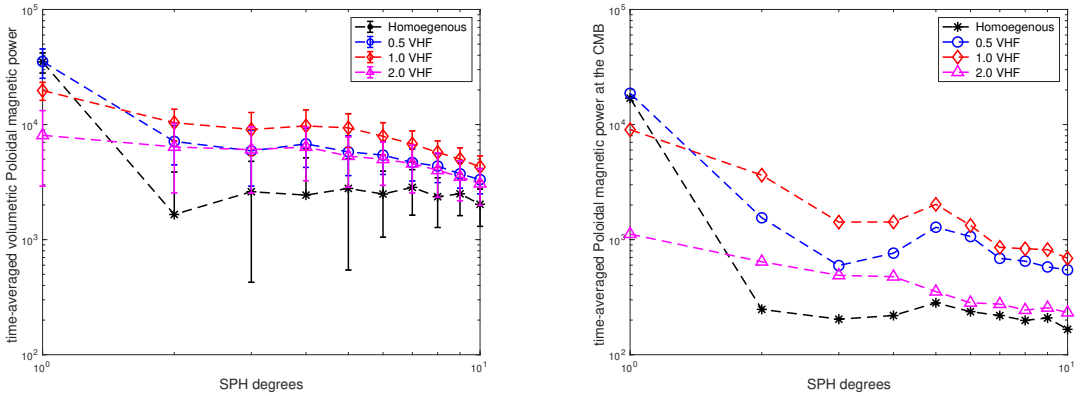

(a) **(b)**

Figure 4-5. The time-averaged power spectrum of the poloidal magnetic field that is (a) averaged throughout the outer core volume; and (b) at the CMB.

We further investigate how increasing the Y_1^0 VHF anomaly affects the resulting magnetic field.

As can been seen from Figure 4-5, when the dynamo model is homogeneously convecting, the magnetic dipole component has a clear dominance over other spherical harmonic degrees. As the magnitude of the Y_1^0 heat flux anomaly starts to increase, the non-dipolar (SH degree l from 2 to 10) magnetic components increase while the dipole component stays the same. As we keep increasing the Y_1^0 heat flux anomaly, the power in the dipole component starts to decrease, which may be a sign for the

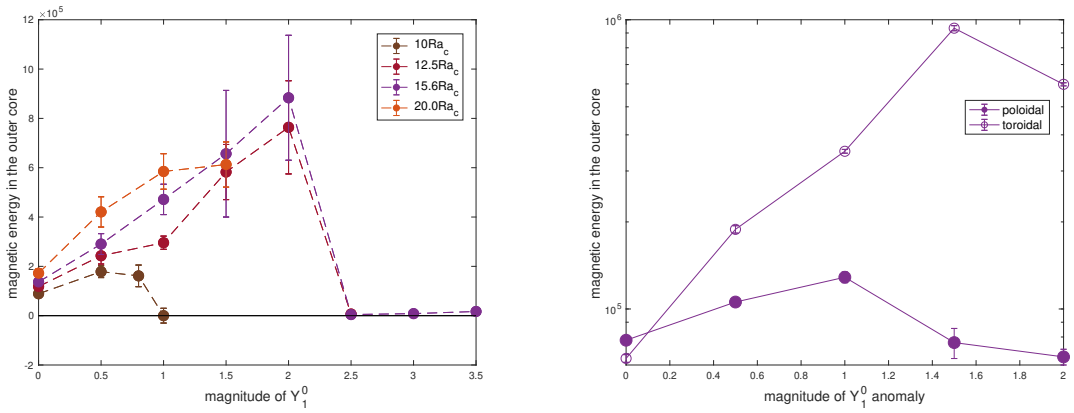

(a) **(b)**

Figure 4-6. Magnetic energy versus Y_1^0 VHF and Rayleigh numbers. (a) The magnetic energy in the outer core grows as a function of the increasing magnitude of the Y_1^0 heat flux anomaly until a critical value where the magnetic field stabilizes to a weaker field. (b) Magnetic energy decomposition into poloidal and toroidal contribution.

transition into "weak dynamos", and eventually the power in larger SH degrees decrease as well.

For dynamo models with increasing Rayleigh number, we can see from Figure 4-6 that, at the same magnitude of the Y_1^0 heat flux anomaly, models with higher Rayleigh number tend to have higher magnetic energy. Moreover, models with higher Rayleigh number tend to produce magnetic fields with a larger magnetic north-south dichotomy (Figure 4-7) and a larger dipole tilt (Figure 4-8).

4.3.2 Influence of heating mechanisms on magnetic field reversals

In the previous section we've shown that a hemispheric magnetic field can result by imposing Y_1^0 heat flux perturbations at the core-mantle boundary (CMB). A previous study (Stanley et al. 2008) has shown similar results. However, there are also studies (Dietrich & Wicht, 2013) suggesting that an imposed Y_1^0 could likely lead to frequent (10 kyrs) polarity reversals of the magnetic field, in which case the intensity of the time-average dynamo field ($|\langle\vec{B}\rangle|$) is zero, insufficient to explain the hemispheric

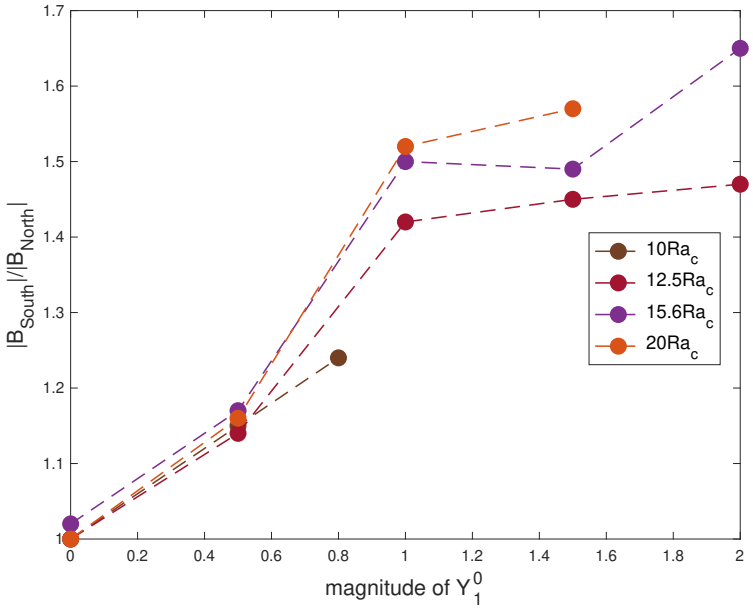

Figure 4-7. The ratio of the magnetic field in the southern to that in the northern hemisphere, as a function of the increasing magnitude of the Y_1^0 heat flux anomaly.

dichotomy of the magnetic field.

Here we aim to understand the dynamo mechanism of the polarity reversals. Specifically, why would Y_1^0 heat flux perturbations at the CMB lead to separate results: (1) a stable hemispheric dynamo, or (2) constantly reversing dynamo in different studies?

We noticed that the different studies used different heating conditions to drive buoyancy. Our models, and those in Stanley et al. (2008) used bottom heating, whereas Dietrich & Wicht (2013) used internal heating. The studies also use different parameter regimes (i.e., different values for non-dimensional parameters). Here we investigate if the difference in buoyancy sources leads to the different results in these papers.

Comparing models 6 and 11 in Table 4-I which are run with the same non-dimensional parameters, we can see that dynamo model 6 that is bottom-heated produces a stable magnetic field with an average dipole tilt around 10°, where the

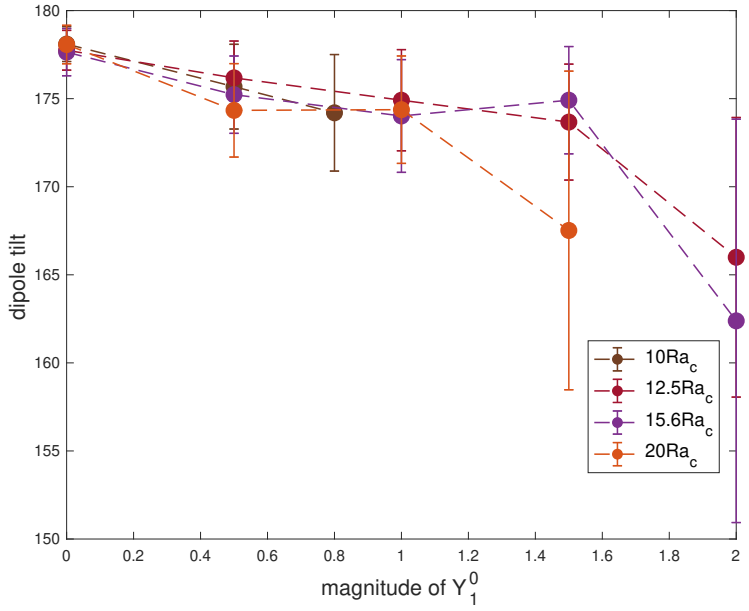

Figure 4-8. The dipole tilt as a function of the increasing magnitude of the Y_1^0 heat flux anomaly.

magnetic field in the southern hemisphere is stronger than in the northern hemisphere (Figure 4-9). However, dynamo model 11 that is internally heated, but otherwise has the same non-dimensional parameters and boundary conditions as model 6, produces an aperiodic, reversing magnetic field. This suggests that the heating mechanism has an important role in determining the stability of the polarity reversal of the field for hemispheric dynamos. This is not too surprising since previous work has demonstrated that internally heated dynamos have different dipolarity scaling relations compared to bottom-heated models (Christensen et al., 2006).

We further looked at the radial velocity field in the two models to understand why the heating mechanism could affect the polarity reversals. Figure 4-10(a & c) show the radial velocities of model 6 and 11 in the equatorial plane. We can see that the flows in the bottom heating model 6 are larger scale towards the inner core, whereas flows in the reversing heating model 11 are relatively smaller scale and are evenly distributed throughout the core. We could then map the velocity field to the spectral

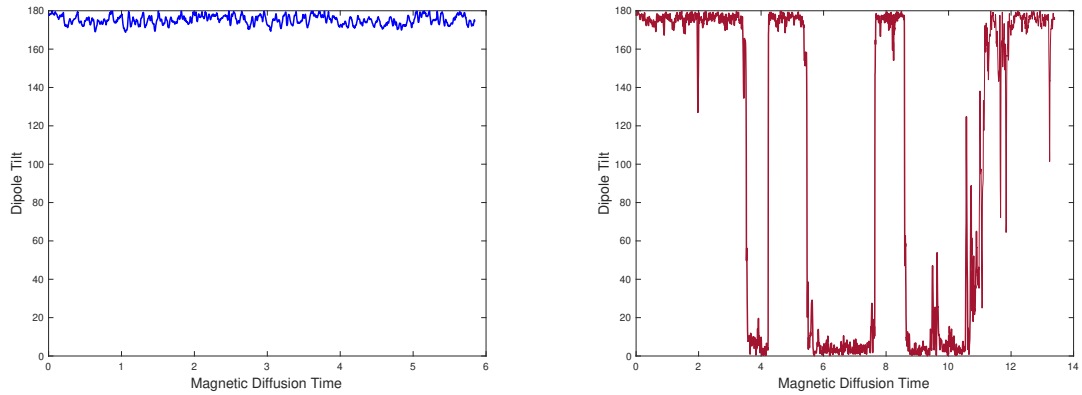

(a) model 6 **(b)** model 11

Figure 4-9. The dipole tilt of model 6 (bottom-heated) and model 11 (internally-heated).

space, shown in Figure 4-10(b & d). We can see that for the bottom heating case, the kinetic energy is concentrated in larger scale modes (i.e. SH l from 1 to 10) and near the inner core (r from 0.54 to 1.0). However, for the internal heating case, the energy is concentrated in smaller scales (i.e. SH l from 10 to 30) and throughout the core (r from 0.6 to 1.45). Such flows in the internally heated models could potentially twist and shear the existing magnetic field, and destroy the initial magnetic polarity.

4.4 Discussion and Future Work

1. Driving mechanism for the ancient Martian Dynamo

In the preliminary results of the ancient martian dynamo study, we found that a hemispheric dynamo that is stable in time is feasible, with preferentially more heat flux in the southern hemisphere imposed at the core mantle boundary. However, the ratio of the north-south magnetic dichotomy is not as high as what is seen in the martian crustal field (Amit et al., 2011). Second, the dynamo models in this study have assumed the existence of an inner core with bottom heating, where a considerable portion of the buoyancy source comes from light element expulsion or the released latent heat due to inner core crystallization. Recent discoveries from

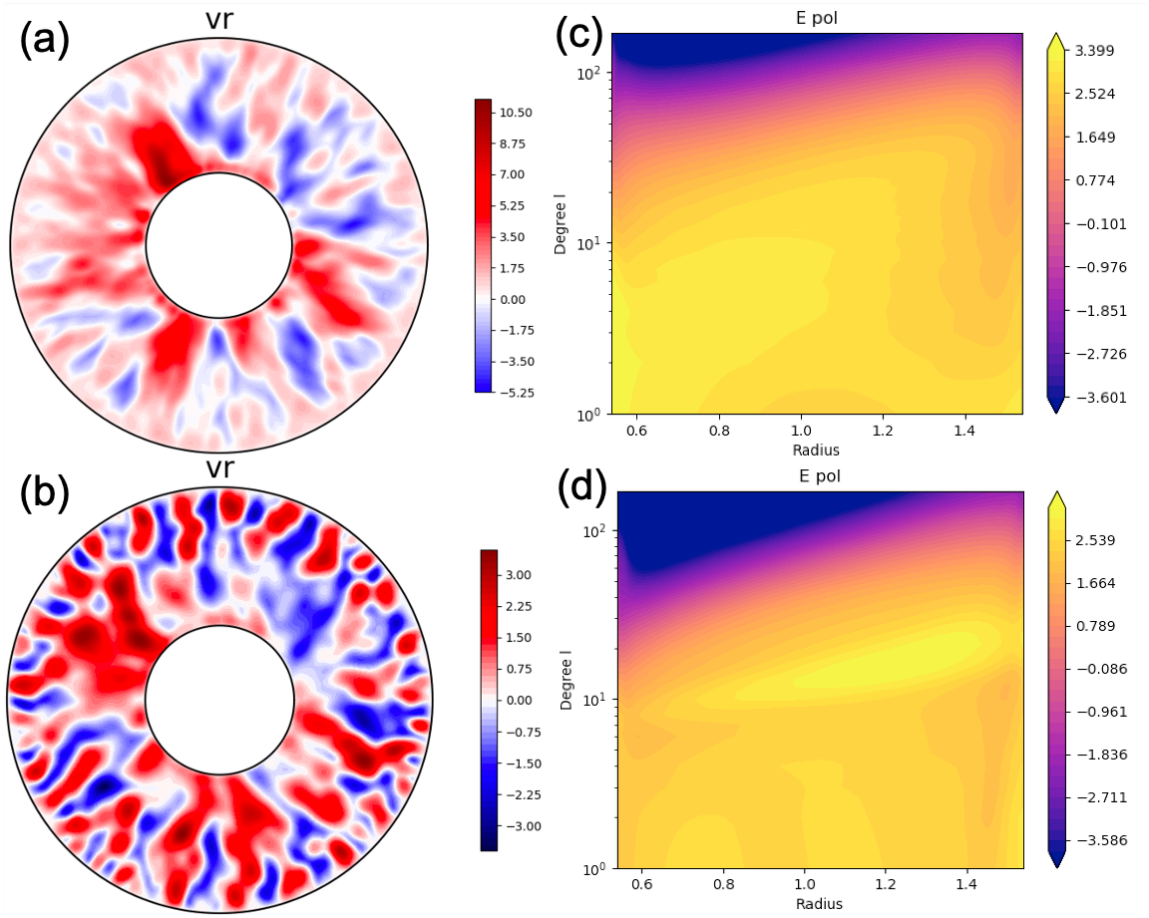

Figure 4-10. Radial velocities in the equatorial plane and poloidal kinetic energy spectrum for a stable hemispheric bottom-heated dynamo model 6 (a,c), and a reversing internally heated dynamo model 11 (b,d).

the InSight mission show an excessive amount of light elements such as sulphur in Mars' core materials, indicating the potential absence of a martian solid inner core. In this way, the compositional buoyancy released by inner core crystallization is lost, reducing the energy budget of Mars' ancient dynamo. Alternatively, instead of bottom up crystallization, it's possible that the core can crystallize from the top down as "iron-snow" (Breuer et al., 2015). Under specific conditions, the iron snow may fall from the top and then remelt into the layer until the core cools below the remelting temperature of the iron snow.

2. Incorporation of "iron-snow" into dynamo modeling

Therefore, future work should incorporate "iron-snow" into the dynamo modeling and to investigate the compositionally driven dynamo where the driving buoyancy force is from the top of the dynamo region. In this case, the buoyancy boundary condition at the dynamo top should be fixed buoyancy flux into the core while the boundary condition at the bottom should possibly be fixed buoyancy.

3. Continue work of the heating schemes

Even though we found that bottom heated dynamos tend to produce stable, hemispheric magnetic field, and internally heated dynamos tend to produce reversing ones, there are still some caveats that one should further investigate.

First of all, the same non-dimensional parameters may not necessarily mean the same buoyancy driving forces, as models with different heating schemes may have different critical Rayleigh numbers. In future work, models with different heating schemes need to be compared at the same level of supercriticality.

Second, the parameters that have been tested should be expanded to include a broader range of Rayleigh numbers and heat flux anomalies.

Model	Ra	E	P_r	P_m	BCs	Y_1^0 magnitude	Heating
1	$6.56e6$	$9.467e^{-5}$	1	1	SF/FF	0	b
2	$6.56e6$	$9.467e^{-5}$	1	1	SF/FF	0.5	b
3	$6.56e6$	$9.467e^{-5}$	1	1	SF/FF	0.8	b
4	$6.56e6$	$9.467e^{-5}$	1	1	SF/FF	1.0	b
5	$8.75e6$	$9.467e^{-5}$	1	1	SF/FF	0	b
6	$8.75e6$	$9.467e^{-5}$	1	1	SF/FF	0.5	b
7	$8.75e6$	$9.467e^{-5}$	1	1	SF/FF	1.0	b
8	$8.75e6$	$9.467e^{-5}$	1	1	SF/FF	1.5	b
9	$8.75e6$	$9.467e^{-5}$	1	1	SF/FF	2.0	b
10	$8.75e6$	$9.467e^{-5}$	1	1	SF/FF	0	i
11	$8.75e6$	$9.467e^{-5}$	1	1	SF/FF	0.5	i
12	$8.75e6$	$9.467e^{-5}$	1	1	SF/FF	1.0	i
13	$8.75e6$	$9.467e^{-5}$	1	1	SF/FF	1.5	i
14	$1.09e7$	$9.467e^{-5}$	1	1	SF/FF	0	b
15	$1.09e7$	$9.467e^{-5}$	1	1	SF/FF	0.5	b
16	$1.09e7$	$9.467e^{-5}$	1	1	SF/FF	1.0	b
17	$1.09e7$	$9.467e^{-5}$	1	1	SF/FF	1.5	b
18	$1.09e7$	$9.467e^{-5}$	1	1	SF/FF	2.0	b
19	$1.09e7$	$9.467e^{-5}$	1	1	SF/FF	0	i
20	$1.09e7$	$9.467e^{-5}$	1	1	SF/FF	0.5	i
21	$1.09e7$	$9.467e^{-5}$	1	1	SF/FF	1.0	i
22	$1.4e7$	$9.467e^{-5}$	1	1	SF/FF	0	b
23	$1.4e7$	$9.467e^{-5}$	1	1	SF/FF	0.5	b
24	$1.4e7$	$9.467e^{-5}$	1	1	SF/FF	1.0	b
25	$1.4e7$	$9.467e^{-5}$	1	1	SF/FF	1.5	b
26	$1.4e7$	$9.467e^{-5}$	1	1	SF/FF	0	i
27	$1.4e7$	$9.467e^{-5}$	1	1	SF/FF	0.5	i
28	$1.4e7$	$9.467e^{-5}$	1	1	SF/FF	1.0	i

Table 4-I. Performed simulations. BCs - boundary conditions, stress-free (SF) velocity boundaries and fixed flux (FF) thermal boundaries. Heating-heating scheme, b means bottom heating and i means internal heating).

Chapter 5

Discussion and Future Work

5.1 Conclusion

Using numerical dynamo modeling, I demonstrated in this thesis that the dynamo process is sensitive to the dynamo generation region geometry, and signatures of the dynamo region structure can be present in the observable magnetic field morphology at a planet's surface. This provide us with an independent method to learn about the planetary deep interiors, in a way no other methods can do.

For planet Earth, our study demonstrates that a stably stratified layer at the top of Earth's core may be necessary to explain the zonal octupolar component of the geomagnetic field over the past 10,000 years. We found that a fairly thin stable layer (60 km) needs to be relatively strongly stratified ($(N/2\Omega)^2 \in [0.95, 1.22]$) whereas a moderately thick layer (130 km) needs to be more weakly stratified ($(N/2\Omega)^2 \in [0.14, 0.27]$). Our model with a 350 km thick stable layer could not match the geomagnetic zonal octupolar constraint and the Earth-like χ^2 criterion.

For planet Saturn, our study demonstrates that a relatively thick stably stratified layer with moderate level of stratification and strong thermal winds inside the layer can explain features of Saturn's curious magnetic field.

These findings may answer some questions and fill one piece of the puzzle, but they certainly open up more questions that are worth investigation in the future.

5.2 Stably Stratified Layers

In the thesis, I used the stably stratified layer in numerical dynamo modeling which is implemented through a constant gradient of the background codensity. However, the stably stratified layer in reality may be more complex. For example, studies by Bouffard (2020) found that lighter elements tend to preferentially accumulate in the polar regions rather than the equatorial region, forming a stable layer that is thicker at the poles and thinner at the equator. The effect of the stable layer geometry on the resulting magnetic field has not been investigated. For example, would the magnetic field be filtered out more at the polar regions than the equator? Or would the morphology of the magnetic field be changed because of the latitudinal variance of the stable layer geometry? These effects may be worth future investigations.

Second, in the thesis, implementation of the stably stratified layer is conventionally based on the idea of "co-density", which unifies the thermal and compositional buoyancy sources by assuming the same diffusivity for both terms. However, these thermal and compositional diffusivities may differ by orders of magnitude in planetary cores. Furthermore, the thermal and compositional buoyancy forces may have the opposite (de)stabilizing effects, i.e. one may be convective while the other may be stable. This could give rise to more complex dynamics than stratification inside the layer (Figure 5-1). Implementing a stably stratified layer with two types of buoyancy sources allows complex dynamics such as double diffusive convection (DDC), where the fluid motion may be diffusive in a large scale but convective in smaller scales (Rosenblum et al., 2011). Previous work has demonstrated that the DDC has a significant impact on planetary interiors and their evolution history. Studies demonstrate that incorporating the DDC into planetary evolution could lead to redistribution of the heavy elements or severe core erosion in some cases (Leconte & Chabrier, 2012; Moll et al., 2017). Manglik et al. (2010) investigated finger convection in dynamos and found strengthened

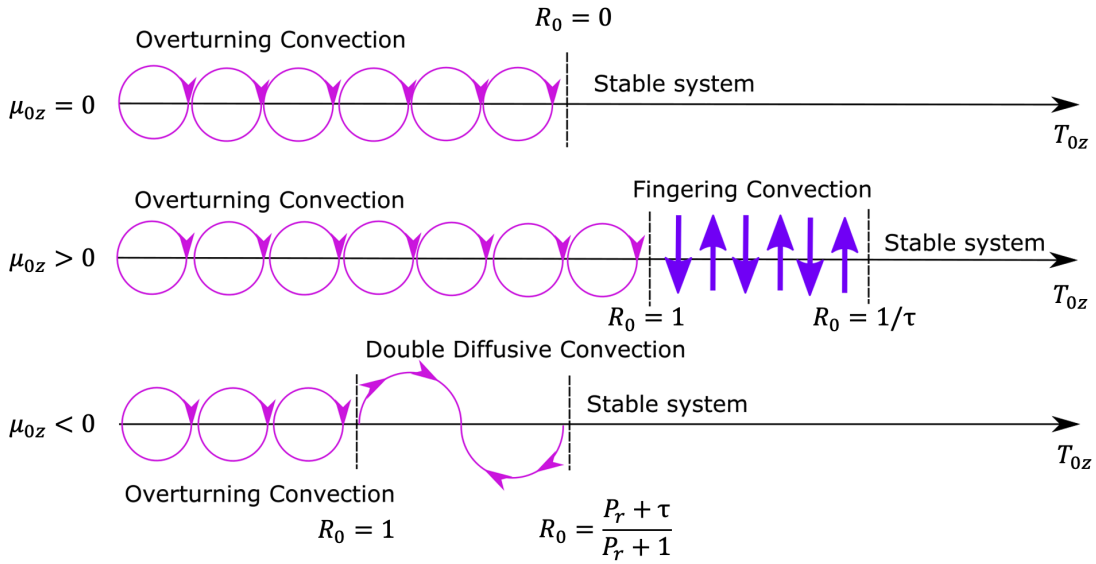

Figure 5-1. Illustration of various scenarios of convective instability. Figure adapted from Rosenblum et al. (2011).

magnetic field due to penetrative convection into the stable layer.

Future investigation involves implementing a stably stratified layer into dynamo modeling that include both buoyancy sources with antagonist gradients, in a rapidly rotating spherical shell. The stably layer will be implemented atop the core where the layer stability can be thermal or compositional in origin. The thickness of the stable layer can be fixed through the background buoyancy gradient. Incorporating the DDC into dynamo models may help determine if a compositionally stable but thermally unstable layer could generate more magnetic power in the high degrees to explain Saturn's flattened power spectrum.

5.3 Exoplanetary Magnetic Fields

The rapid growing number of extrasolar planets discovered over the past few decades has enriched the planetary categories (e.g. *"hot-Jupiters"*, *"mini-Neptunes"* and *"super-Earths"* ...), whereas Earth-like terrestrial analogs are harder to find due

to observational selection bias towards massive and short period planets. The recent discovery of a seven-terrestrial planetary system (TRAPPIST-1) was made using photometry during planets' transits. Several (TRAPPIST-1d & e) are possibly located in the "habitable zone" (Gillon et al., 2017), although the definition of habitability is still preliminary and a global magnetic field should be taken into account. In short conclusion, there is growing importance in detecting and characterizing magnetic fields of exoplanets.

There are a few ways to detect exoplanetary magnetic fields from Earth. The first method is through radio emissions from the interaction of stellar winds with planetary magnetic fields (Farrell, Desch, and Zarka, 1999), where the associated power of the cyclotron radiation is positively proportional to the magnetic flux density while inversely proportional to the distance from the planet to its parent star. Adopting this method, recent observations has reported active magnetic fields of a few hot Jupiters that may be 1.67 to 10 times stronger than Jupiter's magnetic field (Cauley et al., 2019).

The existence of a planetary magnetic field can also be inferred qualitatively through magnetospheric interactions between a planet and its parent star. As a planet orbits close enough to the primary star, it is possible that the magnetic field lines from two celestial bodies join together, thus trap the plasma in closed magnetic field lines between the planet and the parent star (Cohen et al., 2009). This is proposed to be the mechanism for some of the "hot spots" apparent on chromospheres of primary stars which are moving along with the planetary orbit.

A recent method for detecting planetary magnetic fields tries to look at the Helium absorption lines at 1083 nm (Oklopcic et al., 2019). They find that for magnetic fields stronger than a few $10^{-4}G$, metastable helium atoms in the escaping atmospheres could align with the planetary magnetic field, resulting in linearly polarized absorption at 1083 nm that traces the field direction. This method alleviates the strong magnetic

field condition of the cyclotron radiation method, although it cannot provide the magnetic field strength. In conclusion, exoplanetary exploration is a young field and constantly advancing. It opens up a broader test bed for planetary dynamo theory.

References

Acuna, M.H. et al. (1999). "Global Distribution of Crustal Magnetization Discovered by the Mars Global Surveyor MAG/ER Experiment." In: *Science* 284, pp. 790–793.

Acuña, M. H., N. F. Ness, and J. E. P. Connerney (1980). "The magnetic field of Saturn: Further studies of the Pioneer 11 observations." In: *Journal of Geophysical Research: Space Physics* 85.A11, pp. 5675–5678. DOI: https://doi.org/10.1029/JA085iA11p05675. eprint: https://agupubs.onlinelibrary.wiley.com/doi/pdf/10.1029/JA085iA11p05675.

Acuña, Mario H and Norman F Ness (1980). "The magnetic field of Saturn: Pioneer 11 observations." In: *Science* 207.4429, pp. 444–446.

Amit, Hagay, Ulrich R Christensen, and Benoit Langlais (2011). "The influence of degree-1 mantle heterogeneity on the past dynamo of Mars." In: *Physics of the Earth and Planetary Interiors* 189.1-2, pp. 63–79.

Anderson, Brian J et al. (2011). "The global magnetic field of Mercury from MESSENGER orbital observations." In: *Science* 333.6051, pp. 1859–1862.

Anderson, Brian J., Mario H. Acuña, et al. (2008). "The Structure of Mercury's Magnetic Field from MESSENGER's First Flyby." In: *Science* 321 (5585), p. 82.

Anderson, Brian J., Catherine L. Johnson, Haje Korth, Michael E. Purucker, et al. (2011). "The Global Magnetic Field of Mercury from MESSENGER Orbital Observations." In: *Science* 333 (6051), pp. 1859–1862.

Anderson, Brian J., Catherine L. Johnson, Haje Korth, Reka M. Winslow, et al. (2012). "Low-degree structure in Mercury's planetary magnetic field." In: *Journal of Geophysical Research: Planets* 117.E12. DOI: https://doi.org/10.1029/2012JE004159. eprint: https://agupubs.onlinelibrary.wiley.com/doi/pdf/10.1029/2012JE004159.

Aubert, Julien and Christopher C Finlay (2019). "Geomagnetic jerks and rapid hydromagnetic waves focusing at Earth's core surface." In: *Nature Geoscience* 12.5, pp. 393–398.

Aurnou, JM et al. (2015). "Rotating convective turbulence in Earth and planetary cores." In: *Physics of the Earth and Planetary Interiors* 246, pp. 52–71.

Bloxham, Jeremy (2000). "Sensitivity of the geomagnetic axial dipole to thermal core–mantle interactions." In: *Nature* 405.6782, pp. 63–65. DOI: 10.1038/35011045.

Bouffard, Mathieu, M Landeau, and A Goument (2020). "Convective erosion of a primordial stratification atop Earth's core." In: *Geophysical Research Letters* 47.14, e2020GL087109.

Braginsky, S. I. (1993). "MAC-Oscillations of the Hidden Ocean of the Core." In: *Journal of geomagnetism and geoelectricity* 45.11-12, pp. 1517–1538. DOI: 10.5636/jgg.45.1517.

Braginsky, Stanislav I. (1999). "Dynamics of the stably stratified ocean at the top of the core." In: *Physics of the Earth and Planetary Interiors* 111.1, pp. 21–34. DOI: https://doi.org/10.1016/S0031-9201(98)00143-5.

Breuer, Doris, Stephane Labrosse, and Tilman Spohn (2010). "Thermal evolution and magnetic field generation in terrestrial planets and satellites." In: *Space Science Reviews* 152.1-4, pp. 449–500.

Breuer, Doris, Tina Rueckriemen, and Tilman Spohn (2015). "Iron snow, crystal floats, and inner-core growth: modes of core solidification and implications for dynamos in terrestrial planets and moons." In: *Progress in Earth and Planetary Science* 2.1, pp. 1–26.

Bridge, HS et al. (1967). "Mariner V: Plasma and magnetic fields observed near Venus." In: *Science* 158.3809, pp. 1669–1673.

Buffett, Bruce (2014). "Geomagnetic fluctuations reveal stable stratification at the top of the Earth's core." In: *Nature* 507.7493, pp. 484–487. DOI: 10.1038/nature13122.

Buffett, Bruce A and Christopher T Seagle (2010). "Stratification of the top of the core due to chemical interactions with the mantle." In: *Journal of Geophysical Research: Solid Earth* 115.B4.

Bullard, E. C. and H. Gellman (1954). "Homogeneous dynamos and terrestrial magnetism." In: *Phil. Trans. Roy. Soc. Lond. A* 247, pp. 213–278.

Bullard, Edward Crisp and H. Gellman (1954). "Homogeneous dynamos and terrestrial magnetism." In: *Philosophical Transactions of the Royal Society of London. Series A, Mathematical and Physical Sciences* 247.928, pp. 213–278. DOI: 10.1098/rsta.1954.0018. eprint: https://royalsocietypublishing.org/doi/pdf/10.1098/rsta.1954.0018.

Cao, Hao, Michele K. Dougherty, et al. (2020). "The landscape of Saturn's internal magnetic field from the Cassini Grand Finale." In: *Icarus* 344, p. 113541. DOI: https://doi.org/10.1016/j.icarus.2019.113541.

Cao, Hao, Christopher T. Russell, Ulrich R. Christensen, et al. (2011). "Saturn's very axisymmetric magnetic field: No detectable secular variation or tilt." In: *Earth and Planetary Science Letters* 304.1, pp. 22–28. DOI: https://doi.org/10.1016/j.epsl.2011.02.035.

Cao, Hao, Christopher T. Russell, Johannes Wicht, et al. (2012). "Saturn's high degree magnetic moments: Evidence for a unique planetary dynamo." In: *Icarus* 221.1, pp. 388–394. DOI: https://doi.org/10.1016/j.icarus.2012.08.007.

Cao, Hao and David J. Stevenson (2017). "Zonal flow magnetic field interaction in the semi-conducting region of giant planets." In: *Icarus* 296, pp. 59–72. DOI: https://doi.org/10.1016/j.icarus.2017.05.015.

Cardin, Philippe and LG Cugliandolo (2011). *Dynamos: Lecture Notes of the Les Houches Summer School 2007*. Elsevier.

Cauley, P. Wilson et al. (2019). "Magnetic field strengths of hot Jupiters from signals of star–planet interactions." English (US). In: *Nature Astronomy* 3.12, pp. 1128–1134. DOI: 10.1038/s41550-019-0840-x.

Christensen, U R (2010). "Dynamo Scaling Laws and Applications to the Planets." In: *Space Science Reviews* 152.1-4, pp. 565–590.

Christensen, U.R. et al. (2001). "A numerical dynamo benchmark." In: *Physics of the Earth and Planetary Interiors* 128.1, pp. 25–34. DOI: https://doi.org/10.1016/S0031-9201(01)00275-8.

Christensen, Ulrich R and Johannes Wicht (2008a). "Models of magnetic field generation in partly stable planetary cores: Applications to Mercury and Saturn." In: *Icarus* 196.1, pp. 16–34.

Christensen, Ulrich R. (2006). "A deep dynamo generating Mercury's magnetic field." In: *Nature* 444.7122, pp. 1056–1058.

Christensen, Ulrich R., Julien Aubert, and Gauthier Hulot (2010). "Conditions for Earth-like geodynamo models." In: *Earth and Planetary Science Letters* 296.3, pp. 487–496. DOI: https://doi.org/10.1016/j.epsl.2010.06.009.

Christensen, Ulrich R. and Johannes Wicht (2008b). "Models of magnetic field generation in partly stable planetary cores: Applications to Mercury and Saturn." In: *Icarus* 196.1, pp. 16–34. DOI: https://doi.org/10.1016/j.icarus.2008.02.013.

Christensen, UR and Julien Aubert (2006). "Scaling properties of convection-driven dynamos in rotating spherical shells and application to planetary magnetic fields." In: *Geophysical Journal International* 166.1, pp. 97–114.

Cohen, O. et al. (2009). "Interactions of the Magnetospheres of Stars and Close-In Giant Planets." In: *apjl* 704.2, pp. L85–L88. DOI: 10.1088/0004-637X/704/2/L85. arXiv: 0909.3093 [astro-ph.SR].

Connerney, JEP, Mario H Acuna, and Norman F Ness (1991). "The magnetic field of Neptune." In: *Journal of Geophysical Research: Space Physics* 96.S01, pp. 19023–19042.

Connerney, JEP, Mario H Acuña, and Norman F Ness (1987). "The magnetic field of Uranus." In: *Journal of Geophysical Research: Space Physics* 92.A13, pp. 15329–15336.

Connerney, JEP, MH Acuña, et al. (2005). "Tectonic implications of Mars crustal magnetism." In: *Proceedings of the National Academy of Sciences* 102.42, pp. 14970–14975.

Connerney, JEP, S Kotsiaros, et al. (2018a). "A new model of Jupiter's magnetic field from Juno's first nine orbits." In: *Geophysical Research Letters* 45.6, pp. 2590–2596.

— (2018b). "A new model of Jupiter's magnetic field from Juno's first nine orbits." In: *Geophysical Research Letters* 45.6, pp. 2590–2596.

Connerney, JEP, NF Ness, and MH Acuna (1982). "Zonal harmonic model of Saturn's magnetic field from Voyager 1 and 2 observations." In: *Nature* 298.5869, pp. 44–46.

Constable, Catherine, Monika Korte, and Sanja Panovska (2016). "Persistent high paleosecular variation activity in southern hemisphere for at least 10,000 years." In: *Earth and Planetary Science Letters* 453, pp. 78–86. DOI: https://doi.org/10.1016/j.epsl.2016.08.015.

Cournède, C, J Gattacceca, and P Rochette (2012). "Magnetic study of large Apollo samples: Possible evidence for an ancient centered dipolar field on the Moon." In: *Earth and Planetary Science Letters* 331, pp. 31–42.

Cowling, T. G. (1934). "The magnetic field of sunspots." In: *Mon. Not. Roy. Astr. Soc.* 94, pp. 39–48.

Cox A, Doell RR and Dalrymple GB (1963). "Geomagnetic polarity epochs and Pleistocene geochronometry." In: *Nature* 198, pp. 1049–1051.

Cushman-Roisin, Benoit and Jean-Marie Beckers (2011). "Chapter 11 - Stratification." In: *Introduction to Geophysical Fluid Dynamics*. Ed. by Benoit Cushman-Roisin and Jean-Marie Beckers. Vol. 101. International Geophysics. Academic Press, pp. 347–364. DOI: https://doi.org/10.1016/B978-0-12-088759-0.00011-0.

Davies, Christopher J. and Catherine G. Constable (2014). "Insights from geodynamo simulations into long-term geomagnetic field behaviour." In: *Earth and Planetary Science Letters* 404, pp. 238–249. DOI: https://doi.org/10.1016/j.epsl.2014.07.042.

Davies, Christopher J., David Gubbins, et al. (2008). "Time-averaged paleomagnetic field and secular variation: Predictions from dynamo solutions based on lower mantle seismic

tomography." In: *Physics of the Earth and Planetary Interiors* 169.1, pp. 194–203. DOI: https://doi.org/10.1016/j.pepi.2008.07.021.

Debras, F. and G. Chabrier (2019). "New models of Jupiter in the context of Juno and Galileo." In: *arXiv: Earth and Planetary Astrophysics*.

Dietrich, W. and C.A. Jones (2018). "Anelastic spherical dynamos with radially variable electrical conductivity." In: *Icarus* 305, pp. 15–32. DOI: https://doi.org/10.1016/j.icarus.2018.01.003.

Dietrich, W. and J. Wicht (2013). "A hemispherical dynamo model: Implications for the Martian crustal magnetization." In: *Physics of the Earth and Planetary Interiors* 217, pp. 10–21. DOI: https://doi.org/10.1016/j.pepi.2013.01.001.

Dormy, Emmanuel and Andrew M Soward (2007). *Mathematical aspects of natural dynamos*. CRC Press.

Dougherty, Michele K. et al. (2018). "Saturn's magnetic field revealed by the Cassini Grand Finale." In: *Science* 362.6410, aat5434, aat5434. DOI: 10.1126/science.aat5434.

Dumberry, Mathieu and Christopher C Finlay (2007). "Eastward and westward drift of the Earth's magnetic field for the last three millennia." In: *Earth and Planetary Science Letters* 254.1-2, pp. 146–157.

Dwyer, CA, DJ Stevenson, and F Nimmo (2011). "A long-lived lunar dynamo driven by continuous mechanical stirring." In: *Nature* 479.7372, pp. 212–214.

Elkins-TANTON, Linda T, EM Parmentier, and PC Hess (2003). "Magma ocean fractional crystallization and cumulate overturn in terrestrial planets: Implications for Mars." In: *Meteoritics & Planetary Science* 38.12, pp. 1753–1771.

Elkins-Tanton, Linda T et al. (2005). "Early magnetic field and magmatic activity on Mars from magma ocean cumulate overturn." In: *Earth and Planetary Science Letters* 236.1-2, pp. 1–12.

Evans, AJ et al. (2014). "A wet, heterogeneous lunar interior: Lower mantle and core dynamo evolution." In: *Journal of Geophysical Research: Planets* 119.5, pp. 1061–1077.

Farrell, WM, MD Desch, and P Zarka (1999). "On the possibility of coherent cyclotron emission from extrasolar planets." In: *Journal of Geophysical Research: Planets (1991–2012)* 104.E6, pp. 14025–14032.

FJ, Vine and Matthews DH (1963). "Magnetic anomalies over oceanic ridges." In: *Nature* 199, pp. 947–949.

Frey, Herbert and Richard A Schultz (1988). "Large impact basins and the mega-impact origin for the crustal dichotomy on Mars." In: *Geophysical Research Letters* 15.3, pp. 229–232.

Fu, Roger R et al. (2012). "An ancient core dynamo in asteroid Vesta." In: *Science* 338.6104, pp. 238–241.

Fuller, Jim (2014). "Saturn ring seismology: Evidence for stable stratification in the deep interior of Saturn." In: *Icarus* 242, pp. 283–296. DOI: https://doi.org/10.1016/j.icarus.2014.08.006.

Galanti, E and Y Kaspi (2020). "Combined magnetic and gravity measurements probe the deep zonal flows of the gas giants." In: *Monthly Notices of the Royal Astronomical Society* 501.2, pp. 2352–2362. DOI: 10.1093/mnras/staa3722. eprint: https://academic.oup.com/mnras/article-pdf/501/2/2352/35392645/staa3722.pdf.

Garnero, Edward J and Donald V Helmberger (1995). "On seismic resolution of lateral heterogeneity in the Earth's outermost core." In: *Physics of the Earth and Planetary Interiors* 88.2, pp. 117–130.

Garrick-Bethell, Ian, Benjamin P Weiss, David L Shuster, and Jennifer Buz (2009). "Early lunar magnetism." In: *Science* 323.5912, pp. 356–359.

Garrick-Bethell, Ian, Benjamin P Weiss, David L Shuster, Sonia M Tikoo, et al. (2017). "Further evidence for early lunar magnetism from troctolite 76535." In: *Journal of Geophysical Research: Planets* 122.1, pp. 76–93.

Gill, Adrian E (2016). *Atmosphere—ocean dynamics*. Elsevier.

Gillon, Michaël et al. (2017). "Seven temperate terrestrial planets around the nearby ultracool dwarf star TRAPPIST-1." In: *Nature* 542, pp. 456–460. DOI: https://doi.org/10.1038/nature21360.

Gubbins, D. and C. J Davies (2013). "The stratified layer at the core–mantle boundary caused by barodiffusion of oxygen, sulphur and silicon." In: *Physics of the Earth and Planetary Interiors* 215, pp. 21–28. DOI: https://doi.org/10.1016/j.pepi.2012.11.001.

Gubbins, D., D. V. Kent, et al. (2000). "Four centuries of geomagnetic secular variation from historical records." In: *Philosophical Transactions of the Royal Society of London. Series A: Mathematical, Physical and Engineering Sciences* 358.1768, pp. 957–990. DOI: 10.1098/rsta.2000.0569.

Gubbins, David (2007). "Geomagnetic constraints on stratification at the top of Earth's core." In: *Earth, Planets and Space* 59.7, pp. 661–664.

Gubbins, David et al. (2015). "On core convection and the geodynamo: Effects of high electrical and thermal conductivity." In: *Physics of the Earth and Planetary Interiors* 247, pp. 56–64. DOI: https://doi.org/10.1016/j.pepi.2015.04.002.

Gurnett, D. A. et al. (1996). "Evidence for a magnetosphere at Ganymede from plasma-wave observations by the Galileo spacecraft." In: *Nature* 384.6609, pp. 535–537.

Halekas, J. S. et al. (2001). "Mapping of crustal magnetic anomalies on the lunar near side by the Lunar Prospector electron reflectometer." In: *Journal of Geophysical Research: Planets* 106.E11, pp. 27841–27852. DOI: https://doi.org/10.1029/2000JE001380.

Helffrich, George and Satoshi Kaneshima (2013). "Causes and consequences of outer core stratification." In: *Physics of the Earth and Planetary Interiors* 223, pp. 2–7. DOI: https://doi.org/10.1016/j.pepi.2013.07.005.

Holme, Richard and Jeremy Bloxham (1996). "The magnetic fields of Uranus and Neptune: Methods and models." In: *Journal of Geophysical Research: Planets* 101.E1, pp. 2177–2200.

Hood, L. L. et al. (2001). "Initial mapping and interpretation of lunar crustal magnetic anomalies using Lunar Prospector magnetometer data." In: *Journal of Geophysical Research: Planets* 106.E11, pp. 27825–27839. DOI: https://doi.org/10.1029/2000JE001366.

I, McDougall and Tarling DH (1963). "Dating of polarity zones in the Hawaiian Islands." In: *Nature* 200, pp. 54–56.

Iess, L. et al. (2019). "Measurement and implications of Saturn's gravity field and ring mass." In: *Science* 364.6445, aat2965, aat2965. DOI: 10.1126/science.aat2965.

Jackson, A., A. R. T. Jonkers, and M. R. Walker (2000). "Four centuries of geomagnetic secular variation from historical records." In: *Phil. Trans. Roy. Soc. Lond. A* 358, pp. 957–990.

Jiang, Weiyuan and Weijia Kuang (2008). "An MPI-based MoSST core dynamics model." In: *Physics of the Earth and Planetary Interiors* 170.1, pp. 46–51. DOI: https://doi.org/10.1016/j.pepi.2008.07.020.

Jonathan, Aurnou et al. (2008). "Convective heat transfer and the pattern of thermal emission on the gas giants." In: *Geophysical Journal International* 173.3, pp. 793–801.

Jones, Chris A (2011). "Planetary magnetic fields and fluid dynamos." In: *Annual Review of Fluid Mechanics* 43, pp. 583–614.

Kaneshima, Satoshi (2018). "Array analyses of SmKS waves and the stratification of Earth's outermost core." In: *Physics of the Earth and Planetary Interiors* 276, pp. 234–246. DOI: https://doi.org/10.1016/j.pepi.2017.03.006.

Ke, Y and VS Solomatov (2006). "Early transient superplumes and the origin of the Martian crustal dichotomy." In: *Journal of Geophysical Research: Planets* 111.E10.

Kivelson, M. G. et al. (1996). "Discovery of Ganymede's magnetic field by the Galileo spacecraft." In: *Nature* 384.6609, pp. 537–541.

Kuang, W. (1999). "Force balances and convective state in the Earth's core." In: *Phys. Earth Planet. Inter.* 116, pp. 65–79.

Kuang, Weijia and Jeremy Bloxham (1999). "Numerical Modeling of Magnetohydrodynamic Convection in a Rapidly Rotating Spherical Shell: Weak and Strong Field Dynamo Action." In: *Journal of Computational Physics* 153.1, pp. 51–81. DOI: https://doi.org/10.1006/jcph.1999.6274.

Landeau, Maylis, Julien Aubert, and Peter Olson (2017). "The signature of inner-core nucleation on the geodynamo." In: *Earth and Planetary Science Letters* 465, pp. 193–204. DOI: https://doi.org/10.1016/j.epsl.2017.02.004.

Landeau, Maylis, Peter Olson, Renaud Deguen, and Benjamin H Hirsh (2016a). "Core merging and stratification following giant impact." In: *Nature Geoscience* 9.10, pp. 786–789.

— (2016b). "Core merging and stratification following giant impact." In: *Nature Geoscience* 9.10, pp. 786–789.

Langel, Robert A (1982). "The magnetic Earth as seen from MAGSAT, initial results." In: *Geophysical Research Letters* 9.4, pp. 239–242.

Langlais, Benoit, Mioara Mandea, and Pascale Ultré-Guérard (2003). "High-resolution magnetic field modeling: application to MAGSAT and Ørsted data." In: *Physics of the Earth and Planetary Interiors* 135.2-3, pp. 77–91.

Le Bars, Michael et al. (2011). "An impact-driven dynamo for the early Moon." In: *Nature* 479.7372, pp. 215–218.

Leconte, Jérémy and Gilles Chabrier (2012). "A new vision of giant planet interiors: Impact of double diffusive convection." In: *Astronomy & Astrophysics* 540, A20.

Lister, John R. and Bruce A. Buffett (1998). "Stratification of the outer core at the core-mantle boundary." In: *Physics of the Earth and Planetary Interiors* 105.1, pp. 5–19. DOI: https://doi.org/10.1016/S0031-9201(97)00082-4.

Liu, Junjun, Peter M. Goldreich, and David J. Stevenson (2008). "Constraints on deep-seated zonal winds inside Jupiter and Saturn." In: *Icarus* 196.2, pp. 653–664. DOI: https://doi.org/10.1016/j.icarus.2007.11.036.

Lognonné, Philippe et al. (2020). "Constraints on the shallow elastic and anelastic structure of Mars from InSight seismic data." In: *Nature Geoscience* 13.3, pp. 213–220.

Lowes, FJ (1974). "Spatial power spectrum of the main geomagnetic field, and extrapolation to the core." In: *Geophysical Journal International* 36.3, pp. 717–730.

Luhmann, JG and Ch T Russell (1997). "Venus: Magnetic field and magnetosphere." In: *Encyclopedia of planetary sciences*, pp. 905–907.

Malkus, Willem VR (1973). "Convection at the melting point: a thermal history of the Earth's core." In: *Geophysical Fluid Dynamics* 4.3, pp. 267–278.

Mandea, Mioara et al. (2010). "Geomagnetic jerks: rapid core field variations and core dynamics." In: *Space science reviews* 155.1-4, pp. 147–175.

Manglik, Ajay, Johannes Wicht, and Ulrich R Christensen (2010). "A dynamo model with double diffusive convection for Mercury's core." In: *Earth and Planetary Science Letters* 289.3-4, pp. 619–628.

Mankovich, Christopher R. (2020). "Saturn's Rings as a Seismograph to Probe Saturn's Internal Structure." In: *AGU Advances* 1.2, e00142, e00142. DOI: 10.1029/2019AV000142.

Militzer, B., S. Wahl, and W. B. Hubbard (2019). "Models of Saturn's Interior Constructed with an Accelerated Concentric Maclaurin Spheroid Method." In: *The Astrophysical Journal* 879.2, 78, p. 78. DOI: 10.3847/1538-4357/ab23f0. arXiv: 1905.08907 [astro-ph.EP].

Militzer, Burkhard et al. (2016). "Understanding Jupiter's interior." In: *Journal of Geophysical Research: Planets* 121.9, pp. 1552–1572.

Mittelholz, A., C. L. Johnson, and A. Morschhauser (2018). "A New Magnetic Field Activity Proxy for Mars From MAVEN Data." In: *Geophysical Research Letters* 45.12, pp. 5899–5907. DOI: https://doi.org/10.1029/2018GL078425. eprint: https://agupubs.onlinelibrary.wiley.com/doi/pdf/10.1029/2018GL078425.

Mohit, Pundit Surdas and Jafar Arkani-Hamed (2004). "Impact demagnetization of the Martian crust." In: *Icarus* 168.2, pp. 305–317.

Moll, R et al. (2017). "Double-diffusive erosion of the core of Jupiter." In: *The Astrophysical Journal* 849.1, p. 24.

Moore, Kimberly M et al. (2018). "A complex dynamo inferred from the hemispheric dichotomy of Jupiter's magnetic field." In: *Nature* 561.7721, pp. 76–78.

Moore, Kimberly M. et al. (2017). "The analysis of initial Juno magnetometer data using a sparse magnetic field representation." In: *Geophysical Research Letters* 44.10, pp. 4687–4693. DOI: 10.1002/2017GL073133.

Moore, KM et al. (2019). "Time variation of Jupiter's internal magnetic field consistent with zonal wind advection." In: *Nature Astronomy* 3.8, pp. 730–735.

Morales, Miguel A et al. (2013). "Hydrogen-helium demixing from first principles: From diamond anvil cells to planetary interiors." In: *Physical Review B* 87.17, p. 174105.

Movshovitz, Naor et al. (2020). "Saturn's Probable Interior: An Exploration of Saturn's Potential Interior Density Structures." In: *The Astrophysical Journal* 891.2, p. 109. DOI: 10.3847/1538-4357/ab71ff.

Ness, N. et al. (1982). "Magnetic-field studies by Voyager 2—Preliminary results at Saturn." In: *Science* 215, pp. 558–563.

NESS, N. F. et al. (1975). "Magnetic field of Mercury confirmed." In: *Nature* 255 (5505), pp. 204–205.

Ness, N.F. (1979). "The magnetic field of Mercury." In: *Physics of the Earth and Planetary Interiors* 20.2, pp. 209–217. DOI: https://doi.org/10.1016/0031-9201(79)90044-X.

Ness, N.F. et al. (1976). "Observations of Mercury's magnetic field." In: *Icarus* 28 (4), pp. 479–488.

Ness, NF et al. (1974). "Magnetic field observations near Venus: Preliminary results from Mariner 10." In: *Science* 183.4131, pp. 1301–1306.

Ness, Norman F, Mario H Acuna, Leonard F Burlaga, et al. (1989). "Magnetic fields at Neptune." In: *Science* 246.4936, pp. 1473–1478.

Ness, Norman F, Mario H Acuna, Ronald P Lepping, et al. (1979a). "Magnetic field studies at Jupiter by Voyager 1: Preliminary results." In: *Science* 204.4396, pp. 982–987.

Ness, Norman F, Mario H Acuna, Ronald P Lepping, et al. (1979b). "Magnetic field studies at Jupiter by Voyager 2: Preliminary results." In: *Science* 206.4421, pp. 966–972.

Ness, Norman F, Mario H Acuña, et al. (1981). "Magnetic field studies by Voyager 1: Preliminary results at Saturn." In: *Science* 212.4491, pp. 211–217.

Nettelmann, Nadine, Robert Püstow, and Ronald Redmer (2013). "Saturn layered structure and homogeneous evolution models with different EOSs." In: *Icarus* 225.1, pp. 548–557. DOI: 10.1016/j.icarus.2013.04.018. arXiv: 1304.4707 [astro-ph.EP].

Nimmo, F et al. (2008). "Implications of an impact origin for the martian hemispheric dichotomy." In: *Nature* 453.7199, pp. 1220–1223.

Nimmo, Francis (2000). "Dike intrusion as a possible cause of linear Martian magnetic anomalies." In: *Geology* 28.5, pp. 391–394. DOI: 10.1130/0091-7613(2000)28<391:DIAAPC>2.0.CO;2. eprint: https://pubs.geoscienceworld.org/geology/article-pdf/28/5/391/3518840/i0091-7613-28-5-391.pdf.

— (2002). "Why does Venus lack a magnetic field?" In: *Geology* 30.11, pp. 987–990.

Nimmo, Francis and Martha S Gilmore (2001). "Constraints on the depth of magnetized crust on Mars from impact craters." In: *Journal of Geophysical Research: Planets* 106.E6, pp. 12315–12323.

O'Rourke, JG et al. (2019). "Detectability of remanent magnetism in the crust of Venus." In: *Geophysical Research Letters* 46.11, pp. 5768–5777.

O'Rourke, Joseph G, Cédric Gillmann, and Paul Tackley (2018). "Prospects for an ancient dynamo and modern crustal remanent magnetism on Venus." In: *Earth and Planetary Science Letters* 502, pp. 46–56.

Oklopcic, Antonija et al. (2019). "Detecting Magnetic Fields in Exoplanets with Spectropolarimetry in the Helium Line at 1083 nm." In: *AAS/Division for Extreme Solar Systems Abstracts*. Vol. 51. AAS/Division for Extreme Solar Systems Abstracts, p. 103.05.

Olsen, Nils, R Holme, et al. (2000). "Ørsted initial field model." In: *Geophysical Research Letters* 27.22, pp. 3607–3610.

Olsen, Nils, Hermann Lühr, et al. (2014). "The CHAOS-4 geomagnetic field model." In: *Geophysical Journal International* 197.2, pp. 815–827.

Olson, Peter and Ulrich R Christensen (2006). "Dipole moment scaling for convection-driven planetary dynamos." In: *Earth and Planetary Science Letters* 250.3-4, pp. 561–571.

Olson, Peter, Maylis Landeau, and Evan Reynolds (2017). "Dynamo tests for stratification below the core-mantle boundary." In: *Physics of the Earth and Planetary Interiors* 271, pp. 1–18. DOI: https://doi.org/10.1016/j.pepi.2017.07.003.

Purucker, Michael E and Joseph B Nicholas (2010). "Global spherical harmonic models of the internal magnetic field of the Moon based on sequential and coestimation approaches." In: *Journal of Geophysical Research: Planets (1991–2012)* 115.E12, E12007.

Ridley, Victoria A and Richard Holme (2016). "Modeling the Jovian magnetic field and its secular variation using all available magnetic field observations." In: *Journal of Geophysical Research: Planets* 121.3, pp. 309–337.

Roberts, James H and Shijie Zhong (2006). "Degree-1 convection in the Martian mantle and the origin of the hemispheric dichotomy." In: *Journal of Geophysical Research: Planets* 111.E6.

Rosenblum, Erica et al. (2011). "Turbulent mixing and layer formation in double-diffusive convection: Three-dimensional numerical simulations and theory." In: *The Astrophysical Journal* 731.1, p. 66.

Sabaka, Terence J, Nils Olsen, and Michael E Purucker (2004). "Extending comprehensive models of the Earth's magnetic field with Ørsted and CHAMP data." In: *Geophysical Journal International* 159.2, pp. 521–547.

Schaeffer, Nathanaël (2013). "Efficient spherical harmonic transforms aimed at pseudospectral numerical simulations." In: *Geochemistry, Geophysics, Geosystems* 14.3, pp. 751–758.

Schwaiger, T, T Gastine, and J Aubert (2019). "Force balance in numerical geodynamo simulations: a systematic study." In: *Geophysical Journal International* 219, S101–S114. DOI: 10.1093/gji/ggz192.

Smith, EJ, L Davis, et al. (1975). "Jupiter's magnetic field. Magnetosphere, and interaction with the solar wind: Pioneer 11." In: *Science* 188.4187, pp. 451–455.

Smith, EJ, L Davis Jr, et al. (1974). "The planetary magnetic field and magnetosphere of Jupiter: Pioneer 10." In: *Journal of Geophysical Research* 79.25, pp. 3501–3513.

Soderlund, Krista M. (n.d.). "Ocean Dynamics of Outer Solar System Satellites." In: *Geophysical Research Letters* 46.15 (), pp. 8700–8710. DOI: https://doi.org/10.1029/2018GL081880. eprint: https://agupubs.onlinelibrary.wiley.com/doi/pdf/10.1029/2018GL081880.

Solomon, Sean C et al. (2005). "New perspectives on ancient Mars." In: *science* 307.5713, pp. 1214–1220.

Sreenivasan, Binod (2010). "Modelling the geodynamo: progress and challenges." In: *Current Science*, pp. 1739–1750.

Sreenivasan, Binod and David Gubbins (2008). "Dynamos with weakly convecting outer layers: implications for core-mantle boundary interaction." In: *Geophysical and Astrophysical Fluid Dynamics* 102.4, pp. 395–407.

Stanley, S. (2010). "A dynamo model for axisymmetrizing Saturn's magnetic field." In: *Geophys. Res. Lett.* 37. DOI: 10.1029/2009GL041752.

— (2014). "Magnetic Field Generation in Planets." In: *Encyclopedia of the Solar System, 3rd Edition*. Ed. by T. Spohn, D. Breuer, and T. Johnson. Elsevier.

Stanley, S. and J. Bloxham (2016). "On the secular variation of Saturn's magnetic field." In: *Physics of the Earth and Planetary Interiors* 250, pp. 31–34. DOI: https://doi.org/10.1016/j.pepi.2015.11.002.

Stanley, Sabine and Jeremy Bloxham (2004). "Convective-region geometry as the cause of Uranus' and Neptune's unusual magnetic fields." In: *Nature* 428.6979, pp. 151–153.

Stanley, Sabine and Aylia Mohammadi (2008). "Effects of an outer thin stably stratified layer on planetary dynamos." In: *Physics of the Earth and Planetary Interiors* 168.3, pp. 179–190. DOI: https://doi.org/10.1016/j.pepi.2008.06.016.

Stegman, Dave R et al. (2003). "An early lunar core dynamo driven by thermochemical mantle convection." In: *Nature* 421.6919, pp. 143–146.

Stevenson, DJ (1980). *Saturn's luminosity and magnetism*.

— (1982). "Reducing the non-axisymmetry of a planetary dynamo and an application to Saturn." In: *Geophysical & Astrophysical Fluid Dynamics* 21.1-2, pp. 113–127.

Tanaka, Satoru and Hiroyuki Hamaguchi (1993). "Velocities and Chemical Stratification in the Outermost Core." In: *Journal of geomagnetism and geoelectricity* 45.11-12, pp. 1287–1301. DOI: 10.5636/jgg.45.1287.

Tang, Vivian, Li Zhao, and Shu-Huei Hung (2015). "Seismological evidence for a non-monotonic velocity gradient in the topmost outer core." In: *Scientific Reports* 5.1, p. 8613.

Thébault, E. et al. (2018). "A time-averaged regional model of the Hermean magnetic field." In: *Physics of the Earth and Planetary Interiors* 276, pp. 93–105.

Thébault, Erwan et al. (2015). "International geomagnetic reference field: the 12th generation." In: *Earth, Planets and Space* 67.1, pp. 1–19.

Tsang, Yue-Kin and Chris A. Jones (2020). "Characterising Jupiter's dynamo radius using its magnetic energy spectrum." In: *Earth and Planetary Science Letters* 530, p. 115879. DOI: https://doi.org/10.1016/j.epsl.2019.115879.

Tsunakawa, Hideo et al. (2010). "Lunar magnetic field observation and initial global mapping of lunar magnetic anomalies by MAP-LMAG onboard SELENE (Kaguya)." In: *Space science reviews* 154.1-4, pp. 219–251.

Vestine, Ernest Harry and Anne B Kahle (1968). "The westward drift and geomagnetic secular change." In: *Geophysical Journal International* 15.1-2, pp. 29–37.

Vine, F. J. and D. H. Matthews (1963). "Magnetic Anomalies Over Oceanic Ridges." In: *Nature* 199.4897, pp. 947–949.

Voorhies, C. V., T. J. Sabaka, and M. Purucker (2002). "On magnetic spectra of Earth and Mars." In: *Journal of Geophysical Research: Planets* 107.E6, pp. 1-1-1–10. DOI: https://doi.org/10.1029/2001JE001534. eprint: https://agupubs.onlinelibrary.wiley.com/doi/pdf/10.1029/2001JE001534.

Vorberger, J. et al. (2007). "Hydrogen-helium mixtures in the interiors of giant planets." In: *Phys. Rev. B* 75 (2), p. 024206. DOI: 10.1103/PhysRevB.75.024206.

Weiss, Benjamin P, Jérôme Gattacceca, et al. (2010). "Paleomagnetic records of meteorites and early planetesimal differentiation." In: *Space Science Reviews* 152.1, pp. 341–390.

Weiss, Benjamin P and Sonia M Tikoo (2014). "The lunar dynamo." In: *Science* 346.6214.

Weiss, Benjamin P, Hojatollah Vali, et al. (2002). "Records of an ancient Martian magnetic field in ALH84001." In: *Earth and Planetary Science Letters* 201.3-4, pp. 449–463.

Wicht, J., T. Gastine, and L. D. V. Duarte (2019). "Dynamo Action in the Steeply Decaying Conductivity Region of Jupiter-Like Dynamo Models." In: *Journal of Geophysical Research (Planets)* 124.3, pp. 837–863. DOI: 10.1029/2018JE005759. arXiv: 1808.05356 [astro-ph.EP].

Wicht, J., T. Gastine, L. D. V. Duarte, and W. Dietrich (2019). "Dynamo action of the zonal winds in Jupiter." In: *Astronomy and Astrophysics* 629, A125, A125. DOI: 10.1051/0004-6361/201935682.

Wicht, Johannes (2002). "Inner-core conductivity in numerical dynamo simulations." In: *Physics of the Earth and Planetary Interiors* 132.4, pp. 281–302.

Wilhelms, Don E and Steven W Squyres (1984). "The Martian hemispheric dichotomy may be due to a giant impact." In: *Nature* 309.5964, pp. 138–140.

Yan, C. and S. Stanley (2018). "Sensitivity of the Geomagnetic Octupole to a Stably Stratified Layer in the Earth's Core." In: *Geophysical Research Letters* 45.20, pp. 11, 005–11, 011. DOI: https://doi.org/10.1029/2018GL078975.

Zhang, Nan and Shijie Zhong (2011). "Heat fluxes at the Earth's surface and core–mantle boundary since Pangea formation and their implications for the geomagnetic superchrons." In: *Earth and Planetary Science Letters* 306.3, pp. 205–216. DOI: https://doi.org/10.1016/j.epsl.2011.04.001.

Zhao, Xixi and Robert S. Coe (1987). "Palaeomagnetic constraints on the collision and rotation of North and South China." In: *Nature* 327.6118, pp. 141–144.

Zhong, Shijie and Maria T Zuber (2001). "Degree-1 mantle convection and the crustal dichotomy on Mars." In: *Earth and Planetary Science Letters* 189.1-2, pp. 75–84.

Zou, Zuihong, Keith D Koper, and Vernon F Cormier (2008). "The structure of the base of the outer core inferred from seismic waves diffracted around the inner core." In: *Journal of Geophysical Research: Solid Earth* 113.B5.

Appendix I

Bullard-Gellman Formalism

Case of the Stably Stratified Layer in Earth

In Chapter 2 we observed amplified power (Figure 2-4(a)) in the velocity modes $(l, m) = (3, 0)$ and $(l, m) = (5, 0)$ due to the presence of a stable layer where models with larger layer stabilities lead to stronger amplification of these zonal flows. Models with a stable layer demonstrates amplification of the g_3^0/g_1^0 ratio, as shown in Figure 2-4(b).

This amplified octupolar zonal flow (T_3^0) can lead to creation of the magnetic octupole field (P_3^0) through a two-step dynamo mechanism, shown in Figure I-1, described with the Bullard and Gellman (1954) formalism. The first step is to create a toroidal magnetic field (T_1^{1c}):

$$T_3^0 P_2^{1c} T_1^{1c} \tag{I.1}$$

which satisfy the selection rules of *Adams-Gaunt* integral. The second step is to use the existing toroidal magnetic field (T_1^{1c}) to create the zonal octupolar magnetic field (P_3^0):

$$P_3^{1c} T_1^{1c} P_3^0 \tag{I.2}$$

which satisfy the selection rules of *Elsasser* integral.

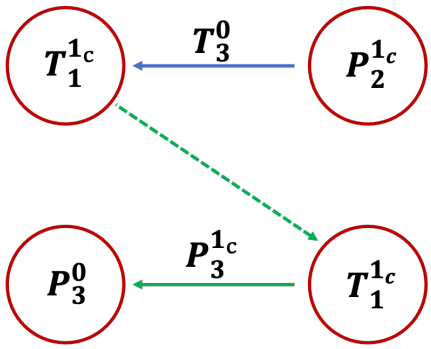

Figure I-1. Interaction diagram of the Bullard-Gellman formalism for the case of the Earth's stably stratified layer in Chapter 2. Red/Green circles represent the existing/created magnetic field, blue arrows represent various velocity fields.

Case of the Saturn's Dynamo

In Chapter 3 we try to understand how Y_2^0 heat flux perturbation could affect the magnetic quadrupole. From Figure 3-9 we observed amplified poloidal kinetic energy in degree 1 (Figure 3-9a) and amplified toroidal kinetic energy in degree one (Figure 3-9b). These can lead to creation of the magnetic quadrupole field (P_2^0) in the following ways.

First, the axisymmetric degree one poloidal (P_1^0) flow could act on the poloidal magnetic dipole (P_1^0) field and generate poloidal magnetic quadrupole (P_2^0) field, which satisfy the *Elsasser* integral (Figure I-2(a)).

Second, the amplified degree one zonal flow (T_1^0) can lead to creation of the magnetic octupole field (P_2^0) through a two-step dynamo mechanism, shown in Figure I-2(b). The first step is to create a toroidal magnetic field (T_2^{1c}):

$$T_1^0 P_1^{1c} T_2^{1c} \tag{I.3}$$

which satisfies the selection rules of the *Adams-Gaunt* integral. The second step is to use the existing toroidal magnetic field (T_2^{1c}) to create the zonal octupolar magnetic field (P_2^0):

$$P_1^{1s} T_2^{1c} P_2^0 \tag{I.4}$$

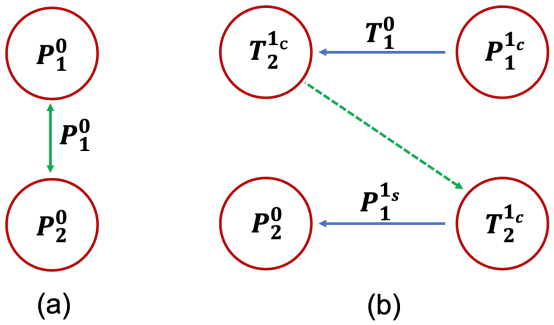

Figure I-2. Interaction diagram of the Bullard-Gellman formalism for the case of Saturn's dynamo in Chapter 3. Red circles represent the existing or created magnetic field, green/blue arrows represent *Elsasser*/*Adams-Gaunt* integrals.

which satisfies the selection rules of the *Elsasser* integral.